

Carnegie Mellon University
MELLON COLLEGE OF SCIENCE

THESIS

SUBMITTED IN PARTIAL FULFILLMENT OF THE REQUIREMENTS
FOR THE DEGREE OF

DOCTOR OF PHILOSOPHY IN THE FIELD OF PHYSICS

TITLE: "Layered two-dimensional heterostructures and their tunneling characteristics"

PRESENTED BY: Sergio de la Barrera

ACCEPTED BY THE DEPARTMENT OF PHYSICS

RANDALL FEENSTRA 8/25/16

RANDALL FEENSTRA, CHAIR PROFESSOR DATE

STEPHEN GAROFF 8/25/16

STEPHEN GAROFF, DEPT HEAD DATE

APPROVED BY THE COLLEGE COUNCIL

REBECCA DOERGE 8/25/16

REBECCA DOERGE, DEAN DATE

Layered two-dimensional heterostructures and their tunneling characteristics

by

Sergio C. de la Barrera

Submitted in partial fulfillment of the
requirements for the degree of
Doctor of Philosophy

at

Carnegie Mellon University
Department of Physics
Pittsburgh, Pennsylvania

Advised by Professor Randall M. Feenstra

July 29, 2016

Abstract

Two-dimensional materials and their heterostructures offer a new paradigm for studying physics, engineering, and materials on the nano-scale. In the course of this work I argue that layered heterostructures of two-dimensional crystals graphene, hexagonal boron nitride, and transition metal dichalcogenides provide new and interesting interlayer transport phenomena. Low-energy electron microscopy is employed to study the surface of atomically thin WSe_2 prepared by metal-organic chemical vapor deposition on epitaxial graphene substrates, and a method for unambiguously measuring the number of atomic layers is presented. Using very low-energy electrons to probe the surface of similar heterostructures, a relationship between extracted work function differences from the layers and the nature of the electrical contact between them is revealed. An extension of this analysis is applied to surface studies of MoSe_2 prepared by molecular beam epitaxy on epitaxial graphene. A large work function difference is measured between the MoSe_2 and graphene, and a model is provided which suggests that this observation results from an exceptional defect density in the MoSe_2 film. I describe a theory for computing tunneling currents between two-dimensional crystals separated by a thin insulating barrier, and a few situations resulting in resonant tunneling and negative differential resistance are illustrated by computed examples, as well as observed characteristics, for monolayer and bilayer graphene tunneling junctions and transistors.

Acknowledgements

First and foremost, I would like to thank my darling wife, who agreed to follow along with me on this journey toward a Ph.D., and remained by my side throughout. Never have I met a more lovely and dedicated person; diligent in her own undertakings, and yet compassionate and supportive in all her personal relationships. It is through her love, support, and exemplary work ethic over the years that I have been able to maintain course, and enjoy life while I do it. I am darn lucky to have met her, and I look forward to many more happy years together.

I remember being drawn to science at a very young age. I had a habit of broadcasting my latest findings to anyone who would listen, and perhaps just as often to those who would not. I appreciate that my mother did not find this behavior as annoying as surely many others would, in fact, she must have regarded it as rather cute given the level of support toward my interests that she unconditionally provided. In any case, I have her to thank for fostering my academic curiosities, taking me to the museums on my request with somewhat ridiculous frequency, supplying all the books, tools, and toys that I required to continue my research into bugs, dinosaurs, volcanoes, planets, chemistry, engineering, and of course eventually, physics. I cannot imagine myself being as happy with the person I have become if it had been any other way, so I thank her.

In my time at Carnegie Mellon University I have had the pleasure of knowing a large number of inspiring and intelligent people. Beginning with my close friends and colleagues from my cohort, I would like to thank David Menasche and Paul La Plante for all of our great conversations, late-night study sessions, and dependability over the years. From my own research group I extend special thanks to Nishtha Srivastava for training me to use the scanning tunneling microscope and for her mentorship, to Patrick Mende for his excellent training regarding the use of low-energy electron microscopy and the graphitization chamber, and finally Jun Li, for his tireless calculations and generally amicable demeanor. I would also like to thank Devashish Gopalan for his friendship and dedication toward building up our nanofabrication process, and along those lines, I thank Mohamed Darwish for his tireless training sessions with me in the nanofabrication facility, and characterization of our first graphene heterostructures.

I would like to thank my collaborators, especially Suresh Vishwanath, Yu-Chuan Lin, Sarah Eichfeld, and Zak Al Balushi for their hard work preparing various films for our studies, Qin Gao, Yifan Nie, and Mike Widom for running an enormous number of density functional theory calculations, Tania Roy and Eric Vogel for our coordinated effort to understand their measured tunneling characteristics, and finally Grace Xing and Josh Robinson for their leadership on several projects. I would like to thank Jean-Yves Desaulles for his dedication to producing high-quality exfoliated graphene, and Andrew Ye for his assistance in constructing and setting up the transfer facility, and recently in exfoliating and transferring for our heterostructures. On the topic

of the exfoliation and transfer facility, I would like to extend very special thanks to Ben Hunt, who has given me immeasurable guidance with regard to that project and many others along the way. I am sincerely looking forward to working together as we move ahead with various projects related to 2D materials.

In closing, I would like to thank all of my past advisors, Charles Melcher, Ray Klann, and Manfred Paulini, each of whom placed their confidence in me and deserve much of the credit for my being here today. I would like to thank my outstanding thesis committee members, Di Xiao, Bob Suter, and Jeff Weldon, each of whom have provided critical mentoring and feedback over the years. Finally, I would like to extend my deepest gratitude to my Ph.D. thesis advisor, Randy Feenstra. It has been an honor and a privilege to have worked with him over the years; my remaining hope is that I can live up to the ideals of his mentorship in the years to come. Randy is truly a great scientist and thinker, and I am humbled to have known him.

Contents

1	Introduction	1
1.1	Two-dimensional materials: a new paradigm for physics in reduced dimensions	2
1.1.1	Graphite in the few-layer limit	3
1.1.2	Hexagonal boron nitride: an ultraflat wide-band-gap insulator	7
1.1.3	Semiconductors in two dimensions: transition metal dichalcogenides	7
1.2	Resonant tunneling physics in its various forms	9
1.2.1	Esaki tunnel diode	10
1.2.2	Double-barrier resonant tunneling diode	11
1.2.3	Lateral momentum conservation in two dimensions	12
1.2.4	Many-body effects and excitonic condensates	14
2	Experimental methods	16
2.1	Low-energy electron microscopy and reflectivity	16
2.1.1	Bright-field and dark-field imaging	18
2.1.2	Electron diffraction in a LEEM	19
2.1.3	Spectroscopic analysis with low-energy electron reflectivity . .	20
2.2	Relative work-function extraction from reflectivity	24
3	Thickness characterization of tungsten diselenide using electron reflectivity oscillations	32
3.1	Introduction	32
3.2	Methods	33
3.3	Experimental results	34
3.4	Theoretical results	38
3.5	Discussion	46
3.6	Conclusions	47
4	Tunneling transport between transition metal dichalcogenides	48
4.1	Introduction	48
4.2	Vertical transport between tungsten diselenide and epitaxial graphene	50
4.2.1	Sample fabrication	51

4.3	LEEM analysis of tungsten diselenide–epitaxial graphene tunneling heterostructures	52
4.4	Charge transfer in tungsten diselenide–epitaxial graphene heterostructures	55
4.5	Impact of tungsten diselenide–epitaxial graphene characterization	61
5	Application of work function extraction method to material characterization	62
5.1	Defect density in molybdenum diselenide prepared by molecular beam epitaxy	62
6	Theoretical background	69
6.1	Interlayer tunneling between 2D materials and the Bardeen method	70
6.2	Tunneling between monolayers of graphene	75
6.2.1	Theoretical formalism	75
6.2.2	Simulation of tunneling characteristics	76
6.3	Electrostatics of layered 2D heterostructures	78
6.3.1	Potentials between two monolayers with top and bottom gates	79
6.3.2	The special case of bilayer graphene	80
7	Theory of graphene–insulator–graphene tunnel junctions	83
7.1	Introduction	83
7.2	Theoretical formalism	84
7.3	Hexagonal boron nitride tunneling barrier	90
7.4	Comparison to experiment	94
7.5	Summary	100
8	Tunneling between bilayers of graphene	102
8.1	Introduction	102
8.2	Tunneling mechanism	103
8.3	Theoretical formalism	107
8.4	Comparison to experiment	108
8.5	Conclusions	108
9	Progress toward 2D tunneling devices	110
9.1	A new facility for 2D crystal exfoliation and transfer	112
9.2	Initial studies of exfoliated materials and challenges	113
9.3	Layered heterostructures of 2D materials for device transport	114
10	Conclusions	116
Appendix A	2D–2D tunneling in the zero-coherence-length limit	118

Appendix B	Details of resonant tunneling model for graphene and its bilayers	121
B.1	Monolayer graphene	121
B.2	Bilayer graphene: parabolic dispersion	123
B.3	Bilayer graphene: hyperbolic dispersion	124
Appendix C	Resonant tunneling between transition metal dichalcogenides	126
C.1	Tight-binding model and dispersion	126
C.2	Energy-conservation between tunneling states in transition metal dichalcogenides	128
C.3	Density of states and occupation of levels	128

List of Figures

1.1	Atomic structure of graphene with top view and side views of armchair and zig-zag edges, and first Brillouin zone of the graphene lattice in reciprocal space	3
1.2	Band structure of graphene produced by the tight-binding method showing linear dispersion and Dirac cones	4
1.3	Atomic structure of monolayer hexagonal boron nitride viewed from the out-of-plane direction	6
1.4	Atomic structure of a transition metal dichalcogenide with side views emphasizing the coexistence of three separate atomic planes	8
1.5	Band diagram of an Esaki tunnel diode at resonance	10
1.6	Illustration of voltage-driven negative differential resistance	10
1.7	Band diagram of a double-barrier resonant tunneling diode at resonance	11
1.8	Coincidence of bands in momentum space leading to negative differential resistance	12
1.9	Schematic of a 2D–2D tunneling transistor based on conventional semiconductors	13
2.1	Diagram of a low-energy electron microscope	17
2.2	Bright-field, dark-field, and diffraction images of exfoliated WSe ₂ on epitaxial graphene from LEEM	18
2.3	Electrostatic potential model of a low-energy electron microscope	21
2.4	Electron reflectivity spectra from graphene on Cu showing onset voltage fitting for relative work function extraction	25
2.5	Energy diagrams of vacuum potential extending from a sample surface with emitted electron energy distribution in LEEM	26
2.6	Schematic diagram of deflected beam trajectories near a sample surface as observed in mirror-mode	29
2.7	Image distortion due to beam deflection by surface potential variations in mirror-mode, and signature of such deflection in very low-energy reflectivity	30

3.1	LEEM images and reflectivity of few-layer WSe ₂ crystals on epitaxial graphene on SiC showing the ability to discriminate between WSe ₂ crystals of varying thicknesses	35
3.2	Atomic force microscope image of monolayer (1 ML), bilayer (2 ML), and trilayer (3 ML) regions of WSe ₂ on epitaxial graphene	36
3.3	Spectroscopic map of WSe ₂ on epitaxial graphene using assignment of colors to indicate the number of layers based on reflectivity	37
3.4	LEEM image and diffraction patterns from WSe ₂ on epitaxial graphene and bare graphene, exhibiting alignment of grown WSe ₂ crystals with the underlying graphene lattice	39
3.5	Computed reflectivity spectrum of 3ML freestanding graphene plotted together with the band structure of graphite	41
3.6	Computed reflectivity spectrum of 3ML freestanding h-BN plotted together with the band structure of bulk h-BN	43
3.7	Computed reflectivity spectra of 1, 2, and 3ML freestanding WSe ₂ plotted together with the band structure of bulk WSe ₂ and experimentally measured WSe ₂ reflectivity curves	45
4.1	Interlayer transport in WSe ₂ on epitaxial graphene and quasi-freestanding epitaxial graphene measured by conducting-AFM, showing great variation in the two cases	50
4.2	Side-view atomic structures of epitaxial graphene on SiC and quasi-freestanding epitaxial graphene on SiC, showing the effect of hydrogen passivation on the buffer layer at the interface of graphene and SiC	51
4.3	LEEM images, reflectivity, and extracted relative work functions from WSe ₂ on epitaxial graphene and WSe ₂ on quasi-freestanding epitaxial graphene	53
4.4	Summary of extracted ΔW values from WSe ₂ -EG _{PH} and WSe ₂ -EG _{FH} samples	54
4.5	Band diagrams illustrating the change in band alignment produced by charge transfer effects at the WSe ₂ -epitaxial graphene interface	57
4.6	Model of equilibrium electrostatic potential and band alignment between regions of EG _{PH} covered by WSe ₂ and neighboring bare EG _{PH} regions	58
4.7	Schematic of electrical characterization using conducting-AFM to measure current through WSe ₂ -epitaxial graphene, with tunneling in one case and ohmic contact in the other	60
5.1	LEEM image of MoSe ₂ formed on epitaxial graphene by molecular beam epitaxy, and reflectivity spectra showing large work function differences between the MoSe ₂ and graphene	64
5.2	Calculated hole density of MoSe ₂ as a function of nominal electron density in supporting epitaxial graphene before charge transfer	65

5.3	Model of equilibrium electrostatic potential and subsequent band alignment between regions of epitaxial graphene covered by MoSe ₂ and neighboring bare graphene regions	67
6.1	Diagram illustrating exact solution to the typical 3D tunneling problem	70
6.2	Scheme for considering interlayer 2D–2D tunneling in an exact manner, including current flowing laterally each electrode to and from contacts	71
6.3	Illustration of the 3D–3D tunneling problem in the Bardeen approach	72
6.4	Illustration of the Bardeen method applied to 2D–2D tunneling . . .	74
6.5	Schematic of the graphene–insulator–graphene tunneling junction and diagrams illustrating the resulting resonant tunneling due to lateral wavevector conservation	77
7.1	Comparison of theoretical tunneling currents as a function of the bias voltage across two graphene electrodes separated by a h-BN insulator, varying coherence length L	88
7.2	Real and complex band structures of hexagonal boron nitride, computed with density-functional theory and from a tight-binding model	91
7.3	Theoretical simulation of a GIG device with a back gate, using relaxed momentum conservation and thus exhibiting no resonant tunneling .	94
7.4	Measured current–voltage characteristic from a GIG device fabricated with CVD graphene and h-BN, and theoretical simulations of the same device	96
7.5	Raman spectra obtained from monolayer graphene before and after processing steps leading to increased disorder, as evidenced by enhanced D and D' peaks	96
7.6	Comparison of measured and simulated resonant tunneling characteristics in a gated graphene–insulator–graphene transistor, with computed currents exhibiting the effects of crystal misorientation between the layers	98
7.7	Intersection of graphene bands from two electrodes with nonzero misorientation	99
8.1	Schematic illustration of BLG–h-BN–BLG tunneling transistor with band diagrams exhibiting multiple resonances	103
8.2	Calculated tunnel current density versus interlayer bias between undoped graphene bilayers for a range of gate voltages	104
8.3	Band diagram and densities-of-states for bilayer graphene tunneling illustrating overlap of van Hove singularities	105
8.4	Simulated low-voltage tunneling current between bilayer of graphene showing a number of small features due to band-edge alignment . . .	106
9.1	Photograph of Wentworth PML8000 probe station and micromanipulator system, modified to perform transfers of exfoliated 2D crystals .	111

9.2	LEEM images and relative work function map of exfoliated WSe ₂ on few-layer epitaxial graphene showing large work function differences between the WSe ₂ and graphene	113
C.1	Approximate bands around the <i>K</i> -point of a transition metal dichalcogenide	127
C.2	Approximate total density of states in a transition metal dichalcogenide	129
C.3	Approximate total carrier density in a transition metal dichalcogenide	130

What could we do with layered structures with just the right layers? What would the properties of materials be if we could really arrange the atoms the way we want them? They would be very interesting to investigate theoretically. I can't see exactly what would happen, but I can hardly doubt that when we have some control of the arrangement of things on a small scale we will get an enormously greater range of possible properties that substances can have, and of different things that we can do.

—R. P. Feynman, “There’s plenty of room at the bottom,” 1959

Chapter 1

Introduction

The periodic arrangement of atoms known to physicists as the solid state has long been the playground of condensed matter physicists, materials scientists, electrical engineers, and the various other experts involved in the fields of nanoscience and nanotechnology. In the atomically thin limit, that is, a single sheet of atoms arranged in a crystalline lattice, the physics that govern particle and quasiparticle behavior are compressed from the three spatial dimensions we live in down to two. In this state, many new and interesting phenomena emerge as a result of the reduced dimensionality, and it is the physics of such two-dimensional materials that concerns this thesis.

Living in a three-dimensional world affords us an additional degree of freedom when dealing with two-dimensional materials. By controlling the physical conditions and geometry of individual two-dimensional layers with three-dimensional forces, effects, and substrates, we are able to influence the behavior in two dimensions to great effect. Even the simple act of stacking several two-dimensional layers on top of one another to form a layered structure can cause dramatic changes in the properties of the individual layers, in addition to the composite layered structure as a whole. In this thesis, I consider a few select layered structures of dissimilar two-dimensional materials, two-dimensional *heterostructures*, and investigate interlayer interactions that occur between them from the framework of quantum tunneling.

The following sections of this introductory chapter provide background material pertaining to the field of two-dimensional materials and quantum tunneling from the standpoint of resonant behavior. The thesis contains a mix of experimental observations and results from computations and simulations of physics. Chapter 2 covers a few of the major experimental techniques that are employed in the scope of this work, outlining the method of low-energy electron microscopy and its utility in atomically thin materials research. These methods are applied to thin heterostructures of tungsten diselenide and epitaxial graphene in Chapter 3, where a novel technique for counting the number of atomic layers is presented. Chapter 4 covers the topic of tunneling transport in similar structures, specifically identifying two distinct cases

of electrical transport between the tungsten diselenide and graphene based on the method of preparation. Heterostructures of molybdenum diselenide and epitaxial graphene are studied in Chapter 5, wherein the experimental methods developed in the thesis are utilized to measure the defect density of the crystals.

Additional background for the theory of tunneling between two-dimensional layers is outlined and extended to include realistic calculations of the electrostatics in Chapter 6. Chapters 7 and 8 carry this work forward by applying the theory to the cases of tunneling between monolayers of graphene and bilayers of graphene in great detail. In Chapter 9, a discussion of ongoing activities related to state-of-the-art assembly of interlayer tunneling heterostructures and devices is provided along with an outlook toward future prospects. Finally the results of the entirety of this work are summarized in Chapter 10. My work in this area has been highly productive in the time that I have had the pleasure of being involved. To this point, portions of the thesis have appeared in published form in Refs. 1–6, as noted in each relevant section.

1.1 Two-dimensional materials: a new paradigm for physics in reduced dimensions

Prior to the first experimental realization of graphene in 2004,[7] it was widely believed that layered materials could not exist in a freestanding, atomically thin form. In fact, Peierls [8], Landau [9], and Mermin [10] each proposed arguments for the fundamental instability of two-dimensional crystals which were highly regarded for many decades. Physics research in two-dimensional solid state systems was therefore confined to quantum wells, quasi-two-dimensional layers of electron gas confined to a narrow geometry in one dimension while extending out laterally in the other two, embedded in bulk (3D) materials.

Within this context, the first explicit demonstration of a stable two-dimensional (2D) material, graphene, was an immense discovery[7, 11] that initiated a new field of research; one that would have great impact on many related fields in a short period of time. From the viewpoint of electronic behavior, graphene is a semimetal, meaning that it conducts electrons freely save for a twice-degenerate point in the band structure that has a vanishing density-of-states. Apart from this detail, in normal conditions the electrons in graphene naturally behave as a two-dimensional electron gas (2DEG), which is in stark contrast to the interfacial engineering required in many conventional quantum well systems in order to produce 2DEG physics. Since the electrons in graphene are quantum-mechanically confined to the 2D layer, it is 2D physics that they obey.

Due to the relative ease with which 2D materials could be synthesized, the field of 2D materials research quickly expanded beyond graphene to include insulating hexagonal boron nitride, semiconducting MoS₂, and superconducting NbSe₂,[12–14] followed by many others.[15, 16] Each of these materials provides a platform for

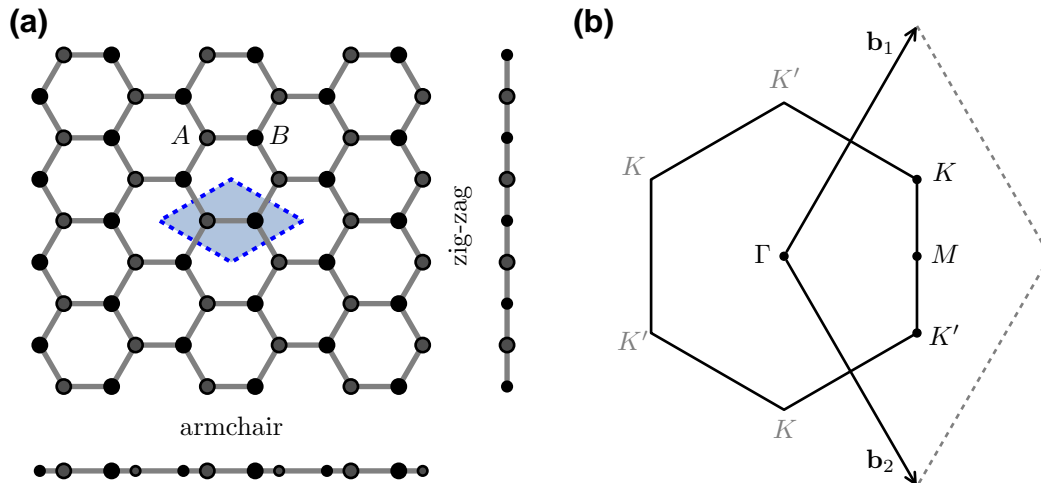


Figure 1.1: (a) Atomic structure of graphene viewed from the out-of-plane direction, with side-views also given along two edges (armchair and zig-zag). There are two carbon atoms per unit cell (shaded area), each belonging to a triangular sublattice A or B . (b) First Brillouin zone (BZ) of the graphene lattice in reciprocal space. Inequivalent symmetry points K and K' exist at the six corners of the BZ, whereas M occurs at the midpoint between neighboring K and K' points.

investigating interesting and novel physics, but it is the combination of such materials in particular arrangements, two-dimensional *heterostructures*, that enables the greatest number of possibilities. As Feynman proposed in his now-famous lecture in 1959, “There’s plenty of room at the bottom,” layered heterostructures in particular are expected to produce new properties and phenomena that are not possible in the constituent materials alone.[17] This was a great insight, put forth at a time when fabrication of such structures was well out of the realm of possibility. After many decades of progress in the field, a catalog of 2D materials and advanced methods for synthesis of these materials into layered structures are finally available. With these elements in place, it is the subject of this thesis to consider a few such structures and, specifically, tunneling phenomena that may occur between vertically-stacked layers of 2D crystals.

1.1.1 Graphite in the few-layer limit

The basic properties of atomically thin graphite were first derived by Wallace in 1947, wherein the bands of a single atomic layer of graphite (later designated *graphene*) were calculated analytically by the tight-binding method and subsequently used to derive properties of bulk graphite.[18] In this work, Wallace showed that the planar

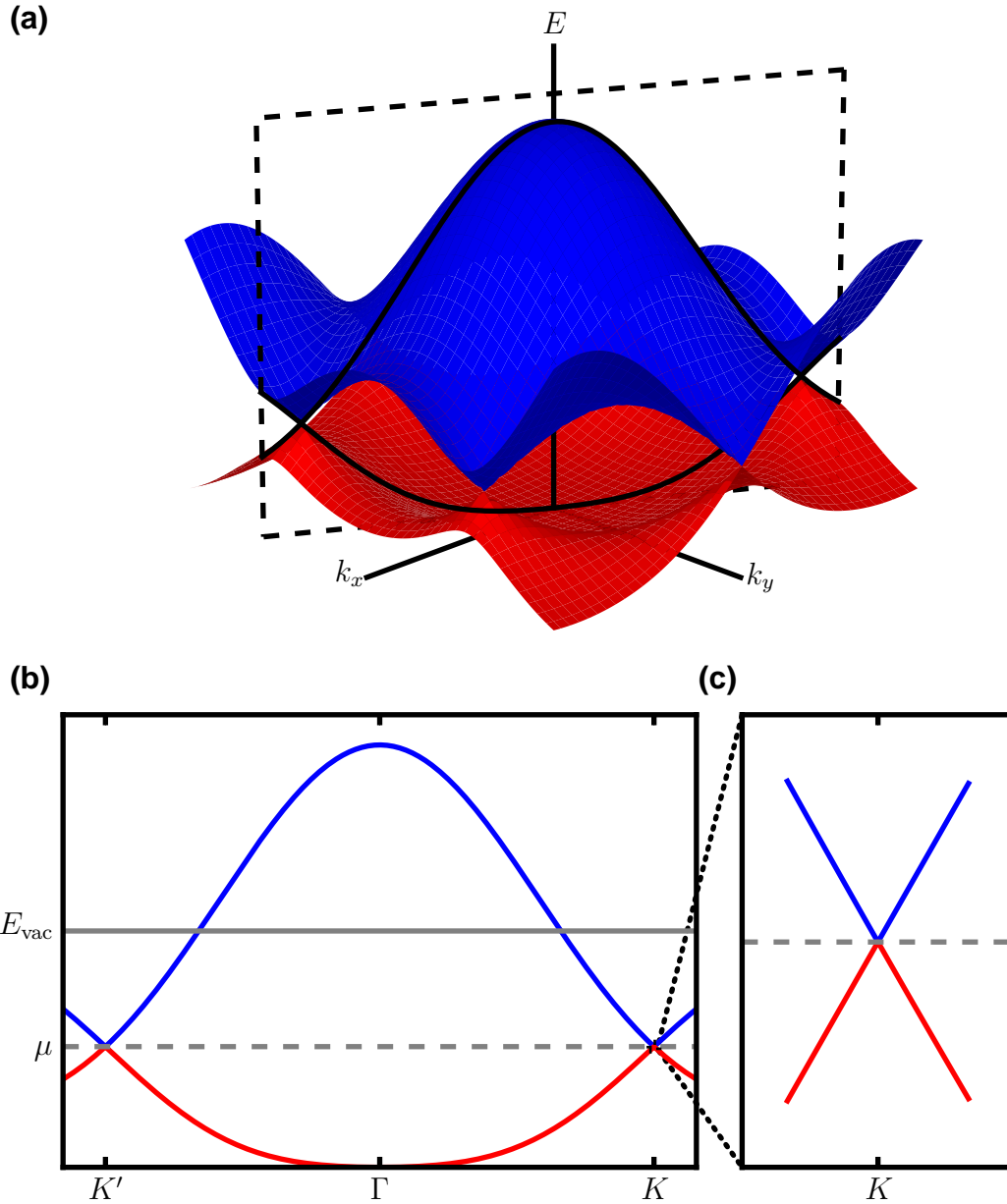


Figure 1.2: (a) Band structure of monolayer graphene produced by the tight-binding method with nearest-neighbor hopping energy $t = 2.8 \text{ eV}$ and next-nearest-neighbor hopping $t' = -0.4 \text{ eV}$. The conduction and valence bands touch at the six corners of the first Brillouin zone, leading to semimetallic behavior. (b) Slice of the band structure taken from the dashed box in panel (a) along the line of symmetry $K' - \Gamma - K$, with the conduction and valence bands in blue and red, respectively. The Fermi level and vacuum level for neutral graphene are labeled as μ and E_{vac} . (c) Blow-up of the detailed bands near the Dirac point, where $E(k_{\parallel})$ is linear and the conduction and valence bands touch.

arrangement of carbon atoms in a honeycomb lattice (Fig. 1.1) produced unusual semimetallic behavior near the Fermi energy for neutral graphene (Fig. 1.2). In a straightforward tight-binding description, orbitals of the two basis atoms A and B , each of which decorate a triangular lattice, are parameterized by nearest-neighbor hopping energy t (from sublattice A to sublattice B) and next-nearest-neighbor hopping energy t' (hopping within the same sublattice). This description permits an analytical form for the band structure (the energies of allowed states as a function of lateral wavevector),[18, 19]

$$E_{\pm}(\mathbf{k}) = \pm t\sqrt{3 + f(\mathbf{k})} - t'f(\mathbf{k}),$$

$$f(\mathbf{k}) = 2\cos(k_y a) + 4\cos\left(\frac{k_y a}{2}\right)\cos\left(\frac{\sqrt{3}}{2}k_x a\right), \quad (1.1)$$

which is shown for the first Brillouin zone(BZ) in Fig. 1.2(a),¹ with lattice constant $a = 2.46 \text{ \AA}$.

The primary result of this simple calculation is that the conduction and valence bands (+ and - signs in Eq.(1.1), respectively) touch at six points, and most importantly, the energy varies linearly with wavevector near these points, as shown in Fig. 1.2(c). The linear dependence can be written down explicitly by expanding Eq. (1.1) around $\mathbf{k} \rightarrow \mathbf{K}$ (or \mathbf{K}'), where \mathbf{K} (\mathbf{K}') is a vector pointing to the high-symmetry point K (K') at the corner of the BZ, where the bands touch,

$$E_{\pm}(\mathbf{q}) \approx \pm v_F |\mathbf{q}| + \mathcal{O}((q/K)^2), \quad (1.2)$$

where $\mathbf{q} \equiv \mathbf{k} - \mathbf{K}$ and $v_F \equiv \sqrt{3}ta/2$ is the *Fermi velocity*. The fact that electronic behavior in this regime is governed by a linear *dispersion* relation ($E \propto q$), typical of *massless* particles, is a miraculous result, and a significant departure from the usual dispersion of electrons, $E \approx k^2/2m$ with effective electron mass m . Moreover, the Fermi velocity v_F does not depend on energy at all, whereas it is usually $v = k/m \approx \sqrt{2E/m}$. In fact, v_F is a constant value near the K and K' symmetry points in graphene, speeding electrons along at close to $v_F \approx c/300 \approx 1 \times 10^6 \text{ m/s}$. [18, 19] Thus the electrons in graphene behave as massless particles with linear dispersion.

This analysis can be taken a step further by noting that a linear dispersion directly results from a Dirac-like Hamiltonian in two dimensions,[19, 20]

$$H_K = v_F \boldsymbol{\sigma} \cdot \mathbf{k}, \quad (1.3a)$$

$$H_{K'} = v_F \boldsymbol{\sigma}^* \cdot \mathbf{k}, \quad (1.3b)$$

around the K and K' points, where \mathbf{k} is now relative to an origin placed at K or K' , utilizing the Pauli matrices $\boldsymbol{\sigma} = (\sigma_x, \sigma_y)$ and $\boldsymbol{\sigma}^* = (\sigma_x, -\sigma_y)$. The eigenenergies both

¹In this section, units are selected such that $\hbar = 1$.

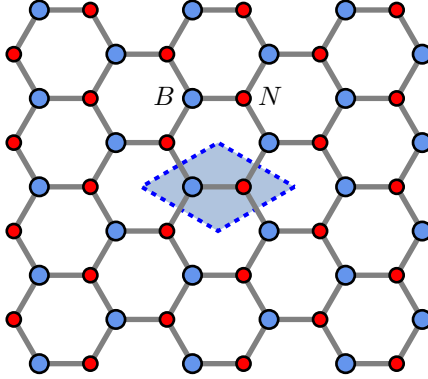


Figure 1.3: Atomic structure of monolayer hexagonal boron nitride (h-BN) viewed from the out-of-plane direction. There is one boron atom (blue) and one nitrogen atom (red) per unit cell (shaded area), populating two inequivalent triangular sublattices. The in-plane lattice constant of h-BN is 2.50 \AA , close to 1.6% larger than that of graphene, leading to an approximate 1.6% *reduction* in the size of the Brillouin zone in reciprocal space, and hence smaller diffraction patterns by the same amount.

copies of this Hamiltonian are $E = \pm v_F k$, as in the linear part of Eq. (1.2), and the eigenstates (around K and K' , respectively) have the form

$$\psi_{\pm, \mathbf{K}}(\mathbf{k}) = \frac{1}{\sqrt{2}} \begin{pmatrix} e^{-i\theta_{\mathbf{k}}/2} \\ \pm e^{i\theta_{\mathbf{k}}/2} \end{pmatrix}, \quad (1.4a)$$

$$\psi_{\pm, \mathbf{K}'}(\mathbf{k}) = \frac{1}{\sqrt{2}} \begin{pmatrix} e^{i\theta_{\mathbf{k}}/2} \\ \pm e^{-i\theta_{\mathbf{k}}/2} \end{pmatrix}. \quad (1.4b)$$

These wavefunctions are valid for describing electrons in graphene when $|\mathbf{k}| \ll |\mathbf{K}| = 4\pi/3a$, and the Dirac-like nature of the electrons in this regime leads to the term *Dirac fermions*. As a final point of nomenclature, the six points at which the conduction and valence bands touch are referred to as the *Dirac points*, and the linear bands near these points, *Dirac cones*. There is one valence electron per atomic site in the graphene lattice, and thus the valence band is completely filled and the conduction band empty in neutral graphene at zero temperature. As a result, the Fermi level in these conditions is found at the energy where the bands touch (Fig. 1.2(b)), the so-called charge neutrality point.

1.1.2 Hexagonal boron nitride: an ultraflat wide-band-gap insulator

The semimetallic behavior of graphene is a result of the high symmetry of the lattice of carbon atoms. Specifically, the equivalence of the potentials at the A and B sublattice sites prevents the existence of a band gap, allowing the conduction and valence bands to touch at the charge neutrality point. In contrast to this picture, hexagonal boron nitride (h-BN), although it has the same lattice structure as graphene, possesses two inequivalent atoms per unit cell (Fig. 1.3), lowering the symmetry compared to graphene and thus opening up a band gap in the band structure (Fig. 7.2). As such, h-BN is a wide-band-gap insulator, with a band gap energy near 6 eV.[21] Due to strong, in-plane covalent bonds and weak interlayer interactions, h-BN is a layered material, similar to graphite, and it is highly stable in thicknesses down to a single layer.

Most importantly for graphene studies, however, is that due to its inherent flatness, inertness, and large band gap, h-BN makes a fantastic substrate, encapsulation layer, and tunneling barrier for 2D heterostructures of all kinds. Boron nitride has been shown to increase the flatness of supported graphene (roughness or curvature tend to introduce potential fluctuations in graphene, among other complications),[15] to vastly reduce spatial potential inhomogeneities in the graphene,[22] and to increase the electron mobility in graphene by at least one order of magnitude compared to bulk substrates.[23]

In the scope of this thesis, h-BN will primarily be viewed as a convenient insulating material; a dielectric material with a permittivity close to $4\epsilon_0$, and a tunneling barrier with decay constant $\kappa \approx 6 \text{ nm}^{-1}$, varying slightly in momentum space (see Section 7.3). Insofar as the h-BN serves one function or the other is largely a question of the thickness, with h-BN substrates and gate dielectrics typically utilizing $\approx 20 \text{ nm}$ or so of h-BN layers, whereas tunneling applications require no more than 2 to 6 monolayers to be effective. For studies involving low-energy electron microscopy, it is the high-energy bands (above the vacuum level) that are relevant, and in this regime h-BN can be considered quite similar to graphene, as will be discussed in Section 3.4.

1.1.3 Semiconductors in two dimensions: transition metal dichalcogenides

Shortly after the isolation of graphene in its monolayer form, the first true 2D semiconductor was similarly reduced to two dimensions, MoS_2 . [12] This material, a transition metal dichalcogenide (TMD), possesses strong ionic-covalent bonds within each layer and weak interlayer interactions, similar to graphene and h-BN, however, there are in fact three atomic planes comprising each “monolayer” of TMD, as shown schematically in Fig. 1.4. Each layer of TMD material (with general formula MX_2) is composed

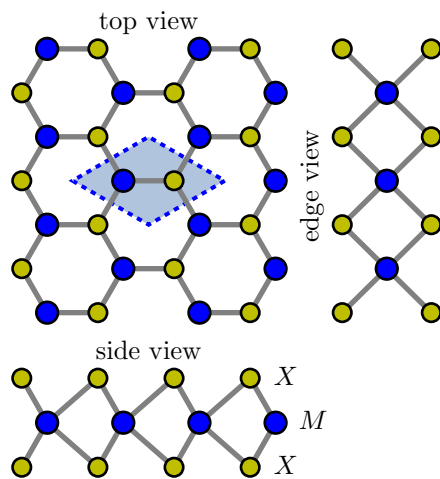


Figure 1.4: Atomic structure of a generic transition metal dichalcogenide with the formula 2H-MX_2 , one with metal M and two chalcogen X atoms per unit cell (for example $M \in \{\text{W}, \text{Mo}\}$, $X \in \{\text{S}, \text{Se}, \text{Te}\}$). Side views emphasize the coexistence of three separate atomic planes; the metallic plane being sandwiched between chalcogen layers. Lattice constants vary depending on the constituents, but are generally about 30% larger than that of graphene, and thus diffraction patterns are easily differentiated from those resulting from graphene.

of a central atomic layer of transition metal atoms (M) in a triangular sublattice sandwiched between two atomic layers of chalcogen atoms (X), with the chalcogens arranged in a trigonal prismatic coordination.² Previous studies of bulk MoS₂ established that it is an *indirect*-band-gap semiconductor, meaning that the conduction band minimum and valence band maximum occur at different points in momentum space. Early work with MoS₂ in the few-layer limit, however, revealed that reducing the number of layers leads to an increasing band gap energy, and strikingly, monolayer MoS₂ obtains a *direct* band-gap, with conduction and valence band extrema occurring at the same location.[14] Neither type of band gap is unusual in conventional semiconductors, but the transition from one type to the other caused by the reduction in dimensionality suggests that this is indeed a class of materials worth investigating.

In fact, there are many unique and superlative properties of TMD materials, most of which are beyond the scope of this thesis. Here, we will primarily be concerned with the utility of TMD materials as 2D semiconductors, with band gaps, electron affinities, and densities-of-states that may prove advantageous for electronic devices, especially tunneling structures. Along those lines, it is worth pointing out that there are several possible phases of TMD crystal structures: 2H, 1T, 1T', and 1Td, each with slightly different arrangement of the metal and chalcogen atoms within each atomic plane. Throughout the thesis, the samples studied are either assumed or revealed to be largely of the 2H (hexagonal) variety, as shown in Fig. 1.4, and thus the distinction will not be made beyond this point.

1.2 Resonant tunneling physics in its various forms

Having established the materials that will enter into the work described in this thesis, it is the task of this section to introduce the tunneling concepts that arise as motivation, and for reference in later chapters. Whereas Chapters 3 and 5 deal primarily with materials characterization, abstracted from the intended purpose of fabricating interlayer tunneling devices, Chapters 4, 7, and 8 involve tunneling directly. The overarching goal of this work has been to design and eventually fabricate interlayer tunneling devices that take advantage of 2D–2D tunneling physics to exhibit novel and desirable electronic behavior. Before we advance to the specific modes of tunneling that appear in the thesis, we must establish the context in which this work is relevant. The term *resonant* tunneling has been used with several, somewhat disjoint meanings in physics and electrical engineering. The observation that these share in common is *negative differential resistance*, but the underlying mechanism that causes this is different in each case. There are whole bodies of literature pertaining to each

² Conceding that one of these layers is technically not atomically thin, one could more precisely call this a *stoichiometric monolayer*, although the distinction is typically irrelevant for situations in which the electronic behavior is still governed by 2D physics. Hence, for the purposes of this thesis, the term *monolayer* will be used to refer to a single stoichiometric monolayer, with three atomic planes.

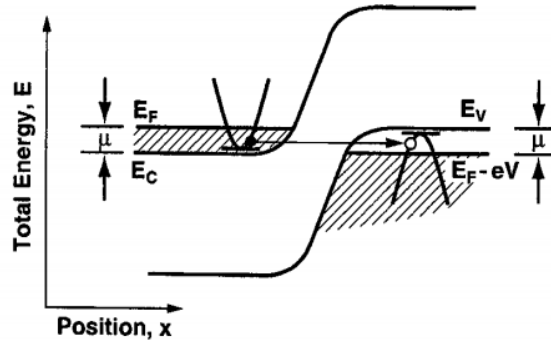


Figure 1.5: Band diagram of an Esaki tunnel diode at resonance. Current tunnels from conduction to valence band through a narrow depletion region in a highly-doped p - n junction. Adapted from Ref. 24.

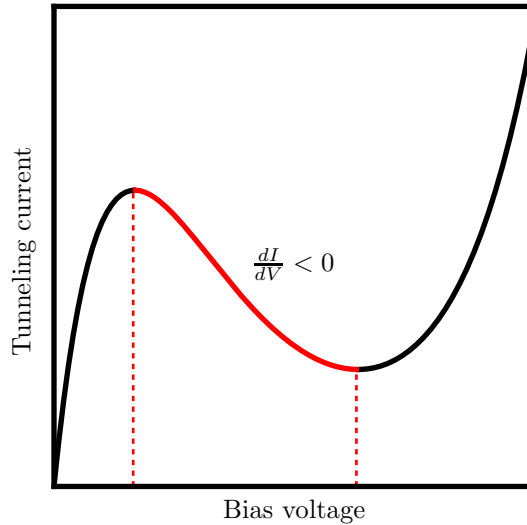


Figure 1.6: Illustration of voltage-driven negative differential resistance (NDR), referring to the red portion of the current–voltage curve, where $dI/dV < 0$. Another form of NDR (current-driven) is also possible, but will not appear in the thesis.

of these mechanisms, so I will only provide a brief overview here for purposes of comparison to the physics that will be discussed in the thesis.

1.2.1 Esaki tunnel diode

The first demonstration of quantum tunneling in a solid state system was, in fact, a form of resonant tunneling observed by Esaki [25]. By measuring the current across highly doped germanium in a p - n junction, Esaki more or less stumbled upon the

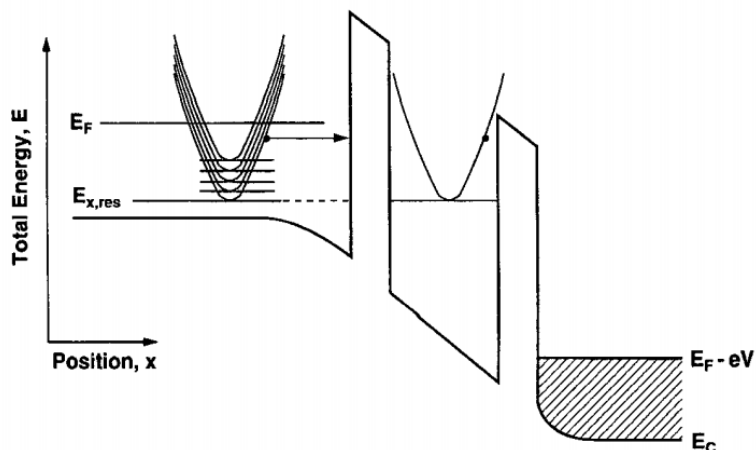


Figure 1.7: Band diagram of a double-barrier resonant tunneling diode (RTD) at resonance. A quantum well is sandwiched between two tunneling barriers with electrodes on the exterior faces. Resonant tunneling occurs for the bias voltage which causes energetic coincidence of the confined state in the quantum well with states in the electrode regions. Adapted from Ref. 24.

phenomenon which now takes his name (and ultimately led to a shared Nobel Prize, no less). With an extremely narrow depletion region between the p and n sides of the junction, carriers can tunnel from the conduction band of the n side to the valence band of the p side (Fig. 1.5). For the special case of very highly-doped n and p regions (so-called *degenerate* doping), the conduction band of the n side is lower in energy than the valence band of the p side at zero bias ($V = 0$). In this configuration, as the bias is increased from zero the window of allowed states for tunneling becomes smaller due to the increasing energy of the conduction band (and the lack of available states in the band gap). This causes the current to *decrease* with increasing voltage for a small range of voltages, a phenomenon known as *negative differential resistance* (NDR), where $dI/dV < 0$, as shown in Fig. 1.6. The concept of NDR is intriguing given that current is generally a monotonically-increasing function of voltage in conventional electronic devices. In practice, this NDR behavior leads to a peak in the tunneling current with respect to voltage; a type of resonant tunneling.

1.2.2 Double-barrier resonant tunneling diode

Double-barrier resonant tunneling is a familiar example of quantum phenomena often taught in courses on quantum mechanics. In such examples, the exact solution of double-barrier tunneling in one dimension is used to show that perfect tunneling transmission can occur for certain energies coincident with states in the central quantum well. A double-barrier resonant tunneling diode (RTD) is an electronic device based on this mechanism that produces NDR in its tunneling characteristic due to

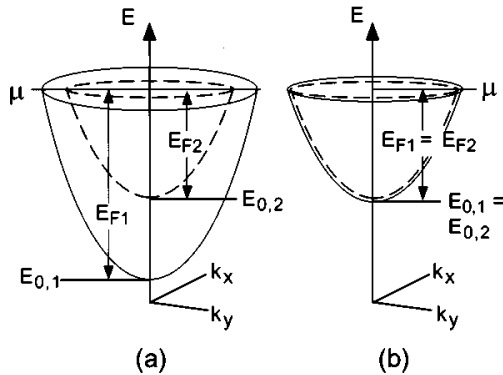


Figure 1.8: Parabolic bands of neighboring quantum wells in momentum space with an applied bias (a) off-resonance and (b) on-resonance, leading to negative differential resistance due to requirement of lateral momentum conservation (k_{\parallel} -conservation). Adapted from Ref. 26.

the non-linear transmission. In this case, reduced dimensionality in a central quantum well region is employed to discretize the available states such that the resulting spectrum in the quantum well possesses a single relevant band. The quantum well is sandwiched by tunneling barriers on either side, with source and drain electrodes on the exterior faces of the tunneling barriers (Fig. 1.7).[24] A bias is applied across the source and drain electrodes, causing modulation of the bands in the electrodes, as well as in the quantum well region. For one bias voltage in particular, the energy of the available band in the quantum well will coincide with a matching bands in the electrodes, causing a peak in the transmission coefficient and subsequent resonant tunneling through the two barriers, from source to drain.

1.2.3 Lateral momentum conservation in two dimensions

Along the lines of using reduced dimensionality to produce resonant quantum effects, moving to two dimensions can provide many opportunities for resonant behavior. One important mechanism that forms a central component of the thesis is resonant tunneling between two separate two-dimensional electron gases (2DEGs) due to lateral momentum (or wavevector) conservation. The first proposals for this phenomenon were devised in the context of quasi-2DEGs in double-quantum-well structures.[26–28] In such a structure, the states of each quantum well are confined to a quasi-two-dimensional volume, causing each band to have well-defined momentum in the lateral directions, but decaying character in the out-of-plane direction (Fig. 1.9). A bias is applied across the two quantum wells, leading to tunneling from one 2DEG to the other. For one particular voltage bias, the bands of each 2DEG will be in complete alignment in momentum space, as in Fig. 1.8(b); this is the resonant tunneling condition. At other biases, the bands will not overlap, as in Fig. 1.8(a), or at

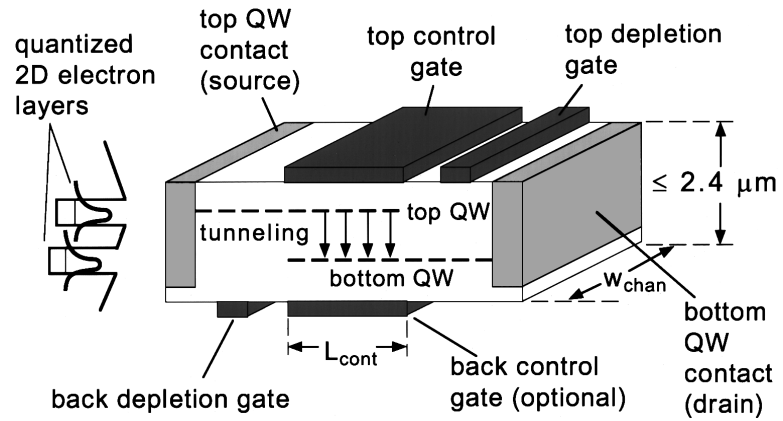


Figure 1.9: Schematic of a 2D–2D tunneling transistor based on a conventional semiconductor heterostructure. Tunneling resonance is provided by the reduced number of states with matching energy and lateral momentum on either side of the tunneling barrier, similar to the graphene–insulator–graphene tunnel junctions presented in Chapters 7 and 8. Adapted from Ref. 26.

least the lines of intersection will be confined to a much smaller number of states, leading to reduced tunneling currents at these other voltages. This manifests as NDR in the tunneling current, similar to the Esaki diode and RTD mechanisms mentioned previously, however, in this case the underlying mechanism responsible is the strict requirement of lateral wavevector-conservation in addition to the usual energy conservation (for elastic transitions) between the tunneling states. Two key properties that enable momentum-conservation to play a role in the transmission are as follows:

1. There must be a greatly reduced number of states with dispersion in the tunneling direction (the 2D requirement), otherwise there will be additional bands which allow tunneling at multiple voltage biases, or even for a voltage continuum, as in 3D crystals.
2. The wavefunctions of each quantum well must be coherent with sufficient lateral extent so as to have well-defined lateral momentum. Localized wavefunctions are diffuse in momentum space and therefore will have significant overlap with states in the opposing electrode at many biases.

These points will arise again in Chapters 6, 7, and 8 regarding a similar mechanism in 2D materials, and therefore further details will be reserved for those sections.

As a final point to differentiate 2D–2D resonant tunneling from Esaki and RTD tunneling, due to the geometry of a 2D–2D device, with the tunneling area exposed on both sides of the junction, electrostatic gates may be easily added above and below the electrodes for modulating the tunneling with a third and fourth external voltage bias (Fig. 1.9). Gate modulation of this sort enables the device to operate as a *transistor* (a three- or four-terminal device) as opposed to a simple *diode* (a two-terminal device). Transistors are highly sought-after components for myriad electronics applications involving switching, logic, and memory, and the ability to regulate NDR as a transistor is very compelling from a circuit perspective.

1.2.4 Many-body effects and excitonic condensates

I will emphasize at this point that the tunneling concepts presented in this thesis deal with *single-particle* effects, that is, tunneling between single-particle states using physics derived from Bloch band theory and its associated machinery. There are, of course, other possible *many-body* effects that could play a role in interlayer tunneling between 2D crystals. It is quite likely that such effects, however, play a secondary role in tunneling transport observed in the standard conditions of electronic components (i.e. at room temperature and above). There is, however, one proposal for interesting many-body tunneling in a heterostructure that is functionally equivalent to the graphene–insulator–graphene tunnel junction presented in the thesis (see, for example, Section 6.2.2). This proposed device also involves interlayer tunneling between graphene sheets separated by a thin insulating barrier, however the underlying

mechanism for tunneling is based on electron-hole (e^-h^+) pairing across the tunnel barrier, an *excitonic* state that behaves as a collection of Bosons due to the integral total spin of each e^-h^+ pair. Whereas individual electrons and holes are Fermions, and therefore cannot occupy the same state simultaneously (the Pauli exclusion principle), the excitonic Boson gas of e^-h^+ pairs may condense below a certain critical temperature (given that there are also roughly equal populations of electrons on one side of the junction and holes on the other), forming a so-called Bose-Einstein condensate. In this configuration, the condensate can allow rapid tunneling through the junction due to the highly correlated state of the carriers.[29, 30] However, with modulation in the bias the condensate is expected to degrade (due to charge imbalance), and thus the tunneling current will reduce, leading to NDR.

Though these effects are undeniably intriguing and worthy of pursuit, presently such effects have not been observed in 2D devices. On the other hand, the predictions of resonant tunneling due to single-particle effects in graphene (Refs. 2, 31, 32) and bilayer graphene (Refs. 33, 34) as presented in the thesis *have* been observed in the time since this work began. Therefore, it is single-particle effects that will be the focus of the thesis, and beyond this section many-body effects will not be considered further.

Chapter 2

Experimental methods

With the goal of studying 2D materials and layered heterostructures composed of 2D materials, the primary experimental tool I employ is the low-energy electron microscope (LEEM). In the following sections, I describe the apparatus and various modes of operation as they pertain to investigations of 2D materials. Whereas the imaging and diffraction modes described in Sections 2.1.1 and 2.1.2 are relatively commonplace amongst users of LEEM, the spectroscopic techniques introduced in Sections 2.1.3 and 2.2 are less commonly known, and a portion of the work described in this thesis involves advancing these methods as needed for applications to 2D surface science. The development of low-energy electron reflectivity as a method for probing 2D materials is a high priority in our group, and as such it is also an area in which we have collectively attained a level of expertise. There are not many LEEM systems, globally; partly due to the high cost of commercial systems (and the even greater challenge of designing and building one), and partly due to lack of awareness regarding the advantages of LEEM for studying 2D materials, not to mention surfaces in general. Therefore it is an additional goal of this thesis, in a small way, to advertise the qualities of LEEM for studying 2D heterostructures to the broader community.

2.1 Low-energy electron microscopy and reflectivity

A low-energy electron microscope (LEEM) uses a broad beam of low-energy electrons to image surfaces by capturing the elastically backscattered electrons with a series of electron lenses.^[35] Electrons are emitted from an electron gun cathode and accelerated through a large negative potential before entering a column of electromagnetic focusing lenses and deflectors, the illumination column (see Fig. 2.1). The beam is curved through a magnetic beam separator before being decelerated to low-energies between the objective lens and sample surface. The reflected electrons pass back through the objective lens and are curved away from the incident beam by the magnetic beam separator before entering the imaging column, which uses a second set of lenses and deflectors to project the magnified image onto a microchannel plate

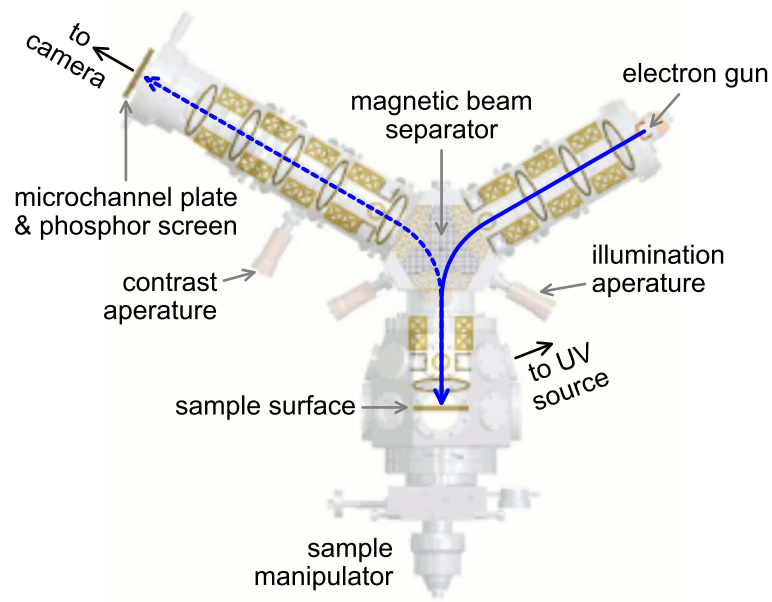


Figure 2.1: Diagram of a low-energy electron microscope with 60° beam deflection design. In contrast to other common electron microscopes, there is a magnetic prism array separating the illumination and imaging electron beams. Electrons are accelerated from the gun cathode through a high-voltage potential and decelerated just before reflecting from the sample surface, with a small variable sample bias applied on top of the decelerating voltage. Reflected and diffracted electrons pass back through the beam separator and are refocused into a magnified image on a phosphor screen and the end of the imaging column. An illumination aperture may be used to reduce the illuminated region on the same surface (typically utilized for selected-area diffraction mode). Diffraction patterns occur in the back focal plane of the objective lens, where a contrast aperture may be inserted for diffraction-contrast and dark-field imaging. With the electron beam turned off, a UV source may be used for photoemission electron microscopy.

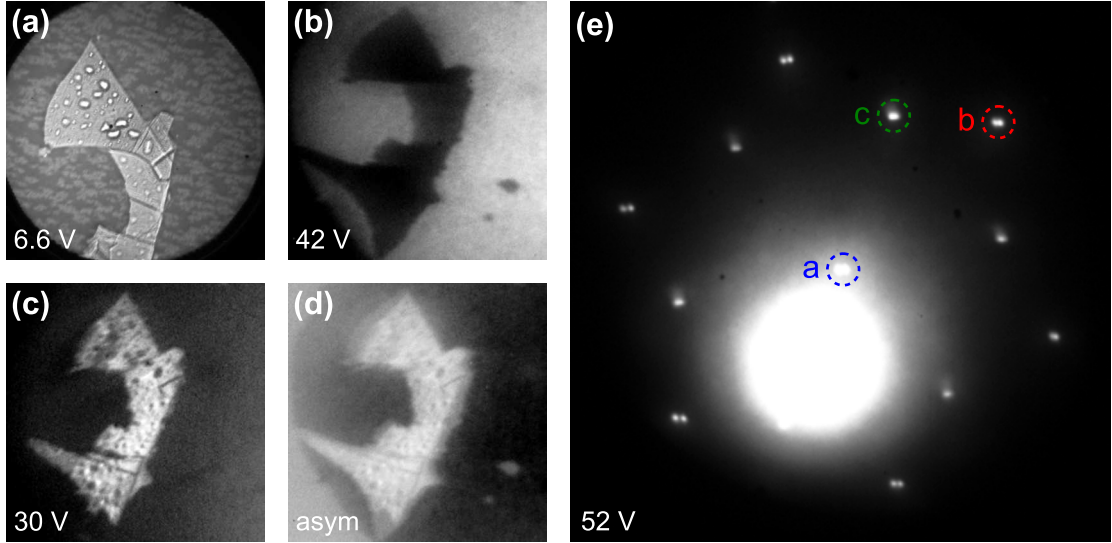


Figure 2.2: (a) Specular bright-field LEEM image of exfoliated WSe_2 flake on epitaxial graphene on SiC. Field-of-view is approximately $50\ \mu\text{m}$. (b) Dark-field (diffraction-contrast) image formed by placing a contrast aperture on the (01)-spot of the graphene diffraction pattern. Bright regions correspond to graphene whereas the dark shadow is covered by WSe_2 . (c) Dark-field image formed by placing a contrast aperture on the (01)-spot of WSe_2 , with the WSe_2 showing as a bright patch in a dark background of graphene. (d) Diffraction asymmetry image produced by taking the normalized difference of dark-field intensities $A = (I_{\text{Gr}} - I_{\text{WSe}_2}) / (I_{\text{Gr}} + I_{\text{WSe}_2})$. (e) Diffraction pattern of the regions shown in panels (a)–(d). Encircled spots indicate the positions of the contrast aperture used to generate the images in panels (a)–(c), as labeled.

and phosphor screen. Depending on the lens currents, several modes of operation are possible.

2.1.1 Bright-field and dark-field imaging

For crystalline samples, in addition to 180° -backscattering, some of the electrons incident on the sample surface are diffracted. In other words, some electrons scatter from a reciprocal lattice vector of the periodic potential on the surface and thus obtain a finite in-plane momentum component. In imaging mode, typically only the normally-reflected electrons are used to form the final image, as in Fig. 2.2(a). To achieve this, a metal *contrast aperture* is centered on the specular (00)-spot of the diffraction pattern that forms in the back focal plane of the objective lens, as in circle “a” in Fig. 2.2(e). This aperture blocks electrons with in-plane momentum, allowing the final image to be formed using only the normally-reflected electrons.

Contrast in bright-field mode typically comes from differences in the interactions

between low-energy electrons and the top few atomic layers on the sample surface. These interactions can in general be quite complex, or at least material dependent. Primarily, contrast will arise due to the partial absorption of incident electrons into the sample due to the presence of surface states and/or inelastic processes. In addition to providing spatial contrast across sample surfaces, these interactions often have a well-defined energy dependence that can provide a great deal of information, as discussed in Section 2.1.3 and utilized in Chapters 3 and 4.

By centering the contrast aperture on a diffracted spot, it is possible to form an image using only electrons diffracted in the direction of the selected spot. This is called dark-field or diffraction-contrast imaging, and can be useful for discerning between surface features with differing crystal structures or orientations. For example, the diffraction pattern in Fig. 2.2(e) is the result of separate graphene and WSe₂ lattices in the illuminated region. By moving the contrast aperture to each encircled region and capturing a real-space image, separate bright-field and dark-field images are recorded, as shown in panels Figs. 2.2(a)–2.2(c). The dark-field images show only electrons which pass through the particular spot that is centered in the aperture, and thus are dark wherever electrons are diffracted in a different direction. By taking the normalized difference of two dark-field images, $A = (I_{\text{Gr}} - I_{\text{WSe}_2}) / (I_{\text{Gr}} + I_{\text{WSe}_2})$, a diffraction *asymmetry* image is formed, as in Fig. 2.2(d), which eliminates contrast that does not originate from well-defined diffraction.

2.1.2 Electron diffraction in a LEEM

For surfaces with sufficient periodicity, a portion of the incident electrons will obtain an in-plane momentum component after scattering, traveling along a diffracted trajectory toward the objective lens. The set of diffracted beams from a given surface is called the diffraction pattern, and appears in the back focal plane (the diffraction plane) of the objective lens. By adjusting the lens currents in the imaging column, the image in the back focal plane of the objective lens can be projected onto the imaging plane of the microscope in lieu of the real-space image of the surface. The result is that the diffracted electron beams can be imaged directly, as shown in Fig. 2.2(e). The ability to switch between real-space and momentum-space imaging in LEEM is similar to transmission and diffraction modes in a transmission electron microscope. Of course, these are backscattered electrons instead of transmitted ones, and the energies used for diffraction in a LEEM system are typically between 30 eV and 500 eV, and hence the technique is called *low-energy electron diffraction* (LEED).

There are, in fact, dedicated LEED systems which do not require the complex arrangement of electron lenses provided in a LEEM, but there are several advantages to measuring diffraction patterns in a LEEM as opposed to a standalone LEED system. The primary advantage of the LEEM optics is that they permit the incident beam to be focused to a small region of the surface through the use of an *illumination aperture* (see Fig. 2.1) in imaging mode. By this method, a specific region of the surface can be

selected for diffraction imaging, so as to obtain a *local* diffraction pattern, so-called selected-area diffraction or μ LEED.

The latter technique enables micrometer-scale analysis of crystallinity, crystal orientation, and even atomic structure in some cases (through indirect methods). By relocating the illuminated region and successively capturing μ LEED patterns it is possible to compare lateral differences in crystal structure. However, for layered 2D structures in particular, the finite (albeit short) depth of electron penetration into the surface allows direct comparison of vertically stacked crystals, for example to measure crystallographic misorientation (rotation) or differences in lattice constant. With these capabilities at our disposal, μ LEED provides excellent complementary information for surface studies of 2D materials and heterostructures in LEEM.

2.1.3 Spectroscopic analysis with low-energy electron reflectivity

Low-energy electrons, that is, electrons with kinetic energy $E < 500$ eV for the purposes of this thesis, interact with surfaces through elastic, quasielastic, and inelastic channels.[35] Especially at the lowest energies, $E < 10$ eV, elastic backscattering and inelastic scattering dominate over forward scattering processes. Unlike electrons with higher energies, these interactions cannot be described by physics assuming weak inelastic scattering or the first Born approximation of general scattering theory. The influence of neighboring atoms on atomic potentials is relevant for electrons with energies less than ≈ 100 eV, and as the incident electron energy decreases further, the effects of charge–charge (correlation) and spin–spin (exchange) interactions become increasingly important.[36] These effects are the relevant ones for the critical range of energies used for LEEM imaging, between 0 and 20 eV.

In crystalline solids, the periodic lattice of atoms produces a set of energy bands that depend on crystal wavevector, $E_n(\mathbf{k})$, the band structure. Forbidden ranges of energy without states, band gaps, do not in principle admit incident electrons, and should therefore reflect all electrons of energy within the band gap. However, quasielastic electron–phonon scattering can provide a change in momentum with negligible change in energy, allowing the scattered electrons to find allowed states in the solid.[35] Additionally, the finite penetration depth of incident electrons, even with energies in a band gap, opens up the possibility of inelastic processes that further reduce elastic backscattering. For these reasons, total reflection of incident low-energy electrons is not typically observed. Incident low-energy electrons with energy and wavevector matching allowed states on the surface may be transmitted into the solid, leading to reduced reflectivity. As a result of these effects, reflectivity of low-energy electrons from crystalline surfaces in general depends on details of the band structure, lattice excitations, and available inelastic processes.

Electron beam energy in LEEM is modulated by a small bias V applied between the electron gun cathode and the sample surface (see Fig. 2.3). In our system, an

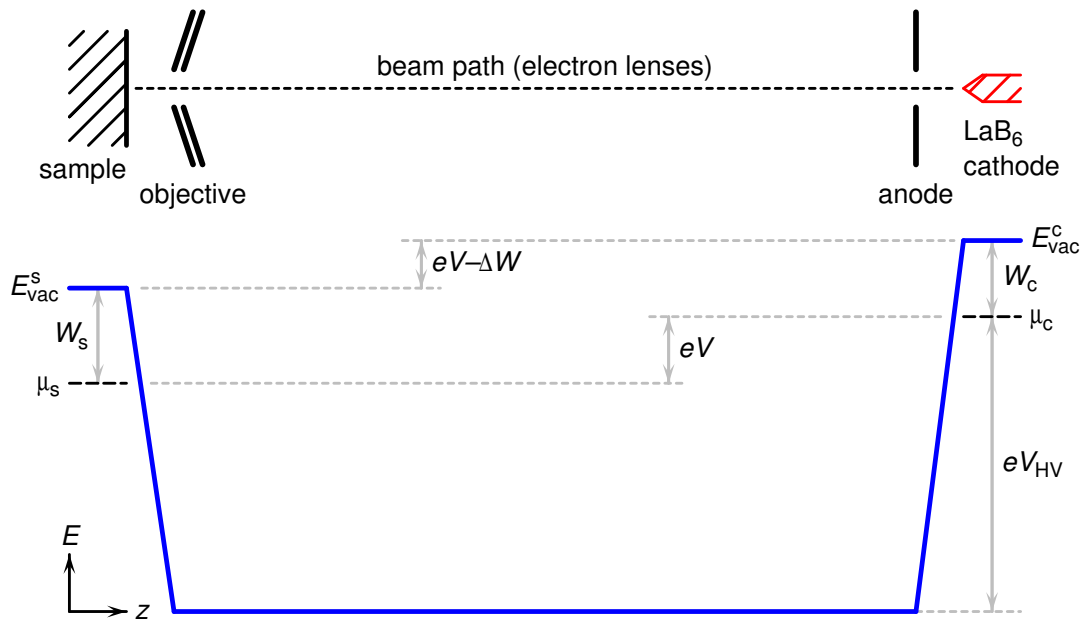


Figure 2.3: Electrostatic potential model of a low-energy electron microscope, relating the high-voltage bias V_{HV} and sample bias V to the Fermi levels μ_s , μ_c and vacuum levels E_{vac}^s , E_{vac}^c of the sample surface and electron gun cathode, respectively. Work functions of the sample and cathode are denoted W_s and W_c . A simplified schematic of the sample, objective lens, gun anode and cathode along the illumination beam path is shown above as it relates to the potentials below, ignoring the effects of the electron lenses and beam deflectors. Neither the spatial nor energy range is shown to scale.

Elmitec LEEM III, electrons are first produced by thermionic emission from a LaB₆ crystal cathode which is held at a high voltage $V_{\text{HV}} = -20 \text{ kV}$ with respect to a nearby anode cylinder. The thermionic electrons are accelerated through this large potential in order to allow efficient lensing by a series of electromagnetic lenses that make up the illumination column of the microscope. To prevent backstreaming of electrons through the various electron-optical stages, the entire system is operated at ultra-high vacuum (UHV), with pressures in the beam column typically less than $1 \times 10^{-10} \text{ Torr}$. Just before the electrons reach the surface of the sample, they are decelerated to low energies by a 10^4 V/mm field emanating from the objective (cathode) lens to the sample surface. The small sample voltage V is floated on top of the high-voltage potential and allows the beam energy to be tuned around the vacuum level of the sample surface. Specifically, the sample and gun cathode Fermi levels may be written as

$$\mu_s = e(V_{\text{HV}} - V) \quad (2.1a)$$

$$\mu_c = eV_{\text{HV}}, \quad (2.1b)$$

respectively. The vacuum level, the lowest unbound (resting) free-electron level at each location, is related to the Fermi level in the usual way,

$$E_{\text{vac}}^s = \mu_s + W_s \quad (2.2a)$$

$$E_{\text{vac}}^c = \mu_c + W_c, \quad (2.2b)$$

for the sample surface and gun cathode, respectively, with work functions W_s , W_c of the sample and cathode crystal. Note that in general the work function is a local quantity, and therefore the vacuum level is also defined locally on the surface of a solid, even in Fermi equilibrium. This point is discussed and utilized in Chapter 4 as it relates to LEEM measurements.

From Eqs. (2.1) it is clear that the sample bias is proportional to the difference in Fermi levels, $eV = \mu_c - \mu_s$. Using this and the difference of Eqs. (2.2), we find

$$E_{\text{vac}}^c - E_{\text{vac}}^s = eV - \Delta W, \quad (2.3)$$

where we have defined the difference in sample and cathode work functions,

$$\Delta W \equiv W_s - W_c. \quad (2.4)$$

Due to the thermionic nature of emitted electrons from the gun cathode, the electron beam energy is primarily concentrated near the vacuum level of the cathode, E_{vac}^c . Details of this energy distribution will be reserved for Chapter 4. Here, it is sufficient to consider the emitted electrons having energy equal to E_{vac}^c , and therefore arriving at the sample surface with kinetic energy equal to the difference in vacuum levels given in Eq. (2.3), and as shown in Fig. 2.3. Therefore, the kinetic energy of incident electrons is indeed modulated by the sample bias, V , but shifted by $\Delta W/e$, an important

distinction that is relevant for any comparison of measured reflectivity to energy bands or quantities derived from energy bands. Finally, for small positive biases, 0 to 20 V, LEEM electrons are generally probing unoccupied states that exist slightly above the vacuum level of the sample surface. These states are “low-energy” insofar as they correspond to slow free electrons, i.e. with low kinetic energy. However, from the perspective of states in the solid itself, these states are typically several electronvolts above the energy range of electronic transport phenomena and would therefore be considered “high-energy” states of the solid.

To study these states, spectroscopic *low-energy electron reflectivity* (or simply *reflectivity*, in this thesis) is utilized. With a clean sample surface in focus, a series of images is captured while sweeping the sample bias, typically from a small negative bias, for example -5 V (slightly below the sample vacuum level, depending on work functions), up to 15 V or 20 V. The sample voltage is swept in 0.1 V increments, resulting in ≈ 200 to 250 images over the course of an hour or so (depending on beam intensity and desired signal-to-noise). This procedure is performed with a contrast aperture (one of three sizes, for choosing the radius of allowed diffraction trajectories) in place over the specular (00)-spot in the diffraction plane.

The resulting series of images allows a reflectivity spectrum, that is, reflected intensity as a function of sample bias $I(V)$, to be extracted from each pixel in the image set during post-processing, as shown in Figs. 2.7 and 3.1. In practice, reflectivity from groups of neighboring pixels are summed or averaged together to improve signal-to-noise and to relate extended regions with similar reflectivity signature. Low-energy electron reflectivity is also sometimes referred to by other groups as LEEM- $I(V)$ since $I(V)$ curves are extracted from LEEM images directly, and to contrast with another method historically called LEED- $I(V)$, which involves extracting *diffracted* intensity from a series of LEED patterns with varying sample bias. The latter technique may be performed in a LEEM, but is also possible in a conventional LEED system which has a vastly simplified design and no imaging capability.

The process of extracting spectroscopic information by varying the cathode-sample bias in LEEM is analogous to sweeping tip-sample bias in scanning tunneling spectroscopy (STS), a well-known technique for studying electronic states on surfaces.[37–39] As a point of distinction, in the former case the states that are spectroscopically probed are unoccupied ones above the vacuum level, whereas in the latter case the states are near the Fermi level and may be occupied or unoccupied depending on the direction of tunneling current. In terms in experimental execution, the greatest difference between the two methods is that low-energy electron reflectivity spectra are obtained for an entire illuminated region all at once, allowing arbitrary point-to-point comparison during data analysis. For equivalent analysis using scanning tunneling microscopy (STM), an STS spectrum must be individually recorded for each location in a rastered grid, requiring large data collection times and high stability of surfaces and experimental conditions. This final point is a great advantage for LEEM-based spectroscopy methods, which allows rapid and routine surface studies

that would otherwise be impractical or impossible with scanning probe methods.

2.2 Relative work-function extraction from reflectivity

As a final point related to spectroscopic techniques enabled by low-energy electron reflectivity, in this section an additional method is introduced that utilizes the very low energy part of the spectrum to measure spatial variations in surface electrostatic potentials. In the scope of the thesis, these methods were developed to allow comparison of work functions between the constituent layers of 2D heterostructures. Highlights of these works appear in Sections 5.1 and 4.3, but the method is generally applicable to electron reflectivity analysis, and is therefore employed in most cases where reflectivity is concerned in the thesis (typically, to allow plotting of reflectivity curves versus band structure, as opposed to sample bias voltage). The development of this method, as laid out in this section, has appeared, in part, in published form in Ref. 4.

The measurement is performed as a function of the sample voltage, V , which is the potential difference between the sample and cathode emitter,

$$eV = \mu_c - \mu_s, \quad (2.5)$$

where the Fermi energies of the sample and cathode emitter are denoted by μ_s and μ_c , respectively, as defined in Eqs. (2.1). As discussed in Section 2.1.3, the sample bias is also related to the vacuum levels E_{vac}^s , E_{vac}^c and work functions W_s , W_c of the sample and cathode as follows,

$$eV = \Delta W + E_{\text{vac}}^c - E_{\text{vac}}^s, \quad (2.6)$$

where the difference in work functions is defined as $\Delta W \equiv W_s - W_c$, as in Eq. (2.4).

For a relatively ideal spectrum such as in Fig. 2.4(a), we see, as a function of decreasing voltage, a sharp onset (near 1.5 V) at which the reflectivity rises to unity. This signifies the transition to *mirror mode* of the LEEM;[35, 40] as pictured in Fig. 2.5(a), for sample voltage lower than this onset, the incident electrons do not have sufficient energy to reach the surface. Rather, they are reflected by the electric field (typically 10^4 V/mm) that extends out from the surface to the objective lens of the electron optics. This field is shown schematically in the context of the illumination column of a LEEM in Fig. 2.3, whereas a close-up of the field near the sample surface is represented in Fig. 2.5. For a sample voltage equal to the onset voltage, the vacuum levels of the sample and cathode emitter are aligned. Denoting the onset voltage by V_0 , we have

$$eV_0 = \Delta W. \quad (2.7)$$

For voltages greater than the onset, all electrons are reflected from the sample surface or absorbed into the sample, as pictured in Fig. 2.5(b).

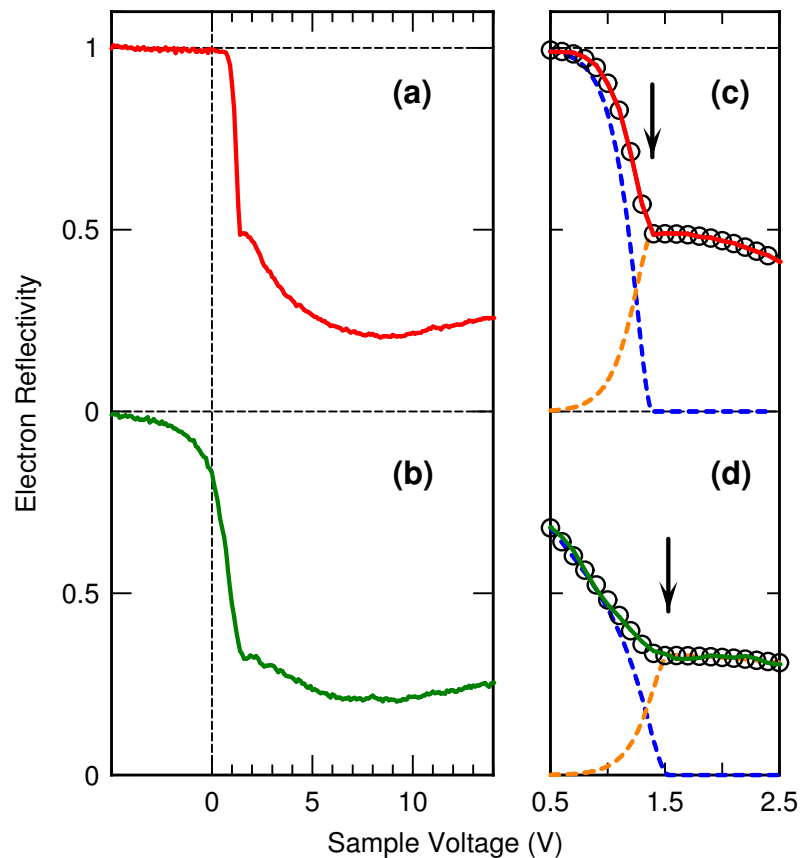


Figure 2.4: (a) and (b) Typical reflectivity spectra (in this case, from graphene on Cu grown by atmospheric pressure chemical vapor deposition), with (a) displaying a sharp transition to unit reflectivity (near 1.5 V sample voltage) and (b) showing a more gradual transition. (c) and (d) Expanded views of the transition regions from panels (a) and (b), respectively. Black circles show a fit function, with the arrows indicating the onset voltages derived from the fit. The two components of the fits, for each spectrum, are indicated by the dotted lines.

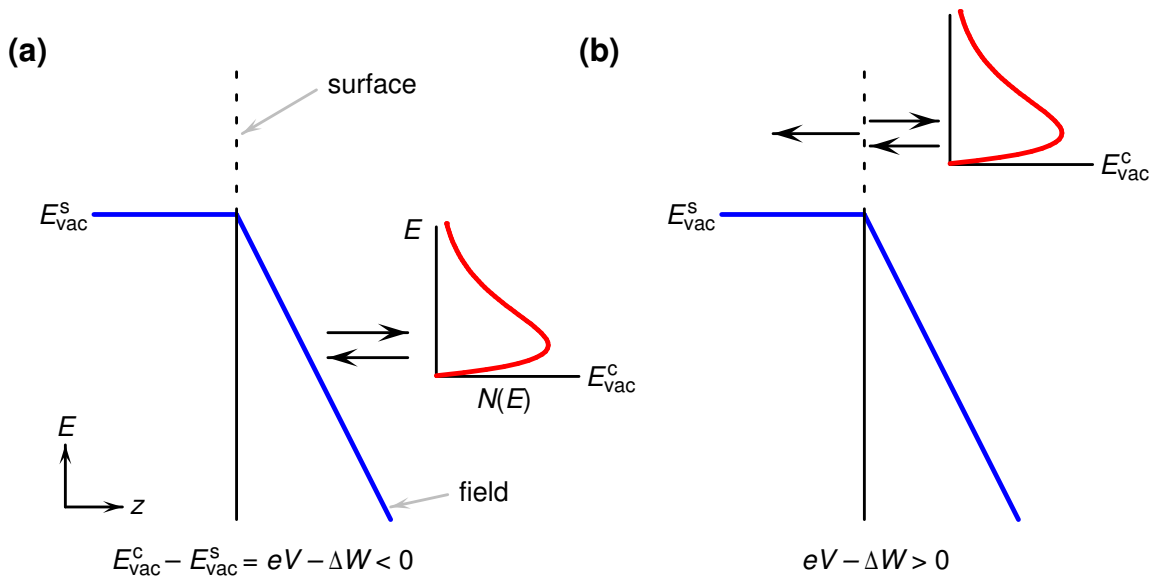


Figure 2.5: (a) and (b) Schematic energy diagrams of the distribution $N(E)$ of electrons incident on the surface of a sample in LEEM. In (a), the electrons are reflected by the field extending out from the surface, whereas in (b) the electrons have sufficient energy to reach the surface, where they are partially reflected and partially absorbed. For a schematic showing these potentials in the context of the LEEM, see Fig. 2.3.

A convenient way to plot reflectivity spectra is in terms of the energy of a sample state, as probed by the incident electrons. Electrons emitted from the thermionic emitter have a well-known energy distribution,

$$N(\varepsilon) = \frac{\varepsilon}{\sigma_c^2} \exp\left(-\frac{\varepsilon}{\sigma_c}\right), \quad (2.8)$$

with $\sigma_c = kT_c$ where k is Boltzmann's constant, T_c is the temperature of the cathode emitter, and with ε being the electron energy relative to E_{vac}^c . [41] This distribution is peaked at $\varepsilon = \sigma_c$, so that the incident electrons have peak energy of $\sigma_c + E_{\text{vac}}^c$. Due to this shift in the peak energy from E_{vac}^c , the largest contribution to measured reflectivity is similarly shifted. This energy corresponds to the energy of a probed sample state, which we denote by E . Therefore, for plotting the spectra on an energy scale we employ

$$E - E_{\text{vac}}^s = \sigma_c + E_{\text{vac}}^c - E_{\text{vac}}^s \quad (2.9a)$$

$$= \sigma_c + e(V - V_0), \quad (2.9b)$$

where the second line follows from the first by using Eqs. (2.6) and (2.7). In our labeling of the spectral plots, we drop the superscript ‘‘s’’ from E_{vac}^s , with $E - E_{\text{vac}}$ understood to refer to the energy of a sample state relative to the vacuum level of the sample.

To obtain values for σ_c and V_0 from the data, we employ a least-squares fitting procedure. Consider the situation of Fig. 2.5(a) with $V < V_0$; some electrons of the incident distribution will be reflected by the field. The number of those mirror-reflected electrons is given by

$$f_m(V) = \int_0^{\varepsilon_1} \left[\frac{\varepsilon}{\sigma_c^2} \exp\left(-\frac{\varepsilon}{\sigma_c}\right) \right] d\varepsilon, \quad (2.10)$$

where the upper limit of integration is $\varepsilon_1 = E_{\text{vac}}^s - E_{\text{vac}}^c = -e(V - V_0)$. Evaluating the integral, we find

$$f_m(V) = 1 - \left(1 - \frac{V - V_0}{\sigma}\right) \exp\left(\frac{V - V_0}{\sigma}\right), \quad (2.11)$$

where $\sigma \equiv \sigma_c/e$. The number of electrons reflected from the sample is given by

$$f_s(V) = [1 - f_m(V)] r(E), \quad (2.12)$$

where $r(E)$ is the reflectivity of the electrons at an energy given by Eq. (2.9b). No considering the situation of Fig. 2.5(b) with $V > V_0$, we have no electrons being reflected by the field, $f_m(V) = 0$, and the number of electrons being reflected from the sample surface is given simply by $f_s(V) = r(E)$. For fitting the observed spectra, we do not assume that the data are necessarily normalized to unit reflectivity (for

example, at large, negative sample voltages). Hence, for the field-reflected electrons, we employ a fit function of the form

$$g_m(V) = \begin{cases} a_0 [1 - (1 - \frac{V-V_0}{\sigma}) \exp(\frac{V-V_0}{\sigma})], & V \leq V_0 \\ 0, & V > V_0, \end{cases} \quad (2.13)$$

where a_0 is a fit parameter. For the electrons reflected from the sample surface, we must assume some form for the reflectivity $r(E)$. We expand this function as a second-degree polynomial about an energy (relative to E_{vac}^s) of $e(V - V_0)$, yielding the fit function

$$g_s(V) = \begin{cases} G_s (1 - \frac{V-V_0}{\sigma}) \exp(\frac{V-V_0}{\sigma}), & V \leq V_0 \\ G_s, & V > V_0, \end{cases} \quad (2.14)$$

where $G_s = b_0 + b_1(V - V_0) + b_2(V - V_0)^2$, with b_0 , b_1 , and b_2 all being fit parameters.

Thus, for a relatively ideal spectrum such as that of Fig. 2.4(a), we fit the data to $g_m(V) + g_s(V)$, with the fit employing the four linear parameters a_0 , b_0 , b_1 , and b_2 along with the two nonlinear parameters V_0 and σ . The result is shown in Fig. 2.4(c), with best-fit values of $V_0 = 1.385 \pm 0.004$ V and $\sigma = 0.121 \pm 0.003$ V. We obtain a very good fit for a voltage window extending over ± 1 V or more on either side of the onset, for spectra such as this, yielding a relative work function $\Delta W = eV_0$ with less than 10 meV uncertainty. The value obtained here for the width of the electron distribution, 0.12 eV, is typical for a data set such as shown in Fig. 2.4, acquired with relatively low current through the electron emitter. For higher currents (for example, for images of smaller surface areas), we obtain widths as large as 0.3 eV or more due to the higher temperature of the cathode emitter element (full-width at half-maximum is $2.45 \times$ greater[41]), consistent with prior reports.[42] We repeat this fitting procedure for a few relatively ideal spectra on the surface, determining a best-fit value for σ that characterizes all the spectra. This value is then kept fixed for all subsequent fits to that data set.

Now let us consider a spectrum such as that of Fig. 2.4(b), which displays a much slower approach of the reflectivity to unity value as the voltage is decreased. This type of behavior is a signature of *lateral fields* on the surface of the sample, arising from a work function difference between neighboring surface areas.[40] Electrons will, in general, be deflected from an area of high work function toward an area of lower work function at Fermi equilibrium, as shown in Fig. 2.6(a). Hence, in the LEEM images of areas near a transition from high to low work function, the high work function area will appear dark and the low work function area will appear light, as in Fig. 2.7(a). This is clearly evident in mirror-mode imaging of surfaces, that is, for sample voltages $V < V_0$, although it may also affect the image contrast at voltages $V > V_0$. Of course, we would still like to quantitatively obtain the onset voltage values in such cases from some sort of fit.

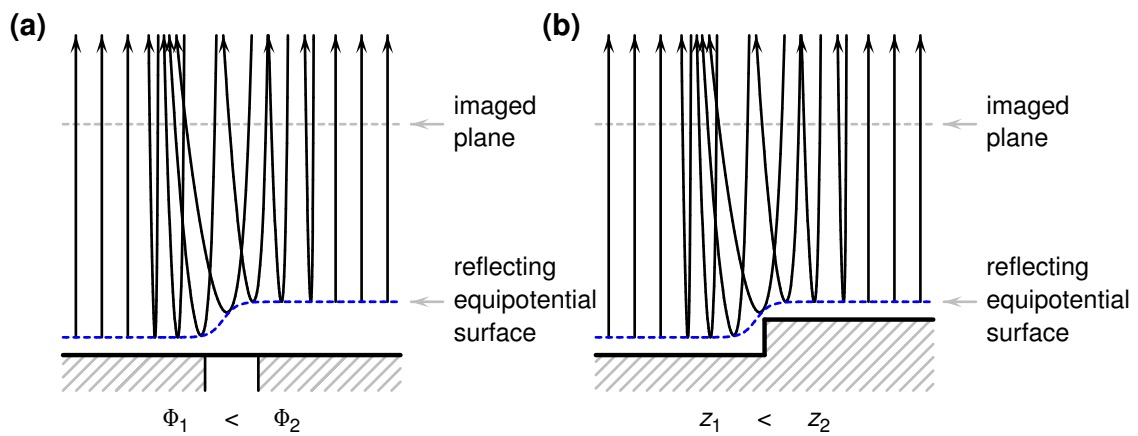


Figure 2.6: Schematic diagram of deflected beam trajectories near a sample surface as observed in mirror-mode, near the onset voltage V_0 . (a) Beam deflection due to lateral fields at the junction of two regions with differing work function. The resulting variation in electrostatic conditions near the surface deflect incident and reflected electrons toward the region of lower work function. (b) Beam deflection due to a step height change on a sample surface. In this case, lateral fields are caused by curvature of the equipotential surface as it conforms to the sharp difference in topography.

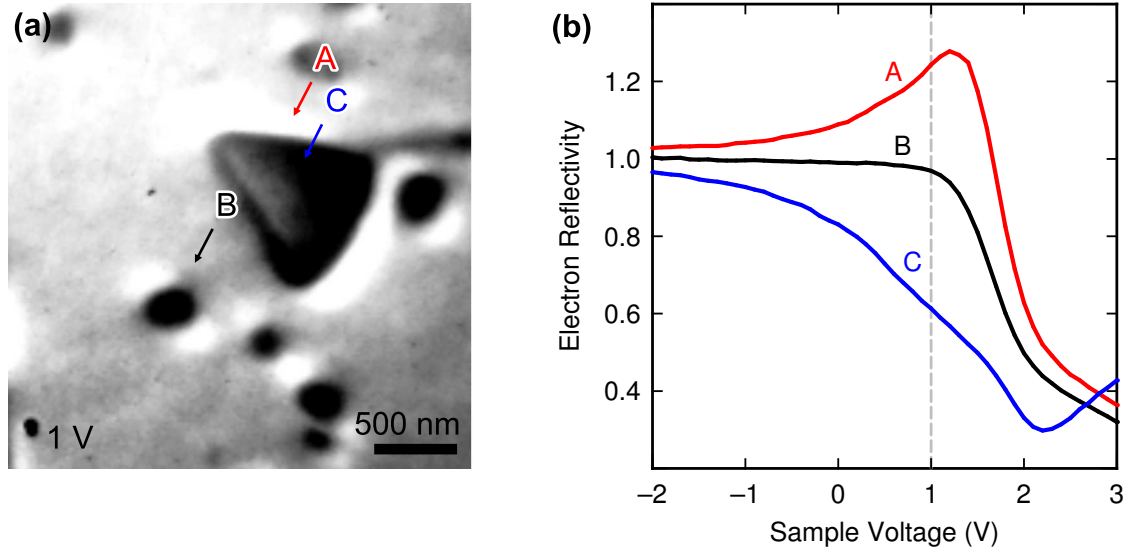


Figure 2.7: (a) Image distortion due to beam deflection by surface potential variations in mirror-mode (close to V_0 sample bias). In this case, the higher work function of a WSe₂ island (dark triangle) compared to the surrounding graphene (light background area) causes electrons to be deflected toward the graphene, as in Fig. 2.6(a). This effect manifests as neighboring bright and dark regions at the junction of the two regions of differing work function. (b) Reflectivity signature of beam deflection. Reflected intensity approaches unity for large negative voltages, with a flat approach in typical curves, as in curve B, taken from a region without potential variation. On the low-work function side of a junction (curve A), reflectivity is augmented over unity by the extra electrons deflected from the other side of the junction (curve C). These effects are strongest near the mirror-mode onset. Vertical dashed line indicates sample bias used to capture image in panel (a).

Let us consider the situation when electrons are swept away from the spectrum, as for the spectrum of Fig. 2.4(b), focusing on the field-reflected electrons in particular. We hypothesize some sort of “loss function” for those missing electrons, which multiplies the $g_m(V)$ reflectivity that occurs in the absence of the loss. Experimentally, it appears that the loss is most pronounced for voltages near the onset voltage (which is not surprising since it is for these voltages that the electrons approach nearest to the surface), and its influence decreases gradually as the voltage (energy) is reduced. We assume a form for the loss function as a second-degree polynomial, expanded in terms of $(V - V_0)$. Thus, for these relatively non-ideal spectra, we fit the mirror-mode electrons to a function of the form

$$\tilde{g}_m(V) = \begin{cases} G_m \left[1 - \left(1 - \frac{V-V_0}{\sigma} \right) \exp\left(\frac{V-V_0}{\sigma}\right) \right], & V \leq V_0 \\ G_m, & V > V_0, \end{cases} \quad (2.15)$$

where $G_m = a_0 + a_1(V - V_0) + a_2(V - V_0)^2$, with a_0 , a_1 , and a_2 all being fit parameters. For the case of sample-reflected electrons, we can still use Eq. (2.14) for the fit, since the effect of the lateral fields on the surface in modifying the reflectivity will simply be absorbed in a redefinition of the b_0 , b_1 , and b_2 parameters. Figure 2.4(d) shows an example of this sort of fit to a non-ideal spectrum, utilizing $\tilde{g}_m(V) + g_s(V)$, and with the fit now having six linear parameters a_0 , a_1 , a_2 , b_0 , b_1 , and b_2 , along with one nonlinear parameter, V_0 . Again, good fits are obtained over a voltage range of ± 1 V or more on either side of the onset. The best-fit value for $\Delta W - eV_0$ obtained in this case is 1.53 ± 0.05 eV. The error is about $10\times$ larger than for fits of more ideal spectra.

Chapter 3

Thickness characterization of tungsten diselenide using electron reflectivity oscillations

In this work, low-energy electron microscopy is employed to probe structural as well as electronic information in few-layer WSe₂ on epitaxial graphene on SiC. The emergence of unoccupied states in the WSe₂-graphene heterostructures are studied using spectroscopic low-energy electron reflectivity. Reflectivity minima corresponding to specific WSe₂ states that are localized between the monolayers of each vertical heterostructure are shown to reveal the number of layers for each point on the surface. A theory for the origin of these states is developed and utilized to explain the experimentally observed features in the WSe₂ electron reflectivity. This method allows for unambiguous counting of WSe₂ layers, and furthermore may be applied to other 2D transition metal dichalcogenide materials. The work described in this chapter appears in published form in Ref. 6.

3.1 Introduction

Low-energy electron microscopy (LEEM) is a powerful characterization tool for two-dimensional (2D) materials, since it provides both structural and electronic information, the latter dealing with unoccupied states above the surface vacuum level. In such a system, a beam of electrons with energies between 0 and 20 eV is reflected from a sample surface at normal incidence. The short penetration and escape depth of incident and reflected electrons with such low energy enables sensitivity to only the top-few atomic layers. For these reasons, LEEM is highly suited to studies of 2D materials and 2D heterostructures. There have been numerous LEEM studies of semimetallic graphene[43–48] and insulating hexagonal boron nitride,[4, 49] but the expanding class of 2D semiconductors remains to be investigated in detail.[5, 50, 51]

Here, we study atomically thin films of WSe₂, a semiconducting transition metal

dichalcogenide (TMD), that are prepared by metal-organic chemical vapor deposition (MOCVD) on epitaxial graphene on SiC. Epitaxial graphene (EG) provides an atomically-flat substrate for TMD growth and carries away excess charge during LEEM. Low-energy electron diffraction (LEED) patterns taken from the surface indicate that the WSe₂ crystals prepared by this method are crystalline and epitaxially aligned to the underlying graphene. The preference for well-defined rotational alignment with graphene is promising for future electronic applications that require integration of 2D semiconducting and metallic components.

By measuring the reflected intensity of electrons as a function of effective beam energy, it is possible to extract spectroscopic information pertaining to electronic states at each point in the surface. These spectra, called low-energy electron reflectivity (LEER), have been shown to allow unambiguous counting of the number of stacked monolayers of few-layer graphene and subsequent thickness mapping based on automated analysis methods.[43, 48] The layer-counting method relies on the presence of special states which are localized between the atomic layers of graphene, and on strong coupling between those states and the electrons involved in LEEM imaging. Since WSe₂ is another layered material, it is a natural question to ask whether or not similar states exist between the quasi-2D layers of few-layer WSe₂ and can be counted by analyzing electron reflectivity. We show that by carefully considering features in the reflectivity of WSe₂, it is indeed possible to distinguish monolayer WSe₂ on EG from regions with two layers or more.

3.2 Methods

In this study, epitaxial graphene (EG) formed on 6H-SiC is used as a template for synthesis of atomically thin WSe₂ crystals. A 1 cm² piece of diced SiC is etched in a 10 % H₂/Ar mixture at 700 Torr and 1500 °C for 30 minutes to remove surface damage caused by wafer polishing. The SiC is subsequently annealed in a pure Ar environment at 200 Torr and 1620 °C for 10 minutes.[52] During the entire process the SiC substrates are inside a graphite crucible, which reduces the sublimation rate of Si at high temperatures and hence improves the uniformity of graphene morphology. WSe₂ synthesis is carried out on EG substrates with conditions as previously reported by Eichfeld *et al.*,[53] with the W and Se precursors in this growth being W(CO)₆ and H₂Se respectively.

Following WSe₂ growth, samples are transferred to an Elmitec LEEM III for characterization. The principal mode of the LEEM directs a broad, monochromatic beam of electrons at the sample surface at normal incidence. The elastically reflected electrons are filtered to allow only non-diffracted trajectories, and the remaining electrons are refocused into an image of the surface using a series of electron lenses. Images are captured with a voltage bias applied between the sample surface and the electron gun, which determines the effective energy of the incident electrons.

Computations are performed using the Vienna Ab-Initio Simulation Package (VASP),

employing the projector-augmented wave method and the Perdew-Burke-Ernzerhof generalized gradient approximation (PBE-GGA) to the exchange-correlation functional,[54–57] with a plane-wave energy cutoff of 500 eV. Low-energy electron reflectivity (LEER) spectra of free-standing slabs of multilayer 2D materials are computed using a method described previously.[48, 58] Inelastic effects are included in the computations,[59] employing an imaginary part of the potential, V_i . Following the detailed analysis of Krasovskii and co-workers,[60–62] in our prior work we employed the phenomenological expression $V_i = 0.4 \text{ eV} + 0.06E$ where E is the energy of a state relative to the vacuum level.[59] These values for V_i were found to give a reasonably good correspondence between experiment and theory, emphasizing experiments with energies of 0–10 eV. In the present work we are especially concerned with reflectivity behavior in the upper part of this range, near 10 eV (and also including energies up to 15 eV). We find that use of the $V_i = 0.4 \text{ eV} + 0.06E$ expression produces reflectivities that are too low (i.e. too much inelastic attenuation) near 10 eV. We therefore use a different expression, $V_i = 0.4 \text{ eV} + 0.03E$, for all spectra computed here (i.e. the value of the slope parameter is reduced by a factor of 2). Comparing theoretical spectra obtained with these two expressions for V_i , we feel that this new expression might slightly underestimate inelastic effects near 10 eV (and above) in typical 2D materials that we examine. Nevertheless, this new expression provides a better means of examining such features in the theory since, again, attenuation near 10 eV is significantly reduced.

3.3 Experimental results

Figure 3.1 shows LEEM images of the sample surface captured at a few sample voltages, showing the strong dependence of image contrast on sample bias. This dependence can be quantified by recording the reflected intensity of electrons as a function of sample voltage for each pixel, in a series of images captured in a voltage sweep. The resulting low-energy electron reflectivity (LEER) curves are extracted from the images for specific points or regions of interest to provide spectroscopic information about the surface. For example, the reflectivity curves shown in Fig. 3.1(e) were extracted from the labeled points in panel 3.1(d). The relevant features in such spectra are reflectivity minima, which correspond to energies of electronic surface states that couple with incident electrons, causing transmission into the sample and thus reduced reflectivity at those energies.

The broad minimum in spectrum C of Fig. 3.1(e) near 4.0 V is associated with a state that exists between monolayer graphene and the carbon-rich surface reconstruction of the SiC below,[43, 48] and therefore indicates the presence of monolayer graphene in that region of the image. Curve D, which has two minima surrounding 4.0 V and a local maximum in the middle, is similarly characteristic of bilayer graphene. Curves A and B, however, originate from WSe₂ regions, and yield a more complex set of reflectivity features with slight variations between the two curves. The

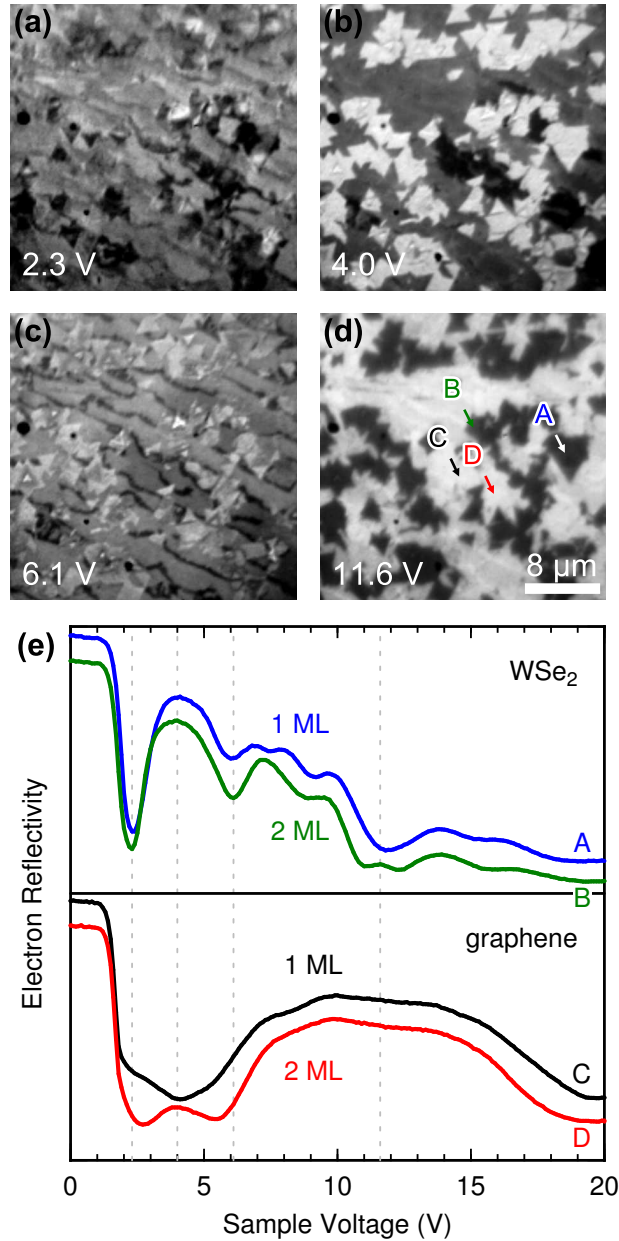


Figure 3.1: (a)–(d) LEEM images showing a single region of few-layer WSe_2 crystals on epitaxial graphene on SiC for a few sample bias voltages, as indicated. (e) Reflected intensity of electrons extracted from the four labeled points in (d) as a function of sample voltage for two thicknesses of graphene and WSe_2 . Curves are shifted vertically for clarity and purposes of illustration. Vertical dashed lines indicate the voltages used to capture the images in (a)–(d).

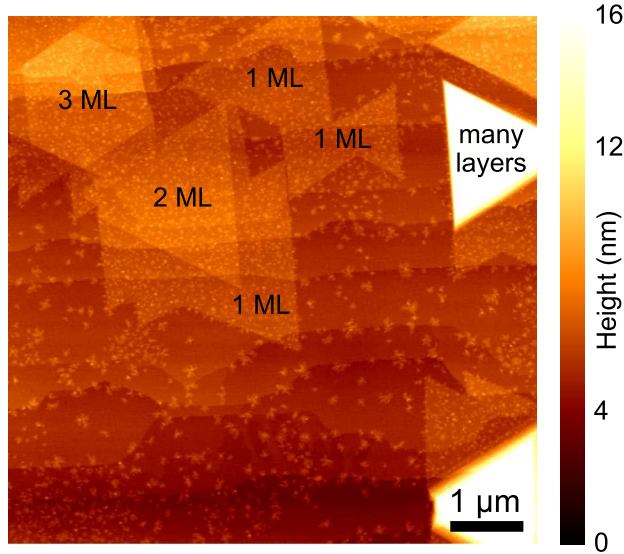


Figure 3.2: Atomic force microscope image of surface height, showing monolayer (1 ML), bilayer (2 ML), and trilayer (3 ML) regions of WSe_2 on the epitaxial graphene surface.

largest differences in these two curves are the shape of the minimum near 6.1 V and the presence of a single- or double-minimum around 11.6 V.

Atomic force microscope (AFM) scans of the surface reveal that the majority of the WSe_2 crystals are monolayer (1 ML) and bilayer (2 ML), with a few instances of thicker island growth (Fig. 3.2). The height change between the top of a monolayer crystal and the EG surface is approximately 0.65 nm, similar to other samples prepared by the same method.[53, 63] Electron reflectivity from one of these monolayer WSe_2 crystals is shown in curve A of Fig. 3.3(b), with a local minimum at 10 eV. We ascribe the occurrence of this minimum to a specific state which exists in monolayer WSe_2 , and will be discussed in Section 3.4. Bilayer WSe_2 triangles are also observed in LEEM as well as AFM. The reflectivity from one of these triangles, shown in curve B of Fig. 3.3(b), exhibits two reflectivity minima surrounding a local maximum at 10 eV. In this case the two minima can be understood to result from a combination of two nearly-degenerate monolayer- WSe_2 states, and thus this double-minimum is a signature of bilayer WSe_2 .

To classify the crystals within the imaged region in Fig. 3.4(a), we create a colored map based on the relevant reflectivity features. Colors are assigned based on the total reflectivity of specific energy windows for each point on the surface, and the result is a false-color spectroscopic image, weighted by the spectral components within each energy window, as in Fig. 3.3(a). From this spectroscopic image, we clearly see the few-layer graphene areas, which primarily have states within the band gap region of the WSe_2 spectrum (between 1.5 and 3.5 eV, with high reflectivity) and appear

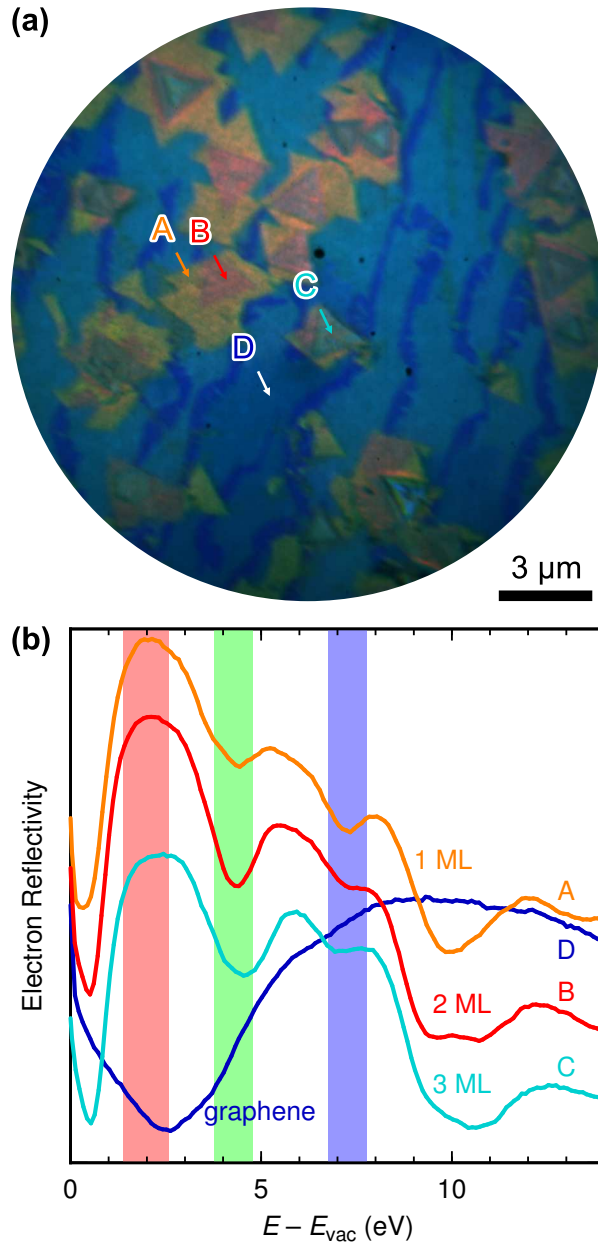


Figure 3.3: (a) False-color spectroscopic image of MOCVD-grown WSe_2 on epitaxial graphene, for the region shown in Fig. 3.4, with colors assigned to the reflected intensity of electrons for specified energy windows. (b) Reflected intensity of electrons from labeled locations in (a). Curves are shifted vertically for clarity and plotted versus energy, rather than sample voltage, for comparison with theory. Colored energy ranges indicate those used to generate the spectroscopic image.

blue due to the assignment of red and green channels to energies in this regime. Two WSe₂ reflectivity minima near 4 and 7 eV, which evolve with the number of layers, are assigned to green and blue channels, respectively, causing color variations in the map based on the number of layers. For example, in this color scheme, monolayer WSe₂ appears yellow-hued, while bilayers appear rose-hued, and trilayers appear turquoise (for a few small triangles in the center of pyramidal structures). The map generated by this colorization scheme is further evidence of the reproducibility of reflectivity analysis for determining WSe₂ thickness.

In another mode of LEEM operation, diffraction patterns are acquired, allowing direct analysis of the surface structure. We insert a small aperture to reduce the illuminated area of the surface and collect a diffraction pattern for the local region, so-called selected area diffraction or μ LEED. Diffraction patterns from the encircled regions in Fig. 3.4(a) show distinct 6-fold diffraction spots from the graphene (larger wavevector) and WSe₂ (smaller wavevector), with six additional satellite spots surrounding the central, specular (00)-spot, originating from the $6\sqrt{3} \times 6\sqrt{3}$ -R30° surface reconstruction, also known as the buffer layer of EG-SiC.[44] The WSe₂ spots form small groups azimuthally-centered on the diffraction pattern of the underlying graphene. From the angular spread of these points, we find that the WSe₂ preferentially forms rotationally aligned with the graphene lattice, within $\pm 2.3^\circ$, for the given growth conditions. Interestingly, the macroscopic alignment of the triangular crystal edges seen in the LEEM images are primarily oriented within 60° of one another. This suggests that a specific edge termination is preferred by this growth method, however, from LEEM it is not clear which type.

3.4 Theoretical results

As first discussed by Hibino *et al.*[43, 64] and extensively analyzed in our prior work,[48, 58, 59, 65] the occurrence of minima in low-energy electron reflectivity spectra is associated with interlayer states that occur between the 2D planes of van der Waals (vdW) bonded materials. Such interlayer states arise from the image-potential states that exist on either side of a single 2D layer,[66, 67] i.e. a monolayer (ML) of carbon for the case of graphene or ML-WSe₂ for the case of bulk WSe₂. When 2D MLs are brought together to form a vdW-bonded bulk material, the image-potential states of the respective layers combine to form a band of interlayer states.[66] The image-potential states themselves have energies some 10's of meV below the vacuum level, but when they combine to form the interlayer states then those states end up with energies typically in the range of 0–8 eV above the vacuum level, at least for the case of graphene.¹ As discussed in prior work, the interlayer states are free-electron

¹ The interlayer band that we are discussing here, occurring in the 0–8 eV range, is actually the lowest band of a pair of two bands. The upper band has energy of 14–22 eV, at least for the case of graphene.[58] The combinations of image-potential states that form the bands are symmetric

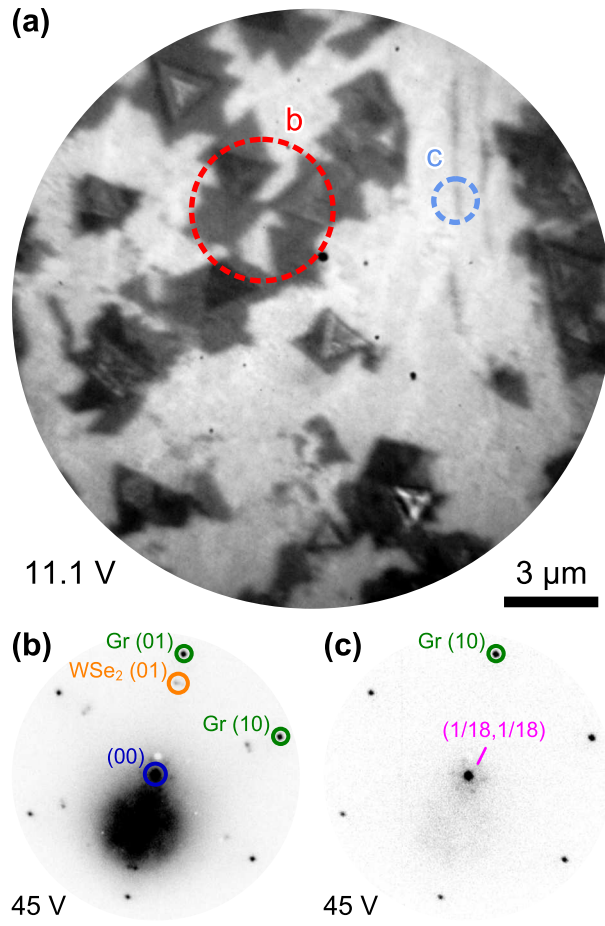


Figure 3.4: (a) LEEM image of WSe_2 -EG-SiC, showing $2\ \mu\text{m}$ triangular WSe_2 islands on a bright background of few-layer epitaxial graphene. (b) Selected-area diffraction from the circular region labeled “b” in the LEEM image shows six dark, outer spots from the graphene lattice, with six additional groups of spots associated with the WSe_2 islands at a smaller wavevector. Surrounding the non-diffracted (00) spot, there are six satellite spots associated with the $6\sqrt{3} \times 6\sqrt{3}$ -R30° reconstruction of the SiC. (c) Diffraction from the bare graphene region labeled “c” in the LEEM image shows only the six outer diffraction spots and the $6\sqrt{3}$ structure also found in (b), labeled by (1/18, 1/18).

like,[66] in the sense that in the spaces between the 2D sheets (the interlayer spaces), these states have character similar to that of plane wave with wavevector magnitude of $\kappa_0 = \sqrt{2m(E - E_{\text{vac}})/\hbar}$ where $E - E_{\text{vac}}$ is the energy of the state relative to the vacuum level. The wavefunctions of the interlayer states tend to be concentrated in the interlayer spaces; they have a local maximum at a location midway between neighboring 2D planes.

Given a band structure of a vdW-bonded bulk material, we analyze it to determine the amount of plane-wave character within the interlayer space that each state exhibits. With the z -direction being along the c -axis of the material, it is only necessary to consider states with wavevector components $(k_x, k_y) = (0, 0)$ and $k_z \equiv k$. We define an overlap between a wave function of the material and a plane wave according to:

$$\sigma_{\pm} = \frac{\sqrt{Ac}}{z_2 - z_1} \int_{z_1}^{z_2} \phi_{\nu, \pm k}^{0,0}(z) \exp(i\kappa_0 z) dz, \text{ and} \quad (3.1a)$$

$$\sigma \equiv (|\sigma_+|^2 + |\sigma_-|^2)^{1/2}, \quad (3.1b)$$

where A is the area of the lateral unit cell of the material and c is the c -axis periodicity, z_1 and z_2 define the interlayer space over which the overlap is computed, and $\phi_{\nu, \pm k}^{0,0}(z)$ is the $(G_x, G_y) = (0, 0)$ Fourier coefficient of the wave function (equal to the wave function averaged over the lateral unit cell). We note that this form is the same as the one we previously introduced in connection with our low-energy reflectivity analysis, although in that prior analysis it was evaluated for the case of far-separated 2D layers in a periodic supercell,² whereas in the present case it is evaluated between 2 ML of a bulk material. All of the evaluations of σ presented below are performed by computing the overlap over a 2-Å-wide space centered at the midpoint of the interlayer space, with $z_2 - z_1 = 2 \text{ \AA}$.

Before examining the band structure for the material of interest, WSe₂, it is instructive to first review the situation for simpler materials such as graphite and hexagonal boron nitride (h-BN). Figure 3.5(a) shows the band structure of graphite, for $(k_x, k_y) = (0, 0)$. We use symbol sizes for the plotting which, for each state, are given by some minimum symbol size plus an amount that is proportional to the computed value of σ for that state. Hence, bands that have significant plane-wave character (i.e. significant interlayer character) are revealed by the relatively large symbol sizes. As is well known from prior work,[43, 48] in graphite there is only a single band with interlayer character, the one labeled “interlayer” at the top of Fig. 3.5. Importantly, this interlayer band has its origin not in terms of any atomic orbitals in

(antisymmetric) for the lower (upper) band, relative to a location midway between the sheets of 2D material.

² An additional distinction between the form introduced in Eq. (3.1) and that used previously in Ref. 48 is that the former refers to states with $\pm k_z$ whereas the latter referred to even and odd states formed by linear combinations of the $\pm k_z$ states. However, the resulting values for σ are identical for both cases.

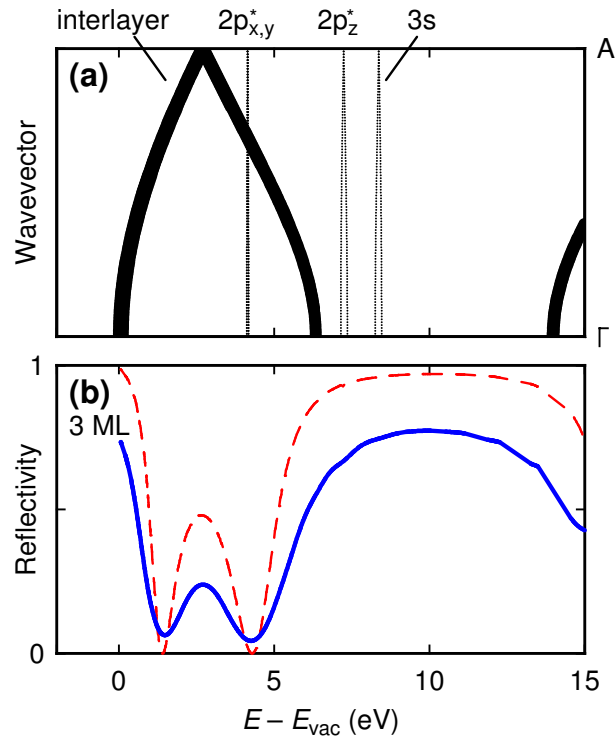


Figure 3.5: (a) Band structure of graphite, with wavevector varying from Γ to A. Symbol sizes, beyond a minimum size, are proportional to the value of σ (Eq. (3.1)) for each state. (b) Computed LEER spectra of 3 ML free-standing graphene, with (blue solid line) and without (red dashed line) inelastic effects. Energies are relative to the vacuum level of the 3-ML slab.

the material, but rather, it arises from plane waves existing in the interlayer spaces as already discussed above. All the other bands that are seen in Fig. 3.5(a), however, *can* be related to specific combinations of atomic orbitals, as labeled at the top of the figure.

The situation for graphite is especially simple since there is zero coupling (zero overlap) between the interlayer band and the overlapping and/or nearby bands. Specifically, we consider the bands labeled $2p_{x,y}^*$, $2p_z^*$, and $3s$ in Fig. 3.5(a). These labels are meant to be approximate ones, indicative of the character of the states in the bands. This character is readily apparent from several types of analysis; examination of the spherical symmetry of the states relative to atomic locations, tight-binding modeling of the bands and comparison to first-principles results, examination of the dependence of the bands on interlayer separation, and individual inspection of specific wavefunctions of the states.[68] We find that all of the states of these three bands are orthogonal to the states in the interlayer band. This orthogonality arises for the states of the $2p_{x,y}^*$ band due to its composition in terms of in-plane p -orbitals, whereas it arises for the $2p_z^*$ and $3s$ bands because the wave functions of states in those bands have opposite sign on neighboring C atoms of the graphene lattice.

Figure 3.5(b) shows the low-energy electron reflectivity (LEER) spectrum that arises from free-standing multilayer graphene containing 3 graphene layers, computed without and with inelastic effects. As is well known from prior work, one reflectivity minimum occurs for every interlayer space in the structure. For example, for 3 graphene layers there are 2 interlayer spaces and hence 2 reflectivity minima.[48] The theoretical spectrum including inelastic effects shown in Fig. 3.5(b) is in good agreement with experiment.[43, 59] Importantly, since there is no overlap between the states of the interlayer band and those of overlapping and/or nearby bands, those bands make no contribution to the resulting LEER spectra.

In Fig. 3.6 we display results for h-BN. Figure 3.6(a) shows the bulk h-BN band structure, again with symbol sizes computed in accordance with the σ values. The inequivalence between the B and N atoms of h-BN produces large changes to the band structure compared to that of graphene, but nevertheless, a single interlayer band together with a few nearby bands can be identified in Fig. 3.6(a). One of these nearby bands has $2p_{x,y}^*$ character; as for graphene, the states of this band are orthogonal to states of the interlayer band. However, in contrast to the situation for graphene, the other two nearby bands, which for h-BN have mixed $2p_z^*$ and $3s$ character, are not orthogonal to the interlayer band. This difference occurs simply due to the inequivalence of B and N atoms, which destroys the precise orthogonality described above for graphite. Hence, these two nearby bands acquire some degree of plane-wave (interlayer) character.

Resulting LEER spectra for 3 MLs of free-standing h-BN, with and without inelastic effects, are displayed in Fig. 3.6(b). In the absence of inelastic effects, the coupling of the interlayer character with two of the nearby bands leads to reflectivity minima associated with each of the bands. All of the three bands with interlayer character

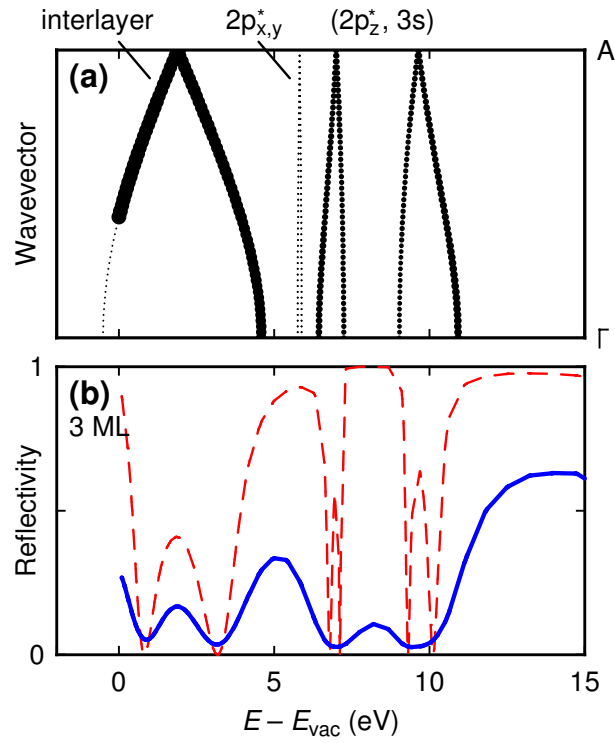


Figure 3.6: (a) Band structure of bulk h-BN, with wavevector varying from Γ to A. Symbol sizes, beyond a minimum size, are proportional to the value of σ (Eq. (3.1)) for each state. (b) Computed LEER spectra of 3 ML of free-standing h-BN, with (blue solid line) and without (red dashed line) inelastic effects. Energies are relative to the vacuum level of the 3-ML slab.

in Fig. 3.6(b) display two reflectivity minima each, arising from the two interlayer spaces. However, when inelastic effects are included, a large amount of broadening occurs in the spectra, particularly for the two bands with mixed $2p_z^*$ and $3s$ character. The reflectivity maximum that occurs at 8.2 eV between these two bands for the computation neglecting inelastic effects is greatly diminished in size, to become a weak, local maximum which separates the two minima (at 7.0 and 9.5 eV) of this band. No discrete thickness oscillations are observed in connection with these minima; the oscillations found in the absence of inelastic effects are eliminated when the inelastic effects are included. Experimentally, a broad reflectivity minimum centered at about 8.2 eV above the vacuum level has indeed been observed in h-BN LEER spectra,[4, 49] and two minima (or a minimum and a shoulder) are seen within that broad minimum. As mentioned in Section 3.2, for the computation of Fig. 3.6(b) we are employing values for the energy-dependent imaginary part of the potential (which governs inelastic effects) which are somewhat reduced from our typical values, in order to emphasize these features in the 7–11 eV range (which are especially relevant for the WSe₂ spectra).

Figure 3.7 displays the bulk bands for WSe₂. There are many more bands than for graphene or h-BN, arising from the multiplicity of s , p , and d states of the W and Se atoms. Low-lying bands of interest in Fig. 3.7(a) are numbered 1–7 (with band 7 being the relatively wide band with significant plane-wave character centered at 10 eV). From a decomposition of the states into their s , $p_{x,y}$, p_z , d_{z^2} , $d_{xz,yz}$, and d_{xy,x^2-y^2} character (not shown), we find that bands 4 and 6, each of which is doubly degenerate, have purely $d_{xz,yz}$ character, with nodal planes parallel to the xz and yz planes. Hence, these bands have no plane-wave character, and they make no contribution to the reflectivity. Of the remaining bands, band 3 is seen to have the most plane-wave character, bands 1 and 7 have substantial plane-wave character, and bands 2 and 5 have a small amount of plane-wave character.

Reflectivity for free-standing slabs of 1, 2, and 3 MLs of WSe₂ are shown in Fig. 3.7(b)–(d), respectively. The spectra that do not include inelastic effects reveal thickness oscillations for most of the bands, with the number of minima given by either the number of layers (n) or the number of interlayer spaces ($n - 1$), depending on the particular band. However, with inelastic effects included all of these oscillations disappear, and the respective minima associated with each band appear just as a single, broad minimum. These broad minima occur at approximately the same energies (relative to the vacuum level) as the features observed in the experimental spectra of Section 3.3. For comparison, these experimental curves are reproduced in Fig. 3.7 as well.

Concerning the small reflectivity features discussed in Section 3.3 at 4 and 10 eV which we associate with differing thicknesses of the WSe₂, these are more difficult to discern in the theoretical spectra. However, comparing the 1 ML and 2 ML spectra, we see a significant difference in their behavior near 10 eV; the former shows a single, distinct minimum at 9.7 eV, whereas the latter displays a broad minimum extending

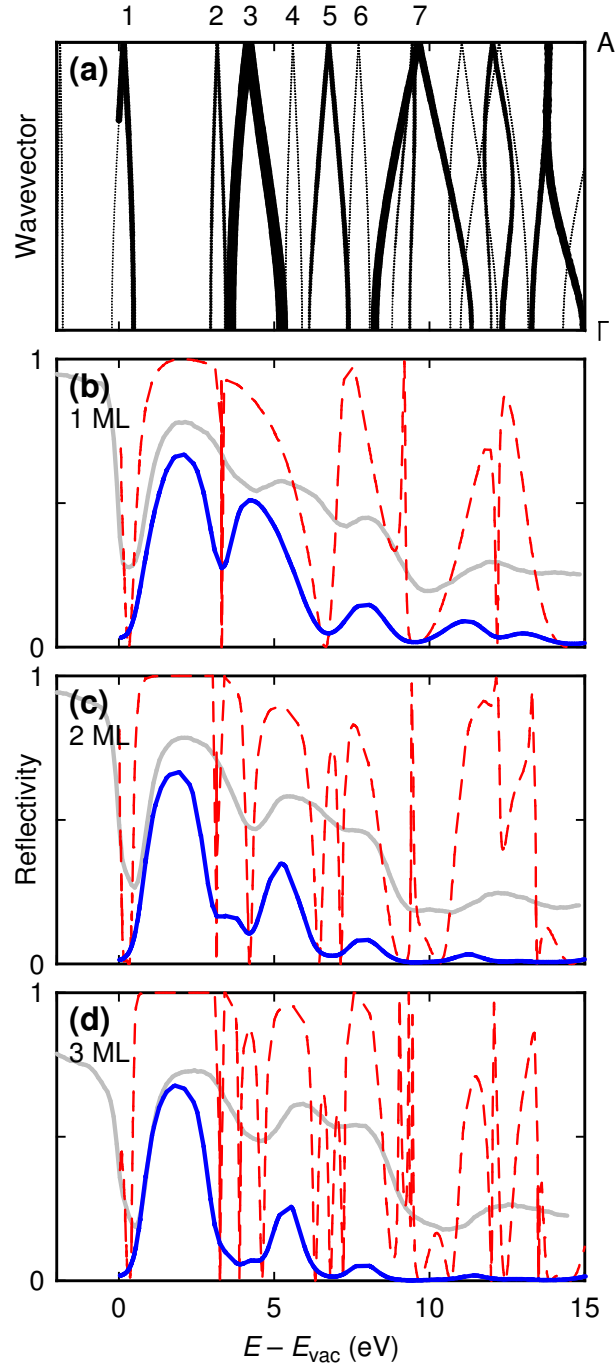


Figure 3.7: (a) Band structure of bulk WSe₂, with wavevector varying from Γ to A. Symbol sizes, beyond a minimum size, are proportional to the value of σ (Eq. (3.1)) for each state. (b)–(d) Computed LEER spectra of 1, 2, and 3 ML of free-standing WSe₂ as indicated, with (blue solid lines) and without (red dashed lines) inelastic effects. Experimental curves (gray solid lines) from Fig. 3.3 are superimposed for comparison. Energies are relative to the vacuum level of the respective slabs.

over about 9.0–10.5 eV (with two minima in the elastic-only computation seen at either end of this range). For the case of 3 ML of WSe₂, an even broader minimum near 10 eV is seen. Of course, an important distinction between the theoretical spectra of Fig. 3.7 and the experimental spectra of Section 3.3 is that the former are for free-standing WSe₂ MLs, whereas the latter are for WSe₂ on top of an epitaxial graphene substrate. This difference is further discussed in Section 3.5.

3.5 Discussion

Computation of reflectivity spectra for WSe₂ on few-layer graphene is quite complex due to the poor epitaxial fit of the materials and the large size of the supercell required. Nevertheless, predictions for the evolution of reflectivity minima for free-standing slabs of 1-, 2-, and 3-ML WSe₂ appear to be sufficient for interpretation of the experimentally-measured reflectivity from WSe₂-EG-SiC, despite neglecting the effect of the substrate. In comparing the measured results from Section 3.3 to the computed reflectivity in Section 3.4, it is important to note that the experimental curves are measured versus sample voltage V_S , and not energy above the vacuum level $E - E_{\text{vac}}$ directly. Due to the work function difference ΔW between the electron gun filament of the LEEM and the WSe₂ on the sample surface, the experimental curves are shifted approximately 2.2 V (depending on location) toward higher voltage. Using a quantitative method for determining the local vacuum level outlined in Ref. 4, the experimental reflectivity curves are shifted by ΔW in order to plot the spectra versus $E - E_{\text{vac}} = eV_S - \Delta W + \sigma_c$, including a small energy shift $\sigma_c \approx 0.1$ eV to account for the peak energy of thermionic emission from the gun cathode. With this method in place, it is possible to plot the experimental reflectivity curves together with the computed ones in Fig. 3.7.

It is a known result that high-energy bands computed with PBE-GGA (as discussed in Section 3.2) are generally lower energy than real bands. As such, the subsequent computed reflectivity curves are typically shifted 0.5 to 1 eV lower along the energy axis compared to experiment.[68] With this in consideration, we conclude that there is reasonable agreement between the computed and experimental minima near 0, 7, and 10 eV.

Critically, the minimum near 10 eV in the 1 ML computed reflectivity curve shown in Fig. 3.7(b) evolves into a broad, flat minimum in the 2 ML case, as in 3.7(c). The flat minimum occurs in the computed reflectivity due to the combined effect of two nearby states, one of which has lower energy and produces a deeper minimum in the 2-ML case than in the 1-ML case. The elastic-only computed curves show this behavior most clearly, although the overall effect becomes complicated for more than 2 ML. A similar flattening of the minimum near 10 eV is clearly observed in the 1- and 2-ML experimental curves (gray solid lines in Fig. 3.7(b) and 3.7(c)), although in the measured curves there are two distinct minima, whereas our best fit shows no clear oscillations using the inelastic model implemented here. In any case, beyond

2 ML it may be difficult to resolve additional minima in measured reflectivity due to inelastic effects.

The states which form band 3 have strong interlayer character and subsequently vary as the number of interlayer spaces, $n - 1$. In addition, states from nearby band 2 couple and broaden the resulting reflectivity minimum such that for 1 ML of WSe_2 , there is a narrow minimum near 3.3 eV, whereas for 2 ML the minimum is deeper and shifted to higher energy. This effect is also observed in the experimental reflectivity outlined in Section 3.3 and therefore provides another signature for discriminating between 1- and 2-ML WSe_2 . For a greater number of layers, the computed minimum near 4 eV is expected to broaden and deepen further, but will not develop countable oscillations like those near 10 eV. It is the wide dispersion of band 7 that allows the states in the few-layer limit to be resolved, as was the case for the interlayer bands in graphene and h-BN. Thus, for bands with small dispersion the variation with number of layers is predicted to be less pronounced.

Finally, although the computations considered here do not include the graphene or SiC below the WSe_2 layers, it is reasonable to posit that interactions between the WSe_2 and graphene might have an effect on the reflectivity. In particular, minima associated with interlayer states in few-layer graphene occupy an energy window from 0–7 eV, as in Fig. 3.5. The band gap in the WSe_2 spectrum between bands 1 and 2 reflects most electrons with energy in that range, and therefore prevents coupling to graphene interlayer states below the WSe_2 , however, there may still be coupling between the upper WSe_2 band gap edge and 7 eV. Whether or not evidence of this can be observed remains an open question.

3.6 Conclusions

We have shown that low-energy electron reflectivity measurements of WSe_2 -EG-SiC yield distinct spectroscopic signatures for WSe_2 and graphene regions. By correlating the observed LEEM images with AFM scans of the surface, we have identified monolayer and bilayer crystals of WSe_2 and labeled the reflectivity accordingly. Using a first-principles method of calculating electron reflectivity curves from free-standing slabs of few-layer WSe_2 , we have assigned the observed features in 1- and 2-ML- WSe_2 reflectivity to specific states with strong plane-wave character. We argued that enumeration of these states provides a clear evolution of reflectivity minima as layer number increases, and that this evolution allows discrimination between 1- and 2-ML- WSe_2 from the reflectivity alone. Furthermore, by numerically analyzing the spectral features from a LEEM imaging dataset it is possible to generate a colorized map of WSe_2 layer thickness with high fidelity across the image. This method paves a path forward for quickly determining few-layer WSe_2 film thickness with atomic resolution, and may be applicable to other TMD materials as well. The results and analyses presented here provide critical insight for future studies of layered heterostructures including WSe_2 and graphene, as well as LEEM studies of other 2D materials.

Chapter 4

Tunneling transport between transition metal dichalcogenides

Over the last five years, many groups have worked to fabricate vertical tunneling devices using graphene, h-BN, and 2D semiconducting transition metal dichalcogenides (TMDs). Within our own collaboration, we sought to make devices exhibiting both resonant tunneling (between like bands in either electrode) as well as steep switching (between unlike bands). Presently, there have been several successful reports of negative differential resistance (NDR) in a number of devices,[63, 69, 70] beyond the graphene ones discussed in Chapters 7 and 8. An even greater number of studies have resulted in 2D devices with a similar vertical geometry that display neither NDR nor steep switching based on vertical tunneling.[71–74]

Needless to say, many groups sought to measure tunneling transport in devices strikingly similar to the ones we proposed and were considering for experimental studies. In this fast-moving context, we decided to pursue two paths in parallel:

1. Take advantage of the great progress in *grown* vertical 2D heterostructures (largely within our own collaboration) by investigating these structures with low-energy electron microscopy, a highly-suited tool for studying 2D materials with which we have a great deal of expertise (as introduced in Chapter 3).
2. Build up a capability to assemble arbitrarily complex vertical heterostructures of *exfoliated* 2D materials, with the goal of making high-quality devices with high throughput (see Chapter 9).

In fact, this work proved to be successful in both approaches, but it is the effort toward objective 1 that will be introduced in this chapter.

4.1 Introduction

Epitaxial growth methods, metal-organic chemical vapor deposition (MOCVD), molecular beam epitaxy (MBE), and powder vaporization (PV), which proceed in a layer-

by-layer manner, provide many advantages for the synthesis of 2D materials. For vertical heterostructures in particular, layer-by-layer growth allows direct control of the constituent materials in a serial fashion, and typically these techniques can be scaled to large lateral dimensions in a way that is not possible with exfoliated materials. Hence, a great deal of effort has gone into adapting epitaxial growth methods to form atomic layers of MoS₂, MoSe₂, WSe₂, h-BN, and others on graphene,[50, 52, 68, 75, 76] as well as graphene on h-BN.[77, 78] Graphene itself has been formed in large-area films using CVD on metal foils with varying degrees of quality.[79–83] Graphene with a high degree of epitaxial registration and uniformity has been demonstrated by sublimation of Si from the (0001)-surface of SiC, forming *epitaxial graphene* (EG).[11, 46, 84, 85] With these techniques available, it was possible to begin developing processes for a wide range of layered heterostructures and vertical tunneling devices.

From an interpretation standpoint, the most ideal vertical tunneling structures would include an h-BN tunneling barrier, but experimentally it is easier and thus reasonable to begin with stacking TMD layers without an explicit barrier material. As such, the first reports of NDR observed in TMD–TMD vertical tunneling structures did not possess a well-defined barrier, with the hope that the top and bottom electrode layers would only weakly couple, thus forming an effective *van der Waals* barrier between the layers. One of these early heterostructures was fabricated by Roy et al. using exfoliated few-layer WSe₂ on MoS₂, and the measured NDR characteristic was attributed by the authors to be due to Esaki tunneling (that is, not due to resonant momentum-conserving tunneling).[69] Not long after, our collaborators Yan et al. reported NDR between vertically-stacked SnSe₂ and black phosphorus, both of which were composed of many layers (50 nm to 100 nm each), also due to Esaki tunneling.[70]

In another work, our close collaborators Lin et al. observed NDR between monolayers of WSe₂ and MoSe₂ grown on EG, as well as between MoS₂ and WSe₂ on EG in separate structures.[63] In both cases, Lin et al. argued that the resonant tunneling was occurring between like bands, and hence did not result from an Esaki mechanism. In this latter work, however, Lin et al. did not fabricate true devices in the traditional sense, with patterned contacts and well-defined device boundaries, but rather used conducting-AFM (CAFM) to measure current from the tip through selected vertical heterostructures into the underlying graphene. This allowed high throughput electrical characterization, but simultaneously provided some ambiguity in the interpretation of the transport results. To offer insight in this regard, we turned to low-energy electron microscopy (LEEM), another high-throughput technique that would allow us to investigate the structural and electronic properties of these materials without the complications of device patterning. To begin this investigation, we focused on simple heterostructures involving a single TMD formed on graphene, which also showed interesting vertical transport with CAFM,[5, 50, 53] and would serve as a baseline for studies of more complex structures.

For the work involved in the following sections, Sarah Eichfeld carried out the

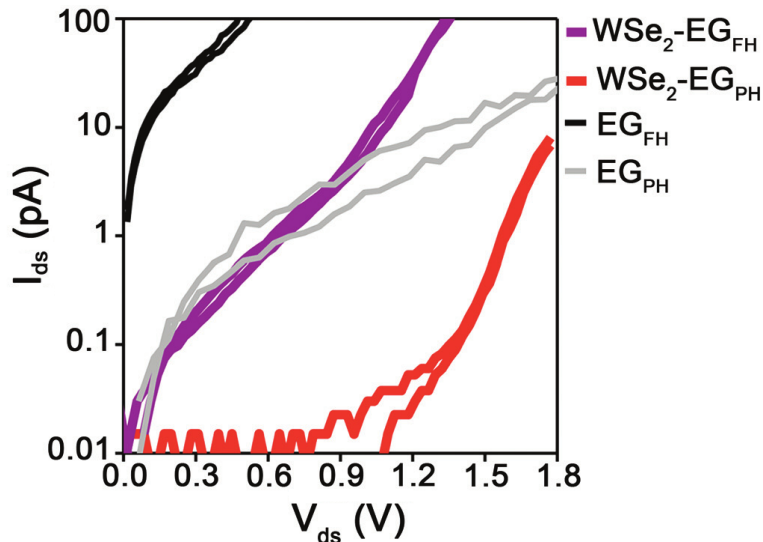


Figure 4.1: Electrical characterization of WSe_2 grown on epitaxial graphene using conducting-AFM (CAFM). The CAFM tip is positioned on a WSe_2 island and current is measured through the WSe_2 into the graphene below, as a function of voltage. Current–voltage characteristics are shown for two substrate types: (i) fully hydrogenated epitaxial graphene (EG_{FH}) and (ii) partially hydrogenated epitaxial graphene (EG_{PH}), with current being highly resistive in the latter cases. Currents are shown for locations on WSe_2 as well as on bare graphene.

growth and sample preparation, Yu-Chuan Lin provided conducting-AFM measurements and leadership for the study, I carried out the LEEM measurements, analysis, and extracted to work function differences, Jun Li provided charge transfer computations, Yifan Nie performed DFT calculations to obtain the interface dipole energies, and all contributors provided input in the final assembly of the results, with guidance from Kyeongjae Cho, Randall M. Feenstra, and Joshua A. Robinson. This work appears, in part, as published work in Ref. 5.

4.2 Vertical transport between tungsten diselenide and epitaxial graphene

Beginning with samples involving the growth of a single TMD overlayer formed on epitaxial graphene on SiC (EG), our collaborators Lin et al. [5] observed peculiar bimodal vertical transport from WSe_2 into the graphene below. By placing a CAFM tip coated with PtIr on monolayer islands of WSe_2 and measuring the current as a function of bias between the tip and the underlying graphene, Lin et al. noticed that the resulting current–voltage (I – V) characteristics varied substantially from sample to sample. In some cases, the WSe_2 –EG behaved as a diode, with a large increase in

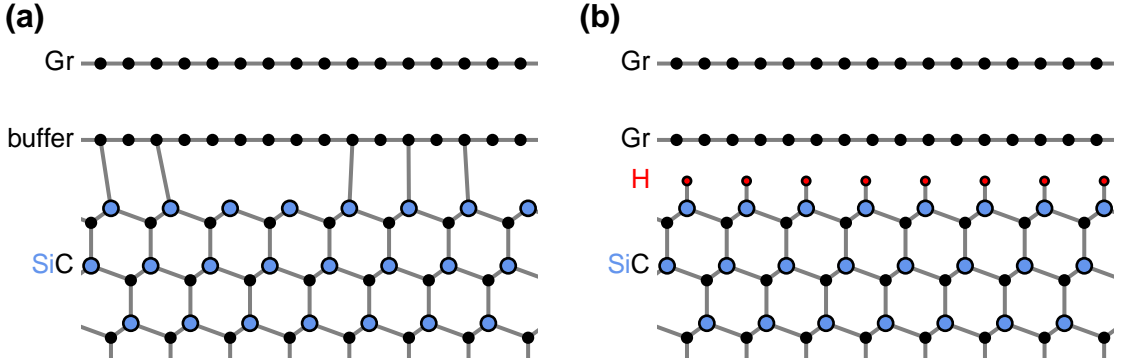


Figure 4.2: (a) Side-view of epitaxial graphene on SiC, which forms a reconstructed carbon *buffer layer* upon Si-sublimation. Partial covalent bonding between the buffer layer and top silicon layer of the SiC prevents graphene-like dispersion in the buffer layer, despite its hexagonal arrangement of C-atoms. (b) Side-view of *quasi-freestanding epitaxial graphene* on SiC, formed by flowing hydrogen at high temperature to passivate the dangling bonds on the SiC surface and thus decouple the buffer layer, which subsequently becomes an additional graphene layer.

current occurring at biases greater than 1 V, whereas in others the measured currents were several orders of magnitude larger, even at zero bias, as in Fig. 4.1. To cast some light on this phenomenon, we consider the growth process used to synthesize these samples.

4.2.1 Sample fabrication

Due to the isostructural nature of graphene with respect to TMD materials, its atomic flatness when formed on SiC, and the advantages of having a semi-metallic underlayer, epitaxial graphene on SiC (EG) was selected as the template for WSe₂ synthesis. Prior to EG formation, the 6H-SiC substrates employed in this study were etched by flowing a 10% H₂/Ar mixture at 700 Torr to remove subsurface damage due to substrate polishing. The EG was then formed via a well-known process[85] involving Si-sublimation from the (0001)-surface of the SiC at 1625 °C in a 200 Torr Ar-environment in a pure graphite heating chamber. Following EG formation, WSe₂ crystals were grown by Eichfeld et al. via metal-organic chemical vapor deposition (MOCVD) using tungsten hexacarbonyl (W(CO)₆) and dimethylselenium ((CH₃)₂Se) precursors for W and Se, as described in Ref. 53. Crucially, in order to prevent carbon impurity incorporation from the precursors,[53] a 100% H₂ carrier gas was used during the WSe₂ formation on the EG. As a side effect of flowing H₂ gas at high temperature, depending on the conditions some hydrogen intercalates between the graphene and SiC.

This too is a well-known effect, utilized in many studies to produce so-called *quasi-freestanding epitaxial graphene* (QFEG) by passivating the Si dangling bonds at the

interface of the graphene and SiC.[46] Structural models of EG and QFEG are shown in Fig. 4.2. To investigate the effect of hydrogen intercalation in our fabrication process, samples were prepared at either 800 °C or 930 °C during the MOCVD stage, and characterized with LEEM.

4.3 LEEM analysis of tungsten diselenide–epitaxial graphene tunneling heterostructures

In order to study the surface and electronic structure of the heterostructure samples, low-energy electron microscopy (LEEM) with electron energies of 0 to 20 eV is employed. In addition, low-energy electron reflectivity (LEER) provides an accurate means of counting the number of graphene layers as well as extracting the work function variation over the surface.[4, 48] The LEEM images of WSe₂–EG from 800 °C WSe₂ growth show triangular islands of WSe₂ with a characteristic size of 1 μm, nucleating preferentially near SiC step edges on the EG surface (Fig. 4.3). The graphene is found predominantly in monolayer + buffer layer form, but small bi- and trilayer graphene crystals are also found on the surface. LEEM analysis indicates that the buffer layer is continuous at the interface of the SiC and EG, suggesting that only a negligible portion of this layer has decoupled during the 800 °C WSe₂ growth.

Low-energy electron reflectivity spectra show of this sample show characteristic oscillations for graphene and WSe₂ for the respective regions of the surface and allow material identification in the LEEM images, as shown in Fig. 4.3(b) for the 800 °C WSe₂ growth.[86] Such LEER curves also permit determination of local work function differences on the surface, as described in Section 2.2. For sufficiently low sample voltages (≈ 2 V) the incident electrons are totally reflected from the sample, near the so-called *mirror-mode* transition (see Section 2.2). The voltage of the mirror-mode transition V_0 corresponds to the work function difference, $\Delta W = eV_0$, between the sample surface and the LEEM electron emitter cathode. Detailed fitting of these transition voltages (energies), locally, for many points on the surface, permits the extraction of variations in work function across the surface.

The average work function difference between the monolayer graphene regions (which covers the majority of the exposed surface) and the electron emitter is found to be $\overline{\Delta W}_{\text{Gr}} \equiv \langle W_{\text{Gr}} - W_{\text{em}} \rangle = 1.87 \pm 0.03$ eV. The values for bi- and trilayer graphene regions are similar, and are summarized in Figs. 4.3(b) and 4.4. The average work function difference between WSe₂ and the emitter is $\overline{\Delta W}_{\text{WSe}_2} \equiv \langle W_{\text{WSe}_2} - W_{\text{em}} \rangle = 2.18 \pm 0.01$ eV. Taking the difference of the monolayer graphene and WSe₂ work function differences, a vacuum level difference of $\delta E_{\text{vac}} \equiv \overline{\Delta W}_{\text{WSe}_2} - \overline{\Delta W}_{\text{Gr}} = 0.31 \pm 0.03$ eV is found. Uncertainties in these values are obtained from a combination of uncertainties in the measurement, analysis, and variations on the sample surface, and are shown in Fig. 4.4. It is important to note that this observed vacuum level (work function) difference is between (i) WSe₂–EG, that is, WSe₂ in contact with

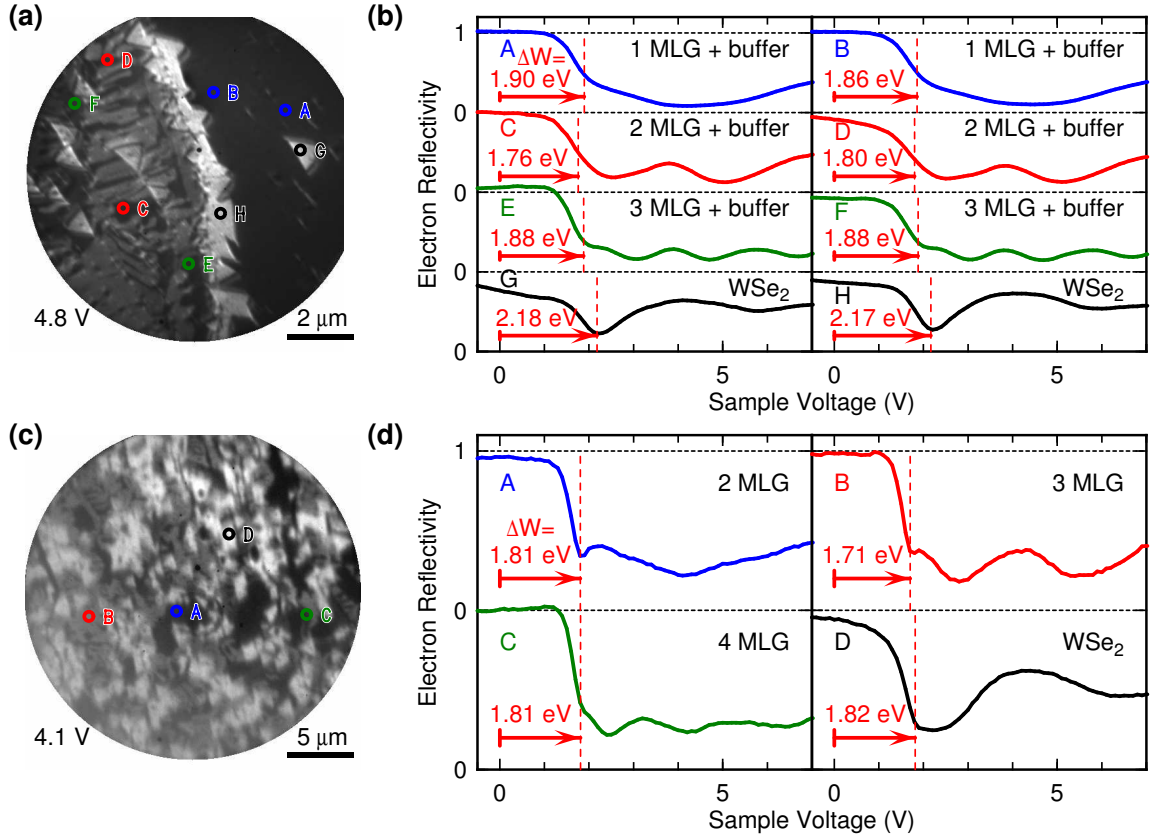


Figure 4.3: (a) Low-energy electron microscopy (LEEM) image of WSe₂ grown on epitaxial graphene on SiC at 800 °C (referenced in text as EG_{PH}), acquired at a sample voltage of 4.8 V. Labeled points indicate locations of reflectivity spectra in (b), which are used to identify the material coverage in the image. Bright triangles are WSe₂ islands, dark regions are monolayer and few-layer graphene on a graphene-like *buffer layer* at the interface of the graphene and the SiC substrate. (b) Reflectivity spectra extracted from labeled locations in (a). ΔW values, to the left of each spectrum, quantify the electrostatic potential variation on the surface due to spatial work function differences, and hence the variation in the vacuum level. (c) LEEM image of WSe₂ grown on epitaxial graphene on SiC at 930 °C (referenced in text at EG_{FH}), acquired at 4.1 V sample bias. Bright regions are WSe₂ crystals, dark regions are few-layer graphene. (d) Reflectivity spectra from labeled points in (c), with small feature characteristic of a released buffer layer (due to passivated SiC dangling bonds) near the onset voltage $V_0 = \Delta W/e$. ΔW values shows much smaller variation between graphene and WSe₂ in this sample compared to the 800 °C growth sample.

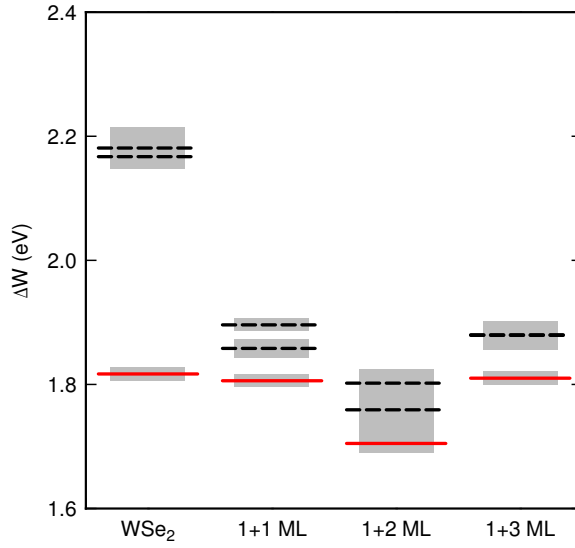


Figure 4.4: Summary of extracted ΔW values from $\text{WSe}_2\text{-EG}_{\text{PH}}$ (dashed) and $\text{WSe}_2\text{-EG}_{\text{FH}}$ (solid) samples. Extracted values from a few locations are shown as horizontal lines for WSe_2 and few-layer graphene. Column labels for few-layer graphene indicate the total number of graphene-like layers, so 1 + 1 ML refers to 2 ML of graphene for the EG_{FH} case and 1 ML plus a buffer layer in the EG_{PH} case. This grouping highlights the similarity in ΔW values depending on the number of layers. Average uncertainties are indicated by gray boxes for each grouping of ΔW values.

underlying graphene (locations G and H in Fig. 4.3(a)), and (ii) bare graphene regions which are next to, but not directly below, WSe₂ (locations A and B in Fig. 4.3(a)). The presence of a vacuum level difference in these regions implies that there must be an interface dipole, and therefore charge transfer, between the WSe₂ and the graphene below. Consistent with this interpretation, it is noted that reflectivity curves measured on the WSe₂ islands from 800 °C growth (Fig. 4.3(b)) display a broad, sloping feature for voltages below the mirror-mode transition. This feature also indicates the presence of charge, or more specifically, electric dipoles on the edges of the triangular crystals which displace the incident and reflected electron beam during measurement, thus reducing the reflected intensity, as discussed in Section 2.2 and shown, for example, in Fig. 2.7(b).

The WSe₂-EG from the 930 °C WSe₂ growth shows similar 1 μm triangle islands on an EG surface in LEEM (Fig. 4.3(c)), however, the sloping features in reflectivity associated with charge accumulations are much smaller than in the sample from the 800 °C WSe₂ growth. In addition, the extracted work function differences between the WSe₂ and the underlying graphene (in contact) in the sample from 930 °C WSe₂ growth are negligible ($\delta E_{\text{vac}} \equiv \overline{\Delta W}_{\text{WSe}_2} - \overline{\Delta W}_{\text{Gr}} = 0.03 \pm 0.03 \text{ eV}$) compared to the sample grown at 800 °C, suggesting limited charge transfer between the layers after growth of WSe₂ (Fig. 4.3(d)). These observations, along with the presence of an additional, small minimum valley in the reflectivity near the mirror-mode transition,[46] are attributed to full hydrogenation of the SiC surface, which passivates bonds between the carbon-rich buffer layer and the SiC, as shown in Fig. 4.2.

This has the effect of releasing the buffer layer and increasing the count of free-standing graphene layers in the hydrogenated regions by 1, creating quasi-freestanding epitaxial graphene (QFEG), which is situated on H-terminated SiC.[87] Based on the evolution of graphene Raman spectra (see Ref. 5) and the LEEM/LEER investigation (Fig. 4.3), we conclude that the WSe₂ growth at high temperatures (>900 °C) leads to hydrogen intercalation and formation of fully hydrogenated epitaxial graphene (EG_{FH}), compared to samples grown at intermediate temperatures (750 °C to 850 °C) which form partially hydrogenated epitaxial graphene (EG_{PH}). Concurrently, the electrical properties of the WSe₂-EG interface appears to have significantly changed, as shown in Fig. 4.1.

4.4 Charge transfer in tungsten diselenide–epitaxial graphene heterostructures

The hydrogenation process is known to have a significant impact on the electrical properties of graphene on SiC. Epitaxial graphene residing on top of the buffer layer reconstruction of graphitized 6H-SiC(0001) is *n*-type doped[85, 87, 88] due to the combination of bulk and interface donor states[89, 90] and has a Fermi energy 0.45 eV above the Dirac point.[90] In contrast, QFEG is known to be *p*-type doped.[46, 90]

This change has been explained by the presence of the spontaneous polarization of the hexagonal 6H-SiC substrate, which lowers the Fermi energy to a position 0.28 eV to 0.30 eV below the Dirac point for complete hydrogenation.[90, 91] This modification in the doping of graphene can thereby influence the electrical transport properties across the WSe₂-graphene interface on SiC. In order to elucidate the effect on transport properties, vertical current versus voltage (I - V) measurements were performed on the 800 °C and 930 °C WSe₂ growth samples (labeled as WSe₂-EG_{PH} and WSe₂-EG_{FH}, respectively) in conducting-AFM (CAFAM).

A CAFM tip with PtIr coating and the graphene serve as the source and drain, respectively. The WSe₂-EG_{PH} diode exhibits an I - V characteristic with current turn-on at a bias greater than 1 V, whereas the WSe₂-EG_{FH} diode turns on near zero bias (Fig. 4.1). To understand this difference, we consider the LEEM measurements of these samples. Analysis of the onset voltages measured in Section 4.3 revealed a work function difference $\delta E_{\text{vac}} = 0.31$ eV between the WSe₂ in contact with monolayer EG_{PH} and the uncovered monolayer EG_{PH} nearby. From the 930 °C growth sample, the work function difference δE_{vac} between the WSe₂ in contact with EG_{FH} and nearby uncovered *bilayer* graphene EG_{FH} (due to release of the buffer layer) is near zero. Each measured work function difference in the layered regions has two components:

1. An intrinsic interface dipole energy resulting from charge redistribution within the graphene and WSe₂ layers, separately.
2. An extrinsic dipole term resulting from charge *transfer* between the layers of WSe₂ and graphene.

The intrinsic interface dipole occurs in response to the difference in work functions in the absence of doping, that is, assuming intrinsic WSe₂ and graphene. This would be equal to the vacuum level difference for undoped WSe₂ and undoped graphene at Fermi equilibrium. The extrinsic dipole is the component that results from excess carriers in both layers transferring between the two in order to achieve Fermi equilibrium. The system as measured in LEEM is of course already in equilibrium, but these statements serve as models for understanding the source of each term.

To quantify these two components, it is necessary to calculate the intrinsic dipole energy and thus extract the portion of the measured δE_{vac} that is due to charge transfer. Density functional theory (DFT) calculations of this intrinsic dipole are performed using the Vienna *ab initio* simulation package (VASP)[55] with the projector-augmented wave (PAW) method.[56] The local density approximation (LDA)[92] is used to describe the exchange-correlation functional with the partial core correction included. For details of this calculation, see the supplementary information of Ref. 5. The resulting value for the intrinsic dipole energy is 0.17 eV, with the dipole field pointing from the graphene toward the WSe₂, that is, the WSe₂ electrostatic potential is 0.17 eV higher than in the graphene below.

Using this intrinsic dipole, along with the measured work function differences, we propose a model in which the WSe₂ has some unintentional *p*-type doping, and

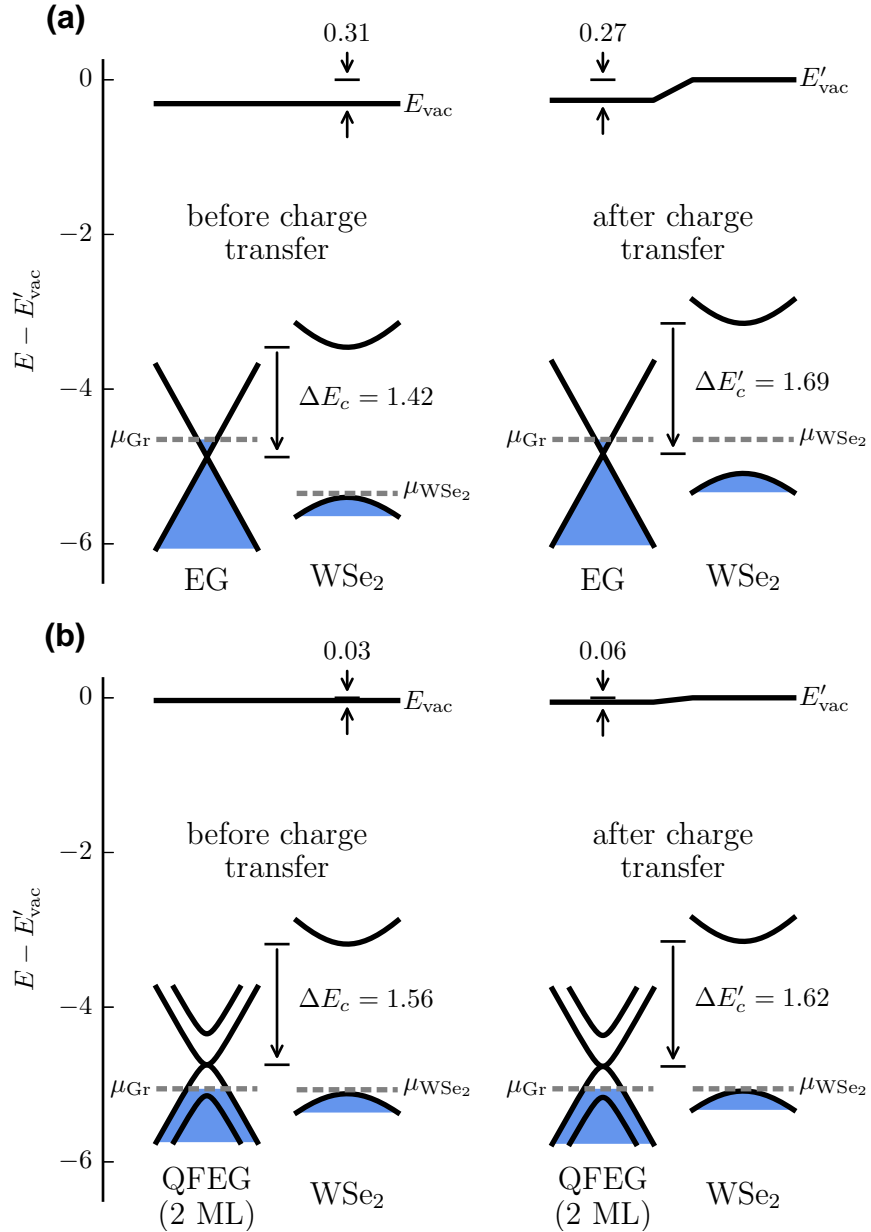


Figure 4.5: Band diagrams illustrating the change in band alignment produced by charge transfer effects at the WSe₂–EG interface. (a) Alignment of monolayer EG_{PH} and WSe₂ bands as modeled before and after charge transfer, and hence equilibrium. Experimentally measured work function difference $\delta E_{\text{vac}} = 0.31$ eV is indicated between the vacuum level of the graphene before charge transfer (left) and the WSe₂ afterward (right). After balancing the electrostatics, the Fermi level ends up in the band gap of the WSe₂. (b) Alignment of bilayer EG_{FH} and WSe₂ bands before and after charge transfer. The experimentally measured work function difference is much smaller, $\delta E_{\text{vac}} = 0.03$ eV, and thus there is little charge transfer between the layers, and therefore the Fermi level ends up near the valence band edge of the WSe₂.

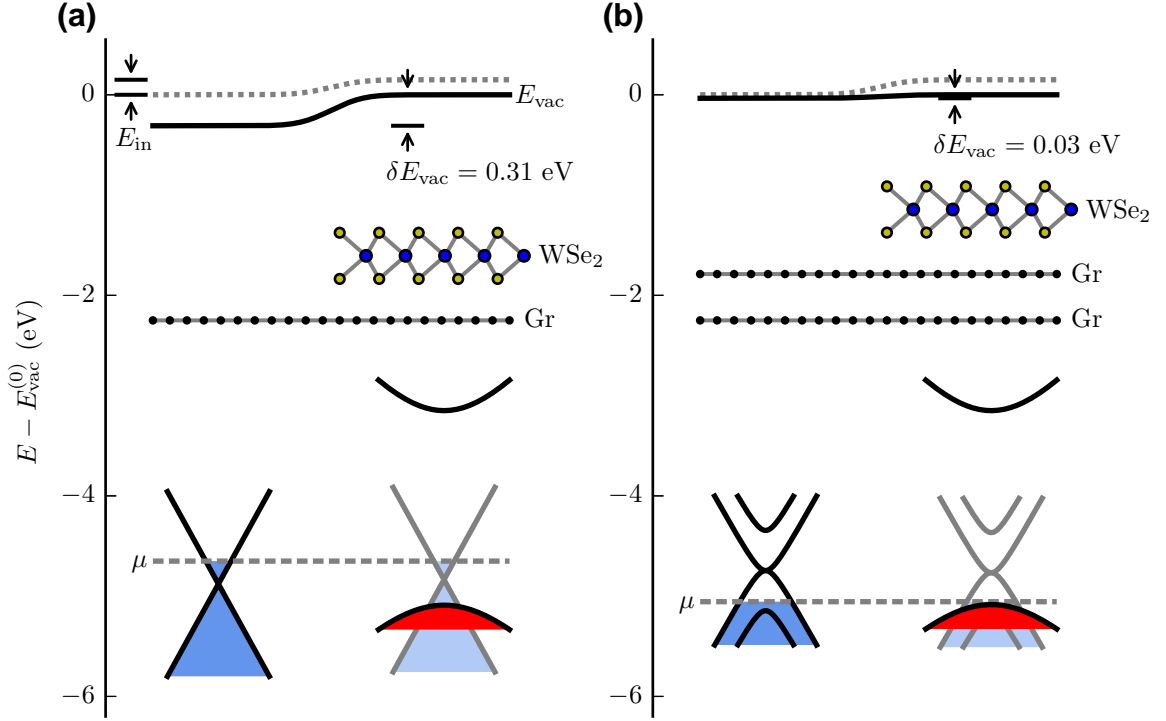


Figure 4.6: (a) Model of equilibrium electrostatic potential and band alignment between regions of EG_{PH} covered by WSe_2 and neighboring bare EG_{PH} regions. Structure model (not on energy scale) illustrates the layer order in covered region. WSe_2 bands ($E(k_{\parallel})$ below each region) are superimposed on graphene bands to highlight the coexistence of the bands in that region (although, in fact, they are separated spatially in z , and in momentum space depending on rotation). Energy scale is referenced to the vacuum level of intrinsic graphene $E_{\text{vac}}^{(0)}$, that is, without doping or the presence of an interface dipole. The raised part of the dotted line therefore indicates the effect of the WSe_2 - EG_{PH} intrinsic interface dipole, E_{in} , on the vacuum level. The total vacuum level change δE_{vac} , including doping and an extrinsic dipole from charge transfer, is illustrated by the solid line. (b) Equivalent model of equilibrium electrostatic potential and band alignment between regions of EG_{FH} covered by WSe_2 and neighboring bare EG_{FH} regions.

subsequent transfer of charge between the EG_{PH} or EG_{FH} and the WSe_2 (combined with the intrinsic dipole) produces the observed variation in work function. With knowledge of the doping density of EG_{PH} and EG_{FH} ($(4 \pm 1) \times 10^{12} \text{ cm}^{-2}$ n -type and $(1.5 \pm 0.2) \times 10^{13} \text{ cm}^{-2}$ p -type, respectively, from previous electrical studies of EG_{PH} and EG_{FH}), [87, 93] and using reported values of electron affinities for monolayer graphene (4.57 eV) and bilayer graphene (4.71 eV), [94] we compute the transfer of charge between the WSe_2 and the EG_{PH} or EG_{FH} . This charge transfer, for a given (unintentional) doping density of the WSe_2 , yields theoretical values for the work function differences; the doping density is determined by matching these differences to experiment. The models for band alignment changes due to charge transfer in the two samples are shown in Fig. 4.5. For details regarding the dependence of the results on the input electron affinities, see the supplementary information of Ref. 5.

For the charge transfer computation, we employ the standard linear band structure around the K and K' points for monolayer graphene in EG_{PH} , and hyperbolic bands near the band extrema for bilayer graphene in EG_{FH} and for WSe_2 around the K and K' points, based on tight-binding models. [95, 96] The method to compute the electrostatics is similar to that discussed in Section 6.3 and described by Li et al. [97]. Fig. 4.6 shows the final result of this calculation graphically, with band diagrams of WSe_2 - EG_{PH} and WSe_2 - EG_{FH} interfaces in regions with partial WSe_2 coverage. Both the intrinsic interface dipole and the extrinsic dipole due to charge transfer are taken into account, and equilibrium is reached when the Fermi levels are aligned. The difference between the vacuum level of WSe_2 (covering a portion of graphene) and neighboring, bare graphene is thus a sum of the intrinsic interface dipole effect and the charge transfer effect (δE_{vac} in Fig. 4.6).

In order to reach equilibrium between the layers of WSe_2 and uncovered graphene and simultaneously match the experimental values for relative work function differences (0.31 eV and 0.03 eV for WSe_2 - EG_{PH} and WSe_2 - EG_{FH} , respectively), we determine that unintentional p -type doping of $1.3 \times 10^{12} \text{ cm}^{-2}$ in the WSe_2 before charge transfer is required. In the model, when the WSe_2 is put in contact with n -type EG_{PH} , electrons transfer from the EG_{PH} to the WSe_2 , leading to nearly complete compensation of the WSe_2 p -type doping and thus negligible carrier density in the WSe_2 . The Fermi level ends up well inside the band gap of the WSe_2 and near the charge neutrality point in the graphene (Figs. 4.5(a) and 4.6(a)). For the case of WSe_2 put into contact with EG_{FH} (which is p -type), a small number of electrons transfer from the WSe_2 into the EG_{FH} layer, making the WSe_2 more p -type, with a carrier density of $2.9 \times 10^{12} \text{ cm}^{-2}$. Critically, the resulting Fermi level of the WSe_2 - EG_{FH} remains near the top of the WSe_2 valence band. In summary, the WSe_2 - EG_{PH} forms a Schottky tunneling barrier (with low conductivity as a result), whereas the WSe_2 - EG_{FH} forms an ohmic contact (much higher conductivity), leading to a $10^3 \times$ increase in current in the latter case (Fig. 4.1). Therefore, the main component of the CAFM current near zero bias for WSe_2 - EG_{PH} is due to *tunneling* from the CAFM tip to the graphene *through* the WSe_2 band gap. On the other hand, for WSe_2 - EG_{FH} ,

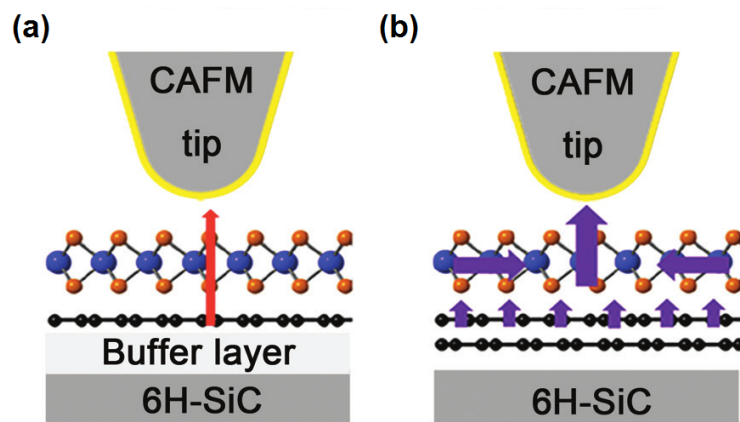


Figure 4.7: Schematic of electrical characterization using conducting-AFM (CAFM). CAFM tip is placed on a WSe₂ crystal and current is measured from the tip to the graphene side of the vertical junction. (a) Current *tunneling* through the WSe₂ due to the Fermi level residing in the band gap of the WSe₂ layer, as in the WSe₂-EG_{PH} sample. (b) Current conducting through semiconducting WSe₂ itself, due to the high carrier density in the WSe₂ and ohmic contact between the WSe₂ and graphene, as in the WSe₂-EG_{FH} sample.

the WSe_2 acts as an electrical short between the CAFM tip and the graphene, and hence ohmic contact (Fig. 4.7).

For validation of our computed charge transfer calculations, we consider the sum of the band gap and electron affinity of the WSe_2 , $\chi_{\text{WSe}_2} + E_g$, which is an output of our model (only the sum enters since the electron density in the WSe_2 conduction band is negligible). In order to match the observed work function variations, we deduce an unintentional doping density in the WSe_2 of $1.3 \times 10^{12} \text{ cm}^{-2}$, and the value of $\chi_{\text{WSe}_2} + E_g$ is determined to be 5.1 eV. This value is consistent with a recently reported electron affinity of ≈ 3.1 eV for WSe_2 using a first-principles GW calculation,[98] together with a band gap of ≈ 2 eV, which is in agreement with several recently reported experimental values.[99, 100]

4.5 Impact of tungsten diselenide–epitaxial graphene characterization

This investigation combining LEEM/LEER, Raman spectroscopy, and electrical characterization revealed that transport across the vertical interface of WSe_2 and graphene is controllable by the doping of the graphene. Moreover, by varying the temperatures for WSe_2 growth on epitaxial graphene in a pure H_2 environment, it is possible to tune the position of the Fermi level in the graphene by partially or fully hydrogenating the EG–SiC interface. This in turn allows the conductivity of the WSe_2 –EG junction to be tuned during the WSe_2 formation process. Band alignment models of two different heterostructures were constructed using the measured work function difference between WSe_2 and epitaxial graphene as extracted from electron reflectivity. Taking into account their intrinsic interface dipoles and charge transfer, the models suggest the presence of a Schottky barrier in WSe_2 –EG_{PH} and ohmic contact in WSe_2 –EG_{FH}, in agreement with measured I – V characteristics. The impact of this work is twofold: (i) we have demonstrated the feasibility of engineering the interface between a 2D semiconductor and graphene to allow desirable transport characteristics, and (ii) we have shown that the nature of such interfaces can be readily probed with a reliable, high-throughput technique based on imaging with LEEM.

Chapter 5

Application of work function extraction method to material characterization

In Section 2.2, I introduced a method for extracting lateral work function differences across the surface of layered two-dimensional heterostructures. The analysis techniques developed in Section 2.2 are applied to reflectivity of CVD-grown WSe_2 crystals formed on epitaxial graphene in Chapter 4, and the resulting work function differences are used to determine the change in band alignment of the WSe_2 and graphene layers due to charge transfer in the following sections. Ultimately, these results are used to explain large differences in WSe_2 -graphene contact resistance based on the preparations methods. The method of relative work function extraction and determination of charge transfer, however, has other possible applications related to material characterization as well. In this chapter, I address the utility of low-energy electron potentiometry, that is, using LEER to extract work function differences and hence the variation in electrostatic potential on surfaces, to examine 2D materials from a materials characterization standpoint.

In this work, samples were prepared by Suresh Vishwanath, led by Grace Xing. Patrick Mende recorded the initial LEEM and LEED data, whereas I performed the spectral analysis, work function extraction, and final assembly of the results. Jun Li provided the computed values from charge balance.

5.1 Defect density in molybdenum diselenide prepared by molecular beam epitaxy

In this study, molybdenum diselenide (MoSe_2) a 2D semiconducting transition metal dichalcogenide (TMD) which is isostructural to WSe_2 , was formed on epitaxial graphene (EG) using molecular beam epitaxy (MBE). Beginning with EG (prepared using

methods described in Section 4.2.1) as a substrate, electron-beam evaporation of a Mo source was used simultaneously with a Knudsen cell supplying Se to deposit a film at a rate of ≈ 0.3 monolayers per minute. Film growth was performed at 400°C , followed by 5 to 10 min of annealing at 400°C with the source shutters closed to remove excess selenium.[86] Samples were transferred *ex situ* to an Elmitec LEEM III for characterization, following several other characterization stages.[86]

LEEM images of the surface show relatively uniform contrast in large portions of the surface (similar to the bright region in Fig. 5.1(a)), with larger variation in contrast in a few regions with swirling morphology (dark region in Fig. 5.1(a)). Selected-area diffraction (μLEED) of the bright and dark regions indicate differing crystallinity between the two regions, as shown in Fig. 1 of Ref. 86. In particular, the dark region is shown to have the expected six-fold diffraction pattern of epitaxial graphene on SiC, indicating that this is a bare region of the surface, not covered by a MoSe_2 film. On the other hand, diffraction from the bright region is diffusely distributed along a ring with a radius (reciprocal wavevector) that corresponds to a hexagonal lattice constant of $3.25 \pm 0.02 \text{ \AA}$, peaked at six spots along the ring.[86] The six-fold symmetry of the ring and the fact that the radius indicates an in-plane lattice constant very close to that of MoSe_2 (3.28 \AA) suggest that the bright region is composed of a polycrystalline MoSe_2 film.

Turning to the spectroscopic characteristics of the surface, reflectivity spectra taken from a few locations are shown in Fig. 5.1(b). Oscillations between 3 and 7 V in curves D, G, H, and J are characteristic of interlayer states in few-layer graphene, and hence allow identification of these regions as graphene, with 1, 2, 3, and 4 layers each, respectively. Curve A is something new, with reflectivity minima that resemble those of WSe_2 , another 2D semiconductor with a similar structure (despite the similarities, this spectrum is distinct from that of WSe_2 , allowing discrimination between the two if required). Due to the agreement between the diffraction pattern from the same bright region with the expected pattern from MoSe_2 , we conclude that this spectrum and other similar ones from this region (curves B and C) are characteristic of MoSe_2 , although the thickness of the film is not clear from reflectivity without further detailed analysis (as is discussed for the case of WSe_2 in Chapter 3).

The mirror-mode onset voltages (discussed in Section 2.2) of the reflectivity curves from different locations on this sample vary in a somewhat large range, an indication of work function differences on the sample surface. Furthermore, there are sloping features in the reflectivity near the onset voltage, especially for curves extracted from locations near the border between the MoSe_2 (bright) and graphene (dark) regions. To investigate these phenomena, we focus on the shape of the reflectivity for low voltages, as shown in Fig. 5.1(c). The detailed features of curves D, E, and F are characteristic of monolayer graphene on a buffer layer of SiC, in agreement with the μLEED analysis of the diffraction pattern from the dark region in the image. Curves A, B, and C, however, are attributed to the MoSe_2 film, taken from the bright region of the image. By carefully fitting the low-voltage part of these spectra

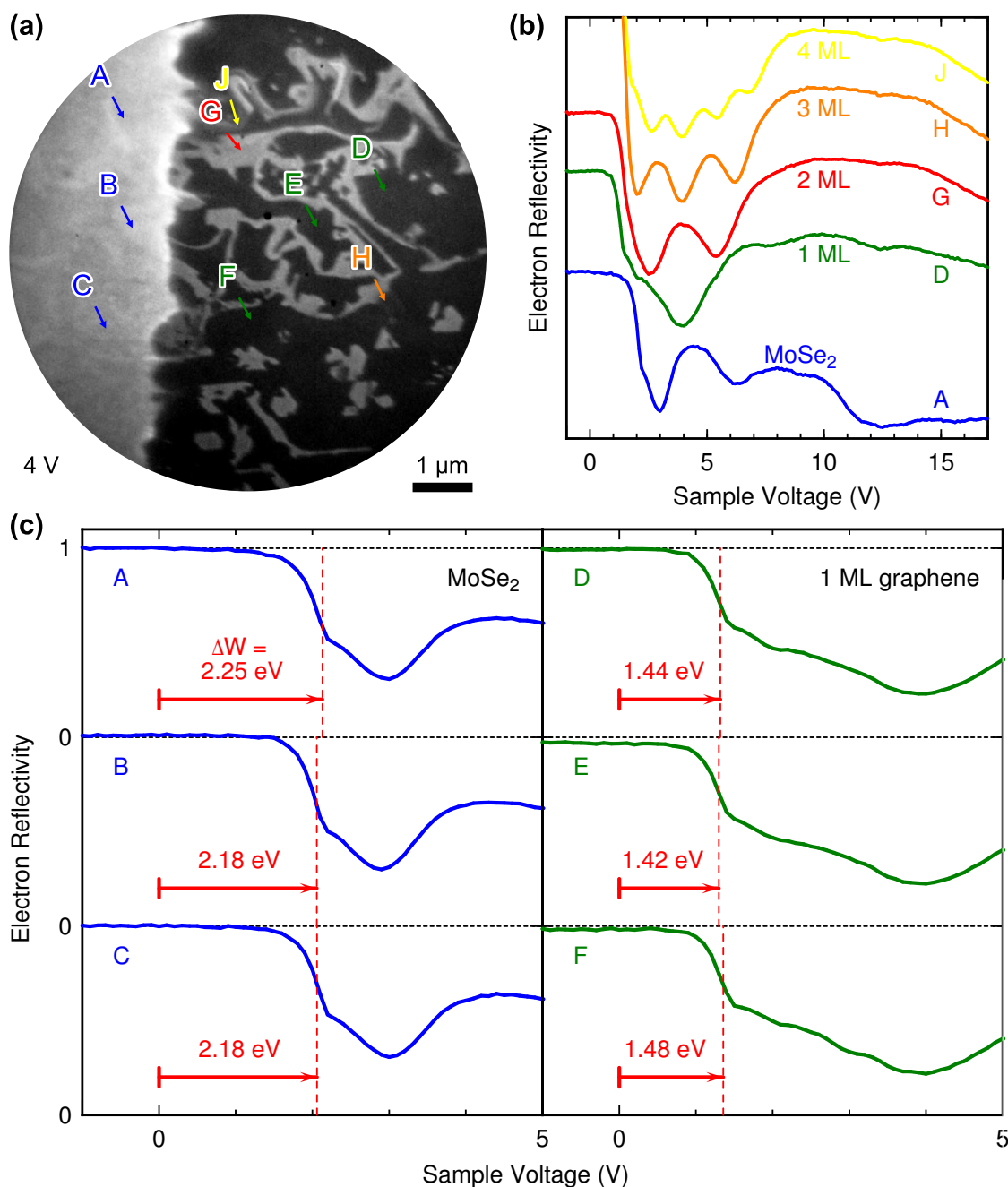


Figure 5.1: (a) Low-energy electron micrograph of MoSe₂ formed on epitaxial graphene by molecular beam epitaxy. (b) Electron reflectivity spectra extracted from the labeled locations in panel a. Each curve is identified and labeled according to the characteristic spectrum of the material. 1 ML, 2 ML, and so on refer to the number of monolayers (ML) of graphene present. (c) Detailed view of reflectivity near the onset voltage of a few graphene and MoSe₂ characteristic curves, with vacuum level differences denoted by ΔW .

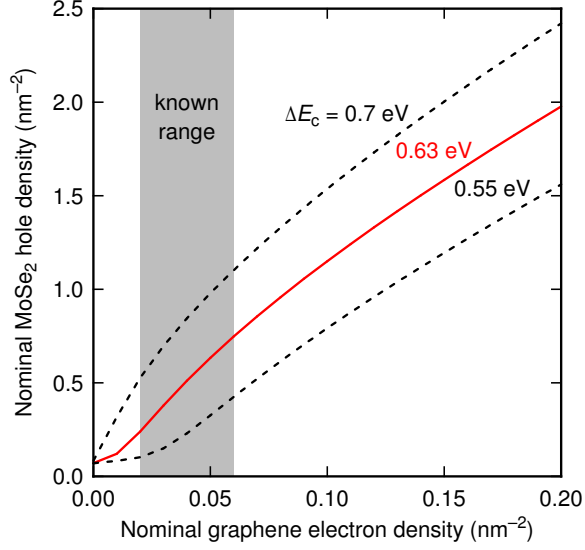


Figure 5.2: Nominal hole density of MoSe₂ (before charge transfer) as a function of nominal electron density in the epitaxial graphene (EG) below; calculated by balancing the electrostatics of MoSe₂-EG in order to produce a 0.75 eV work function difference between the layers, as observed in experiment. The band alignment between MoSe₂-EG is not precisely known, therefore three curves are shown for different conduction band offset values, $\Delta E_c \equiv E_c - E_d$, equal to the difference between the MoSe₂ conduction band edge and the graphene Dirac (charge neutrality) point. The graphene is known to be *n*-type, with a density in the range of $2 \times 10^{12} \text{ cm}^{-2}$ to $6 \times 10^{12} \text{ cm}^{-2}$, and therefore the resulting MoSe₂ hole density will fall along one of the curves in this range.

According to the procedure outlined in Section 2.2, we find that the onset voltages (and thus work function differences with respect to the electron emitter) are bimodal. Specifically, the sample-cathode work function differences in the MoSe₂ region are all close to $\Delta W_{\text{MoSe}_2} \approx 2.25 \text{ eV}$, whereas in the graphene regions $\Delta W_{\text{Gr}} \approx 1.5 \text{ eV}$. These numbers are consistent for many points on the surface, and are therefore taken to be representative of the entire imaged area. The work function difference (or equivalently, the vacuum level difference) between MoSe₂ and graphene is therefore $\delta E_{\text{vac}} = \Delta W_{\text{MoSe}_2} - \Delta W_{\text{Gr}} = 0.75 \text{ eV}$.

This is a significant effect, much larger than that observed in the WSe₂-EG samples discussed in Section 4.3. In order to understand this value, we consider possible doping in the MoSe₂ and graphene which leads to charge transfer and a subsequent interface dipole. Epitaxial graphene on 6H-SiC(0001), the substrate in this sample, is known to be *n*-type with a carrier density in the range of $2 \times 10^{12} \text{ cm}^{-2}$ to $6 \times 10^{12} \text{ cm}^{-2}$. [87, 93] Without knowing the precise value, it is still possible to estimate the MoSe₂ carrier density by calculating the amount of charge transfer required to produce a 0.75 eV work function difference between the layers for a range

of graphene carrier density values. The result of this calculation is summarized in Fig. 5.2, and is produced by balancing the electrostatics of a vertical junction of MoSe₂-EG subject to the constraint that $\delta E_{\text{vac}} = 0.75 \text{ eV}$ at Fermi equilibrium (after charge transfer), as outlined in Section 4.4. In addition, the band alignment between the layers of MoSe₂-EG is not precisely known, thus we repeat this calculation using several reported values for MoSe₂ and graphene electron affinities,[94, 101–103]

$$\chi_{\text{MoSe}_2} = E_{\text{vac}} - E_c \quad (5.1a)$$

$$\chi_{\text{Gr}} = E_{\text{vac}} - E_d, \quad (5.1b)$$

to establish the range of possible MoSe₂ doping densities based on conduction band offset,

$$\Delta E_c \equiv E_c - E_d = \chi_{\text{Gr}} - \chi_{\text{MoSe}_2} \quad (5.2)$$

with MoSe₂ conduction band edge E_c and graphene Dirac point E_d (the charge neutrality point of graphene, which is also the conduction band edge since the conduction and valence bands touch at this point).

With these points addressed, we find that the 0.75 eV work function difference between MoSe₂ and epitaxial graphene implies that the MoSe₂ began with a hole density of approximately $5 \times 10^{13} \text{ cm}^{-2}$, using the mean values of graphene electron density and conduction band offset (red curve in Fig. 5.2). This is an enormous number of carriers, which in this model are ascribed to an equivalent defect density in the MoSe₂ film. Specifically, these defect states (in this model) manifest as a large density-of-states near the valence band edge of the MoSe₂; shallow acceptor states which accept excess electrons from the graphene and thus generate a large dipole between the two layers.

Alternatively, it is possible that these defect states exist in a distribution throughout the band gap of MoSe₂. In this case the defect density would need to be even larger than $5 \times 10^{13} \text{ cm}^{-2}$ to produce the same 0.75 eV work function difference, since the same total number of defect states spread out over the band gap would only be partially filled after the charge transfer process, leading to additional unoccupied defect states. In other words, the same amount of charge is transferred in both models, but the shallow acceptor model (with a large number of defect states per unit energy near the valence band edge) admits a smaller number of defect states, all of which are filled during charge transfer. The shallow acceptor model, which implies that the MoSe₂ begins with large, unintentional *p*-type doping, therefore provides a conservative estimate of the defect density in the MoSe₂; it is more likely that there are in fact a larger number of defect states present in some distribution across the band gap. Recently, other workers have established the presence of dense networks of line defects and mirror-twin-boundaries that result in mid-gap states in MBE-formed MoSe₂. [104–106] These results provide further evidence that the MoSe₂ film in this study, also prepared by MBE, is indeed highly defective, with a spatial defect density of $5 \times 10^{13} \text{ cm}^{-2}$ or greater.

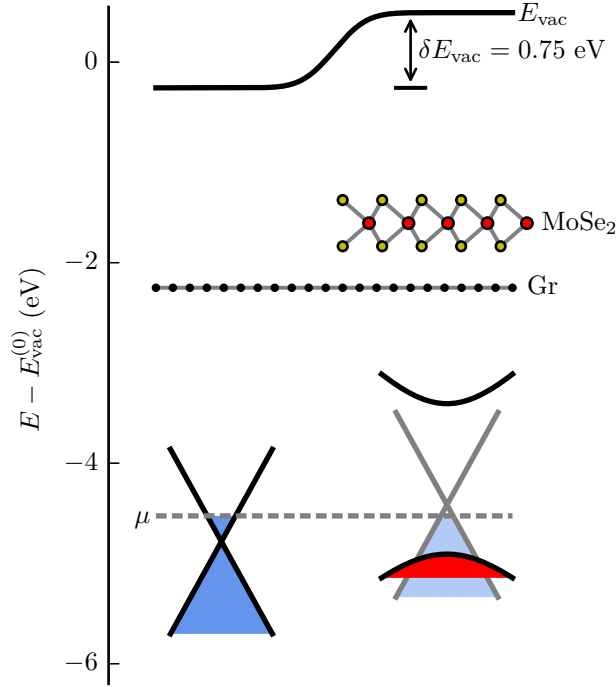


Figure 5.3: Model of equilibrium electrostatic potential and subsequent band alignment between regions of epitaxial graphene (EG) covered by MoSe_2 and neighboring bare EG regions. Structure model (not on energy scale) illustrates the layer order in covered region. MoSe_2 bands ($E(k_{\parallel})$ below each region) are superimposed on graphene bands in the covered region. Bare graphene regions are n -type, but regions covered by MoSe_2 become slightly p -type due to charge transfer with the MoSe_2 . Energy scale is referenced to the vacuum level of intrinsic graphene $E_{\text{vac}}^{(0)}$, that is, without doping or charge transfer.

Regardless of the energetic distribution of defect states, the quantity of charge transferred between the graphene and MoSe₂ (which is the same in both models) is rather large, and produces semiconducting MoSe₂, with the Fermi level in the band gap of the MoSe₂ and slightly *p*-type graphene in covered areas, as shown in Fig. 5.3. Based on the results of Chapter 4, we therefore conclude that the contact between the MoSe₂ film and the epitaxial graphene below is not ohmic, and would therefore serve better as a tunneling barrier than as a contact or conducting medium. In this case, of course, this conclusion is based on LEEM analysis alone, demonstrating an additional application of the method developed in Chapter 4.

Chapter 6

Theoretical background

Regarding potential applications of 2D heterostructures, it is the focus to the remainder of the thesis to investigate interlayer tunneling in layered heterostructures from a theoretical perspective. Although the experimental findings of the previous chapters provide meaningful contributions to the field on their own, these works are additionally motivated by several key predictions which will be the subject of the following chapters. Given that there are many exciting and novel properties of 2D materials, particularly pertaining to electronic behavior, it is therefore expected that there will be equally novel and exciting properties in electronic devices based on such materials. Interlayer tunneling devices in particular are an interesting starting point for such considerations since the atomic flatness, lack of dangling bonds, and highly-ordered nature of clean interfaces between 2D materials have the potential to be superior to those found in bulk materials. These properties are highly favorable for tunneling applications, wherein the width, sharpness, and uniformity of the tunneling barrier are critical parameters; tunneling rates typically being exponentially-sensitive to such quantities. A pristine interface between graphene and hexagonal boron nitride, for example, may very well be the absolute limit of atomic sharpness and uniformity in condensed matter systems. Moreover, there are topological advantages of using a layered 2D geometry, beginning with the fact that it is possible to independently modulate the electrostatic conditions of two opposing 2D layers with fields from either side of the junction, not to mention various other consequences related to screening of charges, in-plane and out-of-plane fields, and so on.

With these concepts as motivation, we proceed to study interlayer tunneling between 2D materials in the following chapters with theory and computation. In Chapter 6 we establish the theoretical groundwork for computing tunneling currents between 2D layers, and the electrostatics necessary to simulate realistic devices. The theory of 2D–2D tunneling between monolayers of graphene separated by hexagonal boron nitride is discussed in detail in Chapter 7, followed by comparisons to experimentally measured tunneling currents in similar structures. Chapter 8 addresses tunneling between bilayers of graphene, which requires additional theoretical com-

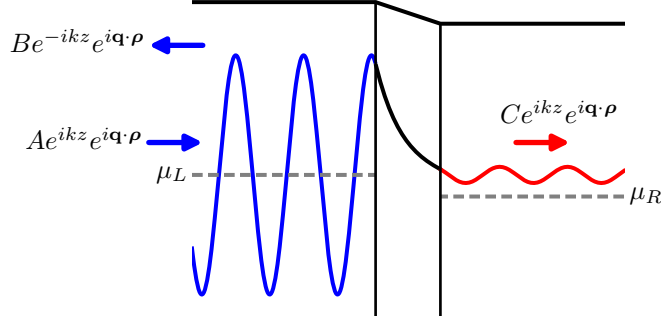


Figure 6.1: Diagram illustrating exact solution to the typical 3D tunneling problem, with incident and reflected propagating waves on the left side of the barrier, and an outgoing transmitted wave on the right. Wavefunctions are separated into z -dependent and $\boldsymbol{\rho} = (x, y)$ components. For a given state, current is obtained by integrating the current density (Eq. (6.1)) over the x, y plane.

plexity but allows for interesting new phenomena compared to monolayer graphene. Finally, a brief summary of experimental progress toward actual fabrication of tunneling devices is provided in Chapter 9.

6.1 Interlayer tunneling between 2D materials and the Bardeen method

Tunneling between sheets of 2D materials requires, in comparison to 3D materials, a new way of visualizing the tunneling process. To illustrate the situation, let us refer to Fig. 6.1 which shows the regular tunneling problem between two semi-infinite 3D electrodes. Considering a wave incident from the left on the tunnel barrier, then there will be a reflected wave in the left-hand electrode and a transmitted wave in the right-hand electrode. From the ratio of the magnitudes of the transmitted to the incident wave, one obtains the transmission probability T . Summing up these transmission probabilities with suitable prefactors, one then obtains the total tunnel current. The states thus formed are exact eigenstates of the system, and this procedure of obtaining the current is equivalent to simply computing the current for each state, using

$$\begin{aligned}
 j_z &= \frac{e\hbar}{2mi} \left[\psi^* \left(\frac{\partial\psi}{\partial z} \right) - \psi \left(\frac{\partial\psi^*}{\partial z} \right) \right] \\
 &= \frac{e}{m} \operatorname{Re} \left(\psi^* \frac{\hbar}{i} \frac{\partial\psi}{\partial z} \right),
 \end{aligned} \tag{6.1}$$

and then summing these individual currents over all the states. This type of solution of the tunneling problem applies equally well to 1D or 3D electrodes, with the latter

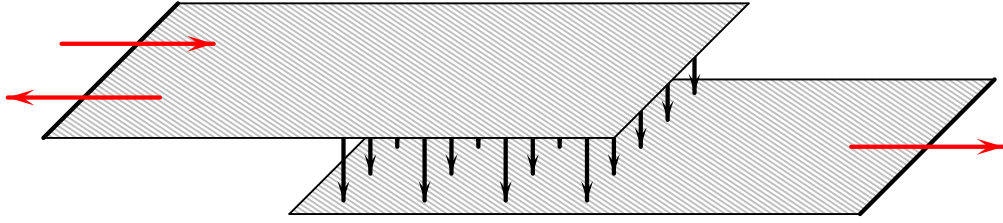


Figure 6.2: Scheme for considering interlayer 2D–2D tunneling in an exact manner, with current flowing laterally along each electrode (propagating waves, with possible reflection and transmission). Tunneling occurs between the layers in the overlap region (without propagation in the z -direction), with transmitted states maintaining their initial lateral momentum after tunneling. Analytic solutions do not exist for this problem, even for simple band structures, and computational solutions are impractical for realistic band structures.

case handled in a separable manner in which the perpendicular component of the energy and momentum for each state are employed in the summation needed to obtain the tunneling current.

Now consider the analogous 2D problem in which the electrodes of Fig. 6.1 are narrow sheets containing just one (or a few) quantum state(s) in the direction perpendicular to the sheets. Such states do not have any momentum perpendicular to the 2D sheets. That is, the states within the 2D materials are manifestly *not* propagating ones in the direction perpendicular to the sheets. Hence, there is no obvious way to apply a similar procedure as used for the 3D problem. For this reason, one must approach the problem in a different way.

To treat the 2D–2D tunneling problem in an exact manner, one must consider the current flowing along the 2D electrodes and then passing between the electrodes in a direction perpendicular to the original current flow, as pictured in Fig. 6.2. We show there a propagating state approaching the tunnel junction (overlap area of the two sheets) from one side of the left-hand electrode. When this state (wavepacket) reaches the junction, it will spread out into the neighboring electrode, and some fraction of the state will then propagate (in the same direction as the original state) in the other electrode. In this way, we can still manage to obtain a transmission probability T for the tunneling process (and a current for each state), and by suitably summing these probabilities (or individual currents), the total tunneling current is obtained. This method for treating the 2D problem is clearly more complicated than that employed for the 3D problem, since, again, the tunneling process is occurring in a direction that is perpendicular (or, at least, not collinear) with the propagation direction of the original state.

Because of this inherent complexity of the 2D–2D tunneling problem, simple analytic solutions for this problem do not exist. Even with very simple models for the 2D electronic band structures, it is necessary to couple plane waves into the junction

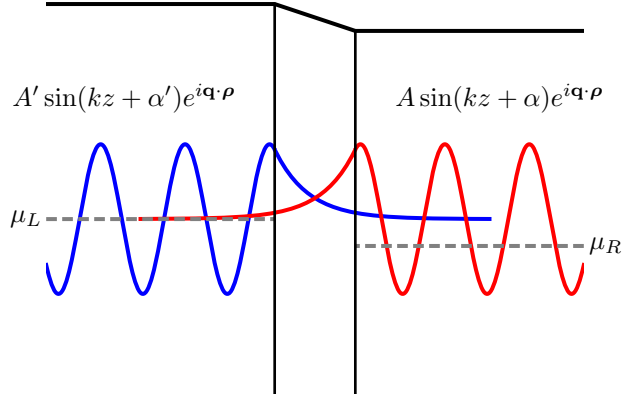


Figure 6.3: Illustration of the 3D–3D tunneling problem in the Bardeen approach. Wavefunctions are first determined using a semi-infinite barrier (and thus the solutions are non-propagating), and the presence of available states in the opposing electrode is treated as a perturbation on the initial Hamiltonian on each side of the barrier. Current is obtained (despite non-propagating waves) through a reformulation of Fermi’s Golden Rule, as described in Eqs. (6.2).

and allow them to “spread out” in the direction perpendicular to their propagation direction. The non-equilibrium Green’s function (NEGF)[107] method provides a formalism for achieving this sort of coupling of states from contacts to the 2D materials, as in the far left edge of the upper 2D sheet in Fig. 6.2 and the far right of the lower sheet. The solutions thus obtained for the tunneling current are exact, within the model used for the electronic band structures. However, the overall computational complexity of the 2D–2D tunneling problem precludes the use of realistic band structures for the 2D material, and even for very simple band-structure models it is not possible to obtain analytic solutions for the tunnel current.

Fortunately, an alternative treatment of the tunneling problem exists from the work of Bardeen [108], and it can be directly employed for the 2D–2D tunneling problem. This method can also be used for 3D–3D tunneling (as commonly used for analysis of problems involving the scanning tunneling microscope[109]), and we illustrate that situation in Fig. 6.3. The essence of the method is that we start with exact solutions for the wavefunctions in each electrode in the absence of the opposing electrode, and then in a time-dependent, first-order perturbation computation (Fermi’s Golden Rule), we compute the probability of an electron in a state of one electrode making a transition into a state of the other electrode. Consider the states shown in the left-hand electrode of Fig. 6.3. Such states are solutions of the single-electrode problem, with vacuum on one side of the electrode. Due to the presence of the vacuum, the states are necessarily non-propagating, that is, they carry no current in the direction perpendicular to the electrode surface.

Starting with these states of the single-electrode problem, now consider adding the

opposing electrode to the problem, and then computing the transition of the state in the left-hand electrode over to a state of the same energy in the right-hand electrode. Fermi's Golden Rule can be used to obtain the total transition probability, and hence the tunnel current, for all participating states. At first glance it may appear that such a perturbative treatment is invalid, since certainly the perturbing potential of the right-hand electrode (its Hartree potential, in a single-particle treatment) is very large, of order 10^1 eV to 10^2 eV. However, Bardeen demonstrated that what is important for the validity of the approach is not the size of this potential itself, but rather, the size of the potential multiplied by the probability amplitude (wavefunction squared) of the state from the left-hand electrode.[108] In other words, so long as the tunneling barrier is sufficiently high and/or broad, then the approach is valid. Certainly for the problems that we consider in this thesis, with tunnel barrier containing several layer of h-BN, this condition is well satisfied.

A second important result obtained by Bardeen was a reformulation of the expression from Fermi's Golden Rule into a form that is much more convenient to evaluate.[108] Recall that in a usual time-dependent perturbation treatment, one would have to evaluate integrals (matrix elements) that extend over the entire volume spanned by the potential of the right-hand electrode, that is, involving the potential of the right-hand electrode and the wavefunctions of both the left- and right-hand electrodes. Bardeen demonstrated that this type of integral can be rewritten as simply a surface integral over a boundary that separates the two electrodes, with this surface integral involving only the wavefunctions of the respective states of the left- and right-hand electrodes and not the potential of the right-hand electrode,

$$I = \frac{2\pi e}{\hbar} \sum_{ij} |M_{ij}|^2 \delta(E_i - E_j) [f_L(E_i) - f_R(E_j)], \quad (6.2a)$$

$$M_{ij} = \frac{\hbar^2}{2m} \int d^2\rho \left[(\psi'_i)^* \left(\frac{\partial \psi_j}{\partial z} \right) - \psi_j \left(\frac{\partial \psi'_i}{\partial z} \right)^* \right]. \quad (6.2b)$$

In this way, the tunneling current can be seen to be determined by the “overlap” of the states of the two electrodes at a location near or at the midpoint of the tunnel barrier.

The Bardeen method can be applied in a straightforward manner to the 2D–2D tunneling problem. We simply replace the semi-infinite electrodes of Fig. 6.3 with thin sheets of material. The resultant quantum states of the 2D sheets do not have propagating character in the direction perpendicular to the sheets, however, such character is not required for application of the Bardeen method.

Hence, a relatively simple solution for the 2D–2D tunneling problem can be obtained with this method. Compared to the situation pictured in Fig. 6.2 for 2D–2D tunneling, which applies to the exact solution (using the NEGF method), the solution using the Bardeen method can be illustrated as shown in Fig. 6.4. It is not necessary to consider the lateral current in the 2D electrodes, nor involve the contacts to those electrodes. Rather, the method allows us to focus simply on the flow of current across

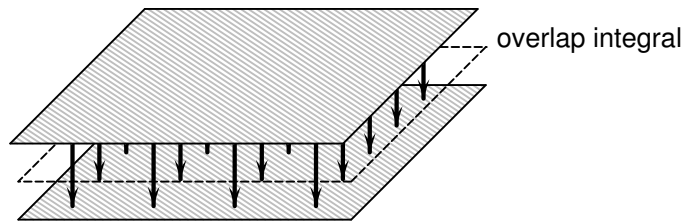


Figure 6.4: Illustration of the Bardeen method applied to 2D-2D tunneling, with states in each layer computed separately, without the presence of the opposing layer. The wavefunctions in each layer have no propagating component in the tunneling direction. As a simplification to standard first-order perturbation theory, tunneling current is computed by evaluating a surface integral in the middle of the barrier using the matrix element defined in Eq. (6.2b), as opposed to computing a full volume integral over a region containing a perturbing potential.

the tunnel barrier itself. Of course, the transport of carriers within the sheets may indeed be important in a full analysis of the problem, depending on the efficacy of transport in the sheets compared to across the barrier. Nevertheless, the Bardeen method allows us to on focus on the flow of current through only the barrier, as an initial, important step in the analysis of the entire problem.

6.2 Tunneling between monolayers of graphene

6.2.1 Theoretical formalism

In this section we review the case of tunneling between two graphene sheets as first worked out by Feenstra et al. [110]. This review provides a good illustration of the Bardeen tunneling method described in Section 6.1, and it also forms the basis for later work presented in Chapters 7 and 8 of the thesis. We begin by considering tunneling between two graphene monolayers in the out-of-plane direction, z . In the Bardeen approach, the tunneling current is computed by calculating the overlap of the wavefunctions from either side of the tunneling barrier, in the middle of the barrier. This is a perturbative approach; the barrier is first treated as a semi-infinite object for each electrode separately, and the introduction of the opposite electrode (with real states) is viewed as a perturbation on the barrier region. This of course relies on the assumption of weak overlap in the barrier, as discussed in Section 6.1. Beginning with a sum over transitions from states α in the left-hand (L) graphene electrode to states β in the right-hand (R) electrode (and vice-versa),

$$I = g_S g_V e \sum_{\alpha, \beta} \left\{ \frac{1}{\tau_{\alpha\beta}} f_L(E_\alpha) [1 - f_R(E_\beta)] - \frac{1}{\tau_{\beta\alpha}} f_R(E_\beta) [1 - f_L(E_\alpha)] \right\}, \quad (6.3)$$

with tunneling rates $\tau_{\alpha\beta}^{-1}$ and $\tau_{\beta\alpha}^{-1}$ for electrons going from $L \rightarrow R$ and $R \rightarrow L$, respectively, and Fermi occupation factors f_L and f_R for each electrode defined in the usual way, $f(E) = \{1 + \exp[(E - \mu)/k_B T]\}^{-1}$. [110] The tunneling transition probabilities,

$$\frac{1}{\tau_{\alpha\beta}} = \frac{2\pi}{\hbar} |M_{\alpha\beta}|^2 \delta(E_\alpha - E_\beta) = \frac{1}{\tau_{\beta\alpha}}, \quad (6.4)$$

are proportional to the square of a matrix element which includes the wavefunction overlap evaluated over the 2D surface in the middle of the barrier region,

$$M_{\alpha\beta} = \frac{\hbar^2}{2m} \int dS \left(\Psi_\alpha^* \frac{d\Psi_\beta}{dz} - \Psi_\beta \frac{d\Psi_\alpha^*}{dz} \right), \quad (6.5)$$

with wavefunctions in the left- and right-hand electrodes $\Psi_\alpha(\mathbf{r}, z)$ and $\Psi_\beta(\mathbf{r}, z)$. The tunneling current including these elements becomes [110]

$$I = g_S g_V \frac{2\pi e}{\hbar} \sum_{\alpha, \beta} |M_{\alpha\beta}|^2 [f_L(E_\alpha) - f_R(E_\beta)] \delta(E_\alpha - E_\beta), \quad (6.6)$$

with spin and valley degeneracies $g_S, g_V = 2$. Equation (6.6) echoes the form of Fermi's Golden Rule from time-dependent perturbation theory, however, with the reformulation described in Section 6.1

6.2.2 Simulation of tunneling characteristics

Using the formalism developed in Section 6.2.1, we proceed to compute tunneling current by numerical evaluation of Eq. (6.6) using the wavefunctions for graphene introduced in Section 1.1.1 with an additional, decaying $e^{-\kappa z}$ component in the out-of-plane direction. With these wavefunctions, the matrix element is explicitly written in terms of the wavevectors in each electrode, $\mathbf{k}_L, \mathbf{k}_R$, as evaluated in Section 7.2 and shown in Eq. (7.4),

$$M_{\mathbf{k}_L, \mathbf{k}_R} = \frac{\hbar^2 \kappa}{2AmD} e^{-\kappa d} g_\omega(\theta_L, \theta_R) \int dS e^{i\mathbf{Q}\cdot\mathbf{r}} e^{i(\mathbf{k}_R - \mathbf{k}_L)\cdot\mathbf{r}} \quad (6.7)$$

with misorientation vector \mathbf{Q} introduced to quantify angular rotation ω between the two graphene lattices, and chiral parts of the wavefunctions $g_\omega(\theta_L, \theta_R)$.

A typical simulated structure is shown in Fig. 6.5(a), with two monolayers of graphene separated by a few layers of hexagonal boron nitride (h-BN), a 2D insulator. Tunneling occurs for non-zero values of bias voltage applied between the two graphene electrodes. For each bias voltage value, the electrostatics are solved independently (as discussed in Section 6.3), and subsequently used to evaluate the current with Eq. (6.6). For a given bias voltage, only states with:

1. matching energy (imposed by the δ -function in Eq. (6.6)),
2. matching lateral wavevector (momentum- or \mathbf{k} -conservation, due to the $e^{i(\mathbf{k}_R - \mathbf{k}_L)\cdot\mathbf{r}}$ term in the surface integral of Eq. (6.7)),
3. and only states between the two Fermi energies (from occupied to unoccupied states)

are allowed to participate in the tunneling. Due to the restriction of \mathbf{k} -conservation in particular, and the reduced number of bands in two-dimensional graphene compared to bulk materials, the tunneling current is highly non-linear with respect to bias voltage.

For example, for rotationally aligned graphene crystals ($\mathbf{Q} = 0$), at one particular bias voltage the graphene bands from either side of the junction will be energetically aligned (Fig. 6.5(b)). In this special case, all states between the two Fermi levels have matching energy and momentum with states on the other side of the junction, so tunneling occurs between between all of these states simultaneously. On the other hand, for any other bias voltage the bands will be energetically offset from one another (Fig. 6.5(c)), and although there are many states with matching energy in the opposing electrode, there will in general only be a few states with matching wavevector, and

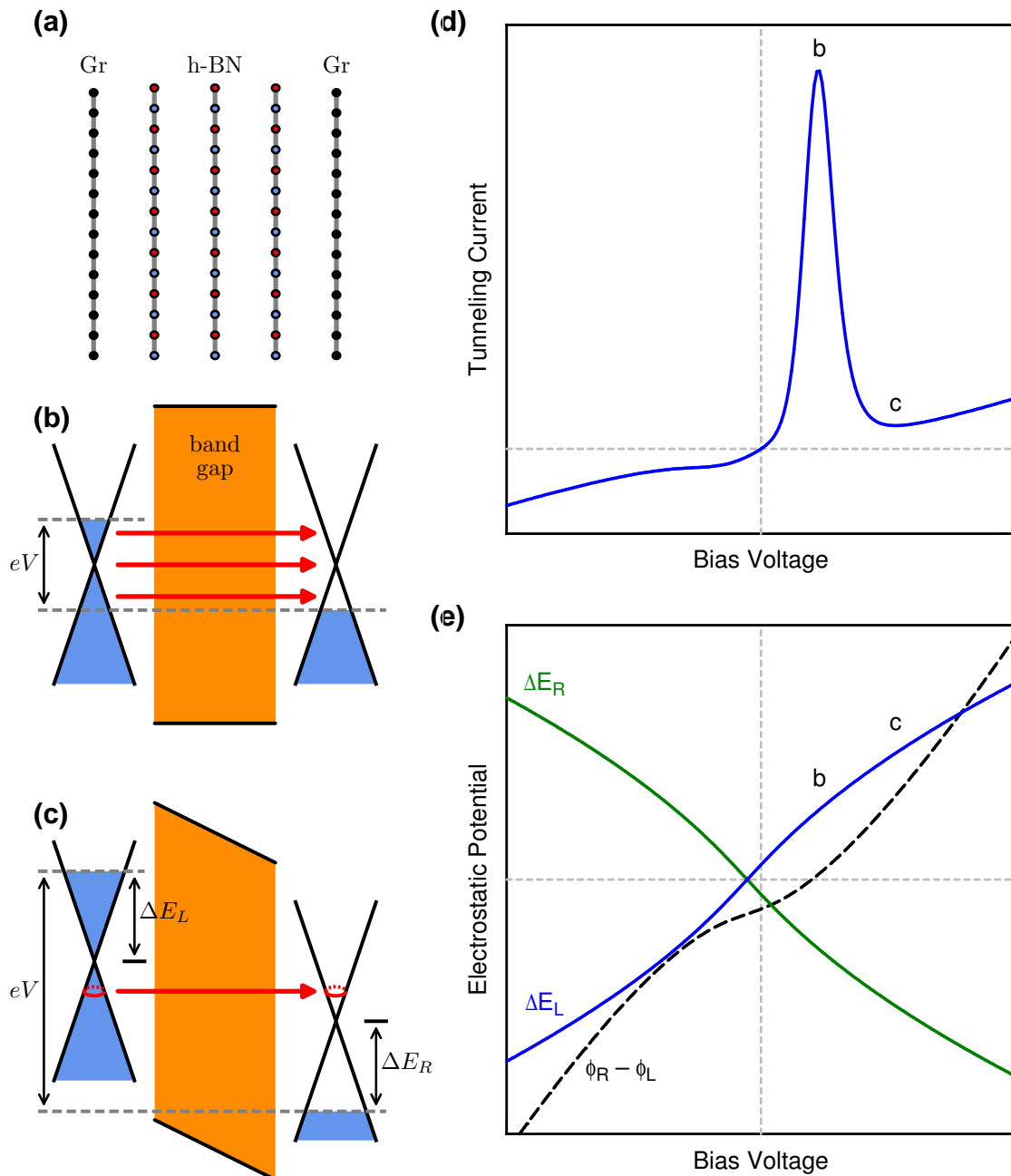


Figure 6.5: (a) Schematic for graphene-insulator-graphene (GIG) tunneling structure, with two monolayers of graphene separated by an insulating barrier, in this case, a few layers of hexagonal boron nitride. (b) Band diagram for GIG junction at resonance. (c) Band diagram for GIG junction off-resonance, in the valley region of the I - V characteristic. (d) Simulated current-voltage (I - V) characteristic computed as described in Section 6.2.1. (e) Simulated electrostatics of the same, showing Fermi shifts $\Delta E = \mu - \phi$ for each electrode, and potential across the barrier $\phi_R - \phi_L$.

thus the current is greatly reduced for all other voltages. Matching states occur at the intersection of the bands in momentum space, so for graphene electrodes in rotational alignment, a single ring of states satisfies this condition (red ring in Fig. 6.5(c)) along each Dirac cone. This leads to resonant tunneling in the current–voltage (I – V) characteristic (Fig. 6.5(d), and a phenomenon known as *negative differential resistance* (NDR) in the voltage range where $\partial I/\partial V < 0$.

In principle, upholding strict wavevector conservation would lead to a δ -function-like spike in the tunneling current at the resonance voltage,[110] however, in practice there are several sources of decoherence which serve to relax the wavevector conservation condition and thus broaden the resonant tunneling effect. To capture this behavior, the surface integral in the tunneling matrix element defined in Eq. (6.5), normally evaluated over all space in the lateral dimensions, is restricted to a finite region of wavefunction coherence[110] as discussed in detail in Chapter 7.

6.3 Electrostatics of layered 2D heterostructures

In order to calculate a tunneling current as a function of bias voltage applied across the 2D layers, the potential difference is placed appropriately within the energy arguments of the Fermi functions and δ -function themselves in Eq. (6.6) such that,

$$E_\alpha = E(\mathbf{k}_L) + \phi_L = E(\mathbf{k}_L) + \mu_L - \Delta E_L, \quad (6.8a)$$

$$E_\beta = E(\mathbf{k}_R) + \phi_R = E(\mathbf{k}_R) + \mu_R - \Delta E_R, \quad (6.8b)$$

where ϕ_L , ϕ_R refer to the electrostatic potential energies of each graphene sheet, and $\phi \equiv \mu - \Delta E$. Here, we find the explicit terms for the electrode Fermi energies, μ_L and μ_R , the difference of which is defined as the electrostatic potential bias,

$$eV \equiv \mu_R - \mu_L. \quad (6.9)$$

In Eqs. (6.8), we have introduced two new quantities, ΔE_L and ΔE_R , which represent position of the Fermi level in each electrode relative to the charge neutrality point of the graphene band structure (as discussed in Section 1.1.1). In the work of Feenstra et al. [110], these terms were combined into one value, ΔE , which was equal in magnitude and opposite in sign between the two graphene layers due to the symmetry of the electrostatics model described therein. In a subsequent work, Zhao et al. [111] calculated the tunneling current between two graphene sheets sandwiched between top and bottom gates, with a symmetric geometry and antisymmetric gate biases in order to enable an analytic form for the tunneling current. The simplification of symmetric gating again allows the use of a single ΔE term, since the effect of the gate fields (with opposite biases applied to the opposing electrodes) is to modulate the position of the bands with respect to the Fermi levels, and given a symmetric geometry the modulation is of equal magnitude on both sides. Here, for the sake of including gate modulation in more realistic geometries, we introduce a generalized method for

calculating the electrostatics of layered 2D structures with arbitrary biases, as an extension to the work of Feenstra et al. [110] and Zhao et al. [111].

6.3.1 Potentials between two monolayers with top and bottom gates

This calculation is intended to provide a general formalism for solving the electrostatics of a gated graphene–insulator–graphene junction in a parallel-plate geometry. The convention will be to label a back gate with voltage V_{BG} followed by source and drain electrodes, and a top gate (V_{S} , V_{D} , and V_{TG} , respectively). Switching from the notation of Section 6.2, the graphene electrodes are now labeled as source ($L \rightarrow S$) and drain ($R \rightarrow D$) in the parlance of electronic transport in field-effect transistors.

We define the system of conductors with $\mathbf{q} = \hat{\mathbf{C}}\mathbf{V}$, which for four conductors will take the explicit form,

$$\begin{pmatrix} q_1 \\ q_2 \\ q_3 \\ q_4 \end{pmatrix} = \begin{pmatrix} C_{11} & C_{12} & C_{13} & C_{14} \\ C_{21} & C_{22} & C_{23} & C_{24} \\ C_{31} & C_{32} & C_{33} & C_{34} \\ C_{41} & C_{42} & C_{43} & C_{44} \end{pmatrix} \begin{pmatrix} V_1 \\ V_2 \\ V_3 \\ V_4 \end{pmatrix}, \quad (6.10)$$

with symmetric coefficients of capacitance $C_{ij} = C_{ji} = \partial q_i / \partial V_j$, which give the total charge on a each conductor at unit potential, holding all other potentials constant. In our model (2D layers which extend to infinity in the lateral dimensions), each conductor is only sensitive to its immediate neighbors, so a few of these matrix elements are zero ($C_{ij} = 0$ for $i < |j + 1|$). Furthermore, since our overall system is charge neutral $\sum_i q_i = 0$ and since the result should not depend on the choice of ground potential $V_i \rightarrow V_i + \delta V$, it follows that $\sum_j C_{ij} = 0$, and therefore we write the diagonal elements as $C_{ii} = -\sum_j C_{ij}$,

$$\begin{pmatrix} q_1 \\ q_2 \\ q_3 \\ q_4 \end{pmatrix} = \begin{pmatrix} -C_{12} & C_{12} & & \\ C_{12} & -C_{12} - C_{23} & C_{23} & \\ & C_{23} & -C_{23} - C_{34} & C_{34} \\ & & C_{34} & -C_{34} \end{pmatrix} \begin{pmatrix} V_1 \\ V_2 \\ V_3 \\ V_4 \end{pmatrix}. \quad (6.11)$$

For metal gates, we identify the potentials $V_1 = V_{\text{BG}}$ and $V_4 = V_{\text{TG}}$, but the graphene potentials are defined as $V_2 = -\phi_S/e$ and $V_3 = -\phi_D/e$ in terms of the electrostatic potentials ϕ_i at the charge neutrality point. In addition, we relabel the capacitances in accordance with each dielectric between elements, $C_{12} = C_{\text{BG}}$, $C_{23} = C_{\text{t}}$, and $C_{34} = C_{\text{TG}}$. With these identifications, we rewrite the two middle equations,

$$q_{\text{S}} = C_{\text{BG}}(V_{\text{BG}} + \phi_S/e) + C_{\text{t}}(\phi_S - \phi_D)/e, \quad (6.12a)$$

$$q_{\text{D}} = C_{\text{TG}}(V_{\text{TG}} + \phi_D/e) + C_{\text{t}}(\phi_D - \phi_S)/e. \quad (6.12b)$$

The net sheet charge density on each electrode is given by

$$q_i = e [(n_i - p_i) - N_i], \quad (6.13)$$

for electron and hole densities n_i , p_i and electrostatic doping (externally-induced carriers) N_i . The charge densities are defined in the usual way,

$$n_i = \int_{\phi_i}^{\infty} dE \frac{\rho_i(E)}{e^{(E-\mu_i)/kT} + 1}, \quad (6.14a)$$

$$p_i = \int_{-\infty}^{\phi_i} dE \frac{\rho_i(E)}{e^{(\mu_i-E)/kT} + 1}. \quad (6.14b)$$

We may then solve Eq. (6.12a) for ϕ_D and insert the solution into Eq. (6.12b) to obtain a single equation which must be solved self-consistently to obtain ϕ_S . The result is then inserted back into Eq. (6.12a) to obtain ϕ_D . For convenience, we introduce $\Delta E_D = \mu_D - \phi_D$ and $\Delta E_S = \mu_S - \phi_S$ and re-parametrize the problem in terms of the Fermi shifts $\Delta E_{D,S}$. Solving for the electrostatic potentials $\phi_{D,S}$, or equivalently, the Fermi shifts $\Delta E_{D,S}$, fully describes the electrostatics needed for the tunneling calculation, as shown in Fig. 6.5(e). In terms of the relevant physics, the classical capacitances of the tunnel barrier and gate dielectrics appear on the right sides of Eqs. (6.12), whereas the *quantum capacitances* of the graphene electrodes (which are significant given the geometry of the layers) and thermal distribution of electrons are encoded in the Fermi integrals that appear in the charge terms on the left sides of these equations.

6.3.2 The special case of bilayer graphene

Due to the fact that the band structure of bilayer graphene (and thus, the density-of-states, which directly affects charge distribution) is modulated by the application of a transverse electric field component, the electrostatics for the double-bilayer tunnel junction must be solved iteratively. The order of material layers for this section is back gate–source–drain–top gate, as in Section 6.3.1. We begin by considering each layer of graphene as a separate monolayer with potential ϕ_i for $i = 0, 1, 2, 3$ in order to calculate the potential differences across each bilayer,

$$U_S = \phi_1 - \phi_0, \quad (6.15)$$

$$U_D = \phi_3 - \phi_2. \quad (6.16)$$

We obtain the full set of coupled electrostatic equations for the four monolayers and two gates by filling in the matrix equation $q_i = C_{ij}V_j$ with the appropriate potentials

which is calculated using the tight-binding dispersion for bilayer graphene, and depends on the potential differences U_i calculated in the first part of the method. Here, n represents a sub-band index. The remaining equation is solved self-consistently to obtain the potential ϕ_S (ϕ_D), which is re-inserted into the system given in Eq. (6.19) to determine ϕ_D (ϕ_S), and subsequently the Fermi shifts ΔE_S and ΔE_D .

Chapter 7

Theory of graphene–insulator–graphene tunnel junctions

In this chapter, details of graphene–insulator–graphene vertical tunneling structures are discussed from a theoretical perspective. Momentum conservation in such devices leads to highly nonlinear current–voltage characteristics, which with gates on the tunnel junction form potentially useful transistor structures. Two prior theoretical treatments of such devices are discussed; the treatments are shown to be formally equivalent, although some differences in their implementations are identified. The limit of zero momentum conservation in the theory is explicitly considered, with a formula involving the density-of-states of the graphene electrodes recovered in this limit. Finally, various predictions of the theory are compared to experiment. The work described in this chapter appears in published form in Refs. 1 and 2.

7.1 Introduction

Recently, several research groups have reported theoretical and/or experimental results relating to vertical graphene–insulator–graphene (GIG) tunneling structures. The first such report dealt with coupled electron and hole gases in the two opposing electrodes, predicted to form an exciton condensate that might survive at temperatures as high as room temperature.[29, 30] The presence of this condensate leads to an enhanced tunnel current (i.e. since the electrons and holes in opposing electrodes have correlated spatial locations), but for a sufficiently high current the condensate is expected to be quenched. Hence, a very nonlinear relationship of tunnel current to voltage across the device, with negative differential resistance (NDR), is expected. With a gate electrode on the device, a transistor-like operation is achieved in a device termed a *BiSFET*. We are not aware of experimental observation of the BiSFET tunnel characteristic to date, although research on such devices is likely continuing.

Following the BiSFET proposal it was realized by Feenstra et al. [110] that, even in the absence of electron-hole coupling between the graphene electrodes, the *single-particle* tunneling characteristics of GIG devices can be highly nonlinear. The reason for this behavior arises from *momentum conservation* in the device, i.e. the requirement that the lateral components of the wavefunctions for tunneling states in both electrodes have the same (or nearly the same) wavevectors. A theory was developed in which momentum conservation in an actual device was shown to depend on the crystallographic order of the graphene electrodes, which is limited by a finite size tunneling area (grains of the graphene) or through scattering from defects in the graphene or insulator layers.[110] The effective size of ordered regions in the electrodes can be characterized by a *coherence length*, with momentum conservation being more rigorously followed when the coherence length is large.

Experimentally, early results by Britnell et al. [112] from GIG junctions did not display any NDR. Indeed, their theoretical description of such devices employed a theory in which momentum conservation is completely neglected. Similarly, NDR was not seen in early reports from Roy et al. [113] for GIG junctions. However, later results from Britnell et al. [31] did reveal NDR in the GIG devices, and a correspondingly more general theory was described in which momentum conservation is included. Related theories have been recently presented by other authors.[114–116]

In this work we compare the theoretical description by Britnell et al. [31] for GIG devices to the earlier treatment of Feenstra et al. [110]. We find that the two treatments are equivalent, at least in the limit of zero misorientation angle between the graphene electrodes. This equivalence between the two theories, and the possible effects of misorientation, are discussed in the following section. We also discuss the limit in which momentum conservation is completely neglected,[112] dealing in particular with the problem of how to obtain absolute current magnitudes in that case. In Section 7.3 we focus on hexagonal boron nitride (h-BN) barrier materials, describing their complex band structure and hence revealing the energy dependence of the tunneling decay constant. A comparison of the theoretical results with experiment is given in Section 7.4, and the paper is summarized in Section 7.5.

7.2 Theoretical formalism

In a prior report, Britnell et al. [112] presented experimental data for current–voltage characteristics of a single-gated GIG junction, and interpreted the characteristics using a theory in which momentum conservation is completely neglected. As described in their work, the expression for the current then has the form

$$I \propto \int D_L(E)D_R(E)T(E) [f_L(E) - f_R(E)] dE \quad (7.1)$$

where D_L and D_R are the densities-of-states for the left- and right-hand electrodes, respectively, f_L and f_R are their Fermi-Dirac occupations factors, and $T(E)$ is a

tunneling transmission term. In this expression the shift in the states and Fermi energies of the two electrodes due to a voltage bias V between them is contained within the D_L , D_R , f_L , and f_R terms, rather than in the energy arguments themselves as done in Ref. 112, so as to be consistent with the formalism presented below.

When momentum conservation (wavevector conservation) for the lateral parts of wavefunctions in the two graphene electrodes is included, then the theory becomes significantly more complex as discussed in Refs. 110 and 31, which employ theories that might appear at first glance to be quite different. We compare those two theories in this section, showing that they are actually equivalent for the situation of zero misorientation angle between the graphene electrodes. We discuss possible effects due to misorientation, and we also identify a few other differences in implementation of the two theories.

In Ref. 110, tunneling between two graphene electrodes is written in the Bardeen formalism[108, 117–119] in which the current is given by Eq. (6.6),

$$I = g_V \frac{4\pi e}{\hbar} \sum_{\alpha, \beta} |M_{\alpha\beta}|^2 [f_L(E_\alpha) - f_R(E_\beta)] \delta(E_\alpha - E_\beta) \quad (7.2)$$

where g_V is the valley degeneracy of graphene, and the summation extends over all states α, β of the left- and right-hand electrodes, respectively. The matrix element $M_{\alpha\beta}$ is given by Eq. (6.5),

$$M_{\alpha\beta} = \frac{\hbar^2}{2m} \int dS \left(\Psi_\alpha^* \frac{d\Psi_\beta}{dz} - \Psi_\beta \frac{d\Psi_\alpha^*}{dz} \right) \quad (7.3)$$

where m is the free electron mass and $\Psi_\alpha(\mathbf{r}, z)$ and $\Psi_\beta(\mathbf{r}, z)$ are the wavefunctions of the left- and right-hand electrodes (each of those electrodes taken to be connected to a semi-infinite barrier), respectively. For a graphene–insulator–graphene junction, $M_{\alpha\beta}$ is evaluated in Ref. 110 by assuming the wavefunctions to be separable, with exponentially decaying z -components and with lateral components that have Bloch form, yielding

$$M_{\alpha\beta} = \frac{\hbar^2 \kappa}{2AmD} e^{-\kappa d} g_\omega(\theta_L, \theta_R) \int dS e^{i\mathbf{Q}\cdot\mathbf{r}} e^{i(\mathbf{k}_R - \mathbf{k}_L)\cdot\mathbf{r}} \quad (7.4)$$

where $g_\omega(\theta_L, \theta_R)$ is an expression of order unity that involves the overlap of periodic part of the lateral wavefunctions (θ_L and θ_R being the angular orientation of their wavevector relative to the respective Dirac point), \mathbf{Q} is the misorientation vector of the graphene electrodes with corresponding misorientation angle ω , and where \mathbf{k}_L and \mathbf{k}_R are the lateral wavevectors of the states in the left- and right-hand electrodes, relative to their respective Dirac points. All other parameters are defined precisely as in Ref. 110. Significantly, in Ref. 110 the surface integral of this equation is restricted in lateral extent, L , for both the x and y directions. This restriction can arise from

the lateral extent of the graphene grains in the electrodes, i.e. a “structural coherence length”, as proposed in Ref. 110.

Turning to the theory of Ref. 31, the matrix element for the tunneling process is written there as

$$M_{\alpha\beta}^S = \int_V dV \Psi_\alpha^*(\mathbf{r}, z) V_S(\mathbf{r}, z) \Psi_\beta(\mathbf{r}, z) \quad (7.5)$$

where the integral extends over all space and V_S is denoted a “scattering potential”. In the computations of Ref. 31 this scattering potential is taken to be localized over the region of the tunnel barrier. Although this form appears to be quite different than that of Eq. (7.3), we demonstrate now that the two methods are equivalent.

Following Ref. 31, Eq. (7.5) is evaluated as (using notation of the present work)

$$M_{\alpha\beta}^S = \frac{1}{AD} e^{-\kappa d} u_{11}^2 e^{i(\theta_L - \theta_R + \omega)/2} \Xi \int dS e^{i\mathbf{Q}\cdot\mathbf{r}} e^{i(\mathbf{k}_R - \mathbf{k}_L)\cdot\mathbf{r}} \quad (7.6)$$

where we have substituted back into Eq. (S11) of Ref. 31 their expression for $\bar{V}_S^\parallel(\mathbf{r})$ from their Eqs. (S8) and (S9). For the purpose of comparing this equation to Eq. (7.4), we have pulled out from the integrand the periodic part of the Bloch function, i.e. following Ref. 110, to form the u_{11}^2 prefactor. Additionally, we have employed the sign convention for misorientation from Ref. 110, so that the signs of \mathbf{Q} and ω in Eq. (7.6) are opposite those in Ref. 31. Now, comparing Eqs. (7.4) and (7.6), we note that the expression $g_\omega(\theta_L, \theta_R)$ in Eq. (7.4) is simply a generalization of the $u_{11}^2 e^{i(\theta_L - \theta_R + \omega)/2}$ terms in Eq. (7.6) (as shown in the latter part of the derivation in Ref. 31). With that, we find that Eqs. (7.4) and (7.6) produce identical results so long as we take $\Xi = \hbar^2 \kappa / 2m$. In terms of the scattering potential of Eq. (7.6), assumed as in Ref. 31 to be separable with $V_S(\mathbf{r}, z) = V_S(z) V_S^\parallel(\mathbf{r})$, this value of Ξ corresponds to $V_S(z) = \hbar^2 \kappa / 2md$ for the case of $V_S(z)$ assumed to be constant over the barrier region. Thus, if Eq. (7.6) is used for computing the tunnel current, then this specific magnitude of V_S must be employed (or, for a varying $V_S(z)$ across the barrier, some generalization of this magnitude could be obtained, again through the use of Eqs. (7.3) and (7.4)). With this specific value, the tunneling formalism of Ref. 31 is then seen to be identical to that of Ref. 110.

It should be noted that our comparison of Eqs. (7.3) and (7.4) with (7.5) and (7.6) is made on the assumption that the latter equations are being used to compute the total (or primary) tunnel current. Alternatively, if some secondary source of scattering in the system is assumed, then Eq. (7.5) can be applied more directly, with some arbitrary (assumed) value of the scattering potential. This distinction is emphasized by Duke [117], where he refers to the primary contribution as the “elastic coherent” one, computed using a matrix element like that of Eq. (7.3), and with any secondary contribution computed according to a matrix element like that of Eq. (7.5) (see, e.g. Eq. (18.38) of Ref. 117). In such a computation, however, the secondary current would be summed together with the primary one. Use of such a summation

is not discussed by Britnell et al. [31], and so we interpret their equation as indeed being intended for expressing the total tunnel current.

Despite the equivalence in the formalisms of Refs. 110 and 31, there are a number of differences in the implementation of their theories for producing numerical results. First, in Ref. 110 a specific model for the tunnel barrier was not considered beyond what would be appropriate for a vacuum barrier (i.e. isotropic band with effective mass of unity). In this respect the treatment of Ref. 31 for a specific barrier material (such as h-BN) is significantly better. In Section 7.3 we extend that sort of treatment, providing theoretical results for the energy dependence of the tunneling decay constant.

A second difference in implementation has to do with the specific means of evaluating the matrix elements. Consider the surface integral in Eqs. (7.4) and (7.6), normalized to the area A of the junction,

$$\frac{1}{A} \int dS e^{i\mathbf{Q}\cdot\mathbf{r}} e^{i\Delta\mathbf{k}\cdot\mathbf{r}} \quad (7.7)$$

where $\Delta\mathbf{k} = \mathbf{k}_R - \mathbf{k}_L$. In Ref. 110, this term is evaluated over a finite range, $-L/2$ to $+L/2$ for both x and y directions, which for zero misorientation leads to

$$\text{sinc}\left(\frac{L\Delta k_x}{2}\right) \text{sinc}\left(\frac{L\Delta k_y}{2}\right) \quad (7.8)$$

For the case of Ref. 31, this part of the matrix element is captured in their $\bar{V}_S^{\parallel}(\mathbf{q})$ term with $\mathbf{q} \equiv \Delta\mathbf{k}$, which similarly restricts the region over which the tunneling occurs in a laterally coherent manner. A quantity analogous to that in Eqs. (7.7) or (7.8) would be $\bar{V}_S^{\parallel}(\mathbf{q})/A$, which in Ref. 31 is modeled as

$$\frac{1}{A(q_c^2 + q^2)} \quad (7.9)$$

where q_c is some cut-off wavelength. If we compare the tunnel currents obtained using Eqs. (7.8) and (7.9), we find fairly good agreement in the dependence of the current on the parameters L and q_c , so long as we take $L = 2\pi q_c^{-1}$. However, regarding the absolute magnitude of the current, we find poor agreement between that obtained from Eqs. (7.8) and (7.9), even with the use of $\Xi = \hbar^2\kappa/2m$. This problem arises from the specific dependence of Eq. (7.9) on the area A of the device, which produces an incorrect dependence of the current on A (it should be noted that Eq. (7.9) was presented in Ref. 31 primarily as a proportionality, i.e. without focus on the absolute magnitude of the term). However, if we modify the form of Eq. (7.9) somewhat, we can obtain current that scales properly with A . In particular, we use

$$\frac{2\pi q_c^2}{\sqrt{A}(q_c^2 + q^2)^{3/2}} = \frac{1}{[1 + (q/q_c)^2]^{3/2}} \quad (7.10)$$

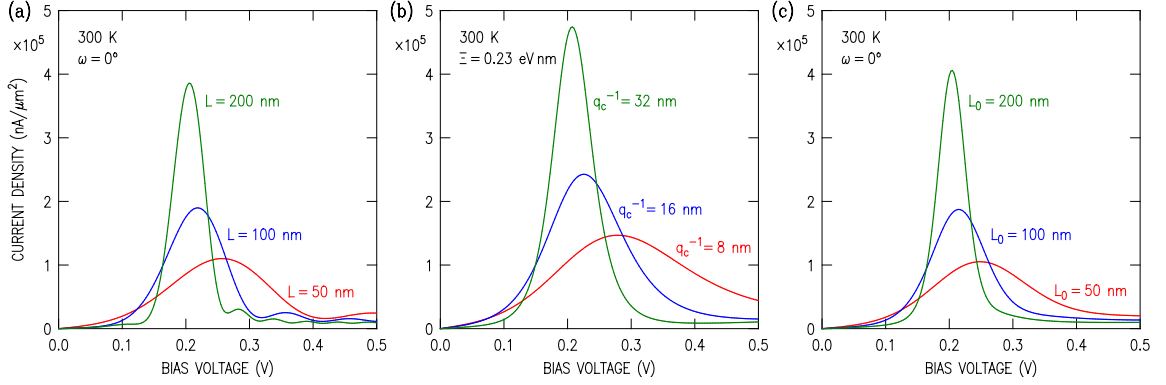


Figure 7.1: Comparison of theoretical tunneling currents as a function of the bias voltage across two graphene electrodes separated by a h-BN insulator using the theories of (a) Ref. 110 with zero misorientation, varying coherence length L ; (b) Ref. 31 with amplitude $\Xi = \hbar^2\kappa/2m$, varying $q_c = 2\pi/L$, and with the modified form of the scattering potential given in Eq. (7.10). In panel (c), we show the equivalence of the two theories by computing the total current of a device with a log-normal distribution of grain sizes with mean coherence length L_0 and variance $L_0^2/10$ with the current for each grain size computed using the theory of Ref. 110.

Equation (7.10) produces very similar results as Eq. (7.8) in terms of both the parameter-dependence and the absolute magnitude of the current, still considering zero misorientation.

The equivalence between the two theoretical treatments is illustrated in Fig. 7.1(a) and 7.1(b), showing a side-by-side comparison of tunneling currents computed using Eqs. (7.8) and (7.10), respectively, with related parameters $L = 2\pi q_c^{-1}$ and $\Xi = \hbar^2\kappa/2m$. Although the results are qualitatively similar, we consider Eq. (7.10) to be slightly preferable compared to Eq. (7.8) for evaluation of the current, since the latter employs sharp cut-offs for a single L -value in the x and y directions, which produce small oscillations in the current-voltage characteristic above the main resonant peak.[110] These oscillations are not present when Eq. (7.10) is employed, since that equation is applicable to a distribution of L -values, as is likely more appropriate for a physical device. We show this equivalence explicitly in Fig. 7.1(c), which is obtained by computing the total current density for a polycrystalline device with a log-normal distribution[120] of grain sizes (i.e. a distribution of coherence lengths). Including such a distribution of grains in a single device averages out secondary oscillations due to grain size effects but preserves the resonant peak structure and yields a tunneling characteristic similar to that of Eq. (7.10), shown in Fig. 7.1(b). Compared to a computation involving a distribution of grains and multiple calculations with Eq. (7.8), a straightforward computation using Eq. (7.10) appears to capture the relevant physics of a macroscopic device in a more compact form, and thus we use Eq. (7.10) in all subsequent calculations.

We conclude that the theories of Refs. 110 and 31, employing Eqs. (7.8) or (7.9), respectively, are actually modeling the same aspect of the tunneling process, namely, a restriction in the lateral extent over which the wavefunctions maintain their coherence. In Ref. 110 this was described in terms of a grain size in the graphene. In Ref. 31 this was described in terms of the “scattering potential” of Eq. (7.5), with specific form given by Eq. (7.9) (or with a small modification to that, as in Eq. (7.10)). Again, the effect of this “scattering potential” is to restrict the lateral area over which coherent tunneling occurs. However, in Ref. 31 it is argued that this restriction is not due to limited grain sizes in their devices, but rather, arises from other scattering mechanisms in the system.

Another significant difference between the theories of Refs. 110 and 31 is in the manner in which they deal with angular misorientation between the lattices of the graphene electrodes. For Ref. 31, it is assumed that there is no dependence on misorientation, with Eq. (7.9) being used in the computations where $\mathbf{q} = \Delta\mathbf{k}$ as defined following Eq. (7.7). That is to say, the factor $e^{i\mathbf{Q}\cdot\mathbf{r}}$ in Eq. (7.7) is incorporated in their definition of a modified scattering potential $\bar{V}_S^{\parallel}(\mathbf{r})$, so that the Fourier transform of that quantity, $\bar{V}_S^{\parallel}(\mathbf{q})$, can be modeled directly by Eq. (7.9) without any further explicit occurrence of the $e^{i\mathbf{Q}\cdot\mathbf{r}}$ term. This treatment thus makes a specific assumption about the scattering mechanism (although the specific physical mechanism is not identified).

In contrast, in Ref. 110 the misorientation is fully included, employing $\mathbf{Q} + \Delta\mathbf{k}$ in the argument of the combined exponentials of Eq. (7.7) where \mathbf{Q} is the misorientation vector. Similarly, writing Eq. (7.8) with inclusion of misorientation we would have $Q_x + \Delta k_x$ and $Q_y + \Delta k_y$ in the arguments of the sinc-functions, as evaluated in Ref. 110, rather than just Δk_x and Δk_y . For the present work in which we use the more general form given by Eq. (7.10), we also evaluate that with $|\mathbf{Q} + \mathbf{q}|$ in the argument rather than just q . This procedure is followed for all subsequent computational results in this work, so that using Eqs. (7.4) and (7.10) our matrix elements are computed as

$$M_{\alpha\beta} = \frac{\hbar^2\kappa}{2mD} e^{-\kappa d} \frac{g_{\omega}(\theta_L, \theta_R)}{[1 + (|\mathbf{Q} + \mathbf{q}|/q_c)^2]^{3/2}} \quad (7.11)$$

with $\mathbf{q} = \Delta\mathbf{k}$. The current is then given by Eq. (7.2).

Regarding the role of misorientation (as determined by \mathbf{Q}), we find that this is a large effect, consistent with the results of Ref. 110. In Ref. 31, misorientation is handled by absorbing the $e^{i\mathbf{Q}\cdot\mathbf{r}}$ from Eq. (7.7) into their definition of the scattering potential $\bar{V}_S^{\parallel}(\mathbf{q})$. We do not agree with their argument that the resulting current–voltage relationship will not show a significant dependence on misorientation. Certainly for small L (large q_c) misorientation is not so important, but we feel that in general the misorientation will play a large role in determining the current–voltage characteristic. We thus feel that it is best to leave this issue as an open question for the moment, hopefully to be addressed experimentally in future work.

Summarizing this comparison of the theories of Refs. 110 and 31, we find the following: (i) The two theories are formally equivalent, although we find that the Ξ parameter in the latter theory must have a value of $\hbar^2\kappa/2m$ (and also L is related to q_c by $L = 2\pi q_c^{-1}$). (ii) The scattering term in the latter theory is slightly modified here, as in Eq. (7.10). With that revision, numerical results from the two theories are in good agreement for the case of zero misorientation. (iii) For nonzero misorientation, we believe that the former theory provides the correct form for the tunneling current at least when finite grain sizes limit the lateral coherence of the tunneling. For other scattering mechanisms perhaps misorientation is not so important, as assumed in Ref. 31, although specific identification of such a mechanism remains to be done. Further work, both experimental and theoretical, is likely needed to evaluate the role of electrode misorientation in the tunneling.

7.3 Hexagonal boron nitride tunneling barrier

In the work of Britnell et al. [112], some specific details of a tunneling barrier consisting of hexagonal boron nitride (h-BN) were described. We extend those considerations here by considering the results of explicit computations of the h-BN band structure. In Fig. 7.2(a) we display the band structure of h-BN along various high symmetry directions, computed using density-functional theory with the Vienna Ab Initio Simulation Package (VASP). We use the Perdew-Burke-Ernzerhof (PBE)[57] parametrization of the generalized gradient approximation (GGA) for the electron exchange correlation potential. We use projector augmented wave potentials[56, 121] with a fixed energy cutoff of 400 eV (the default for N). The cell is fixed with experimental lattice constants in the calculations. The zero of energy in Fig. 7.2(a) is chosen to be coincident with the top of the valence band (VB); a band gap of 4.21 eV separating the VB and the conduction band (CB) is found in our density-functional computation, significantly less than the experimental value of 6.0 eV,[21] with this error occurring due to the well-known limitations of density-functional theory.

For tunneling, we require the band structure for complex values of the wavevector \mathbf{k} , as discussed in Ref. 112 by employing simple models for the band structure for real \mathbf{k} values and then analytically continuing those to imaginary \mathbf{k} values. The general behavior of such analytic continuation can be deduced from inspection of complex band structures for other materials,[122, 123] namely, that the curvature of bands reverses sign when crossing from real to imaginary \mathbf{k} across some critical point in the band structure, but with the magnitude of curvature (effective mass) being maintained. If the bands with real \mathbf{k} approach a critical point with a nonzero slope (as occurs when the Fourier component of the potential for that particular \mathbf{k} value is zero), then no continuation of the band into imaginary \mathbf{k} values occurs. Additionally, considering whether or not a band with imaginary \mathbf{k} value will serve to connect bands with purely real \mathbf{k} (i.e. connecting the VB and CB of h-BN), then the respective states for the two bands at the critical point must have nonzero overlap,[122] i.e. $\langle \Psi_i | \Psi_j \rangle \neq 0$

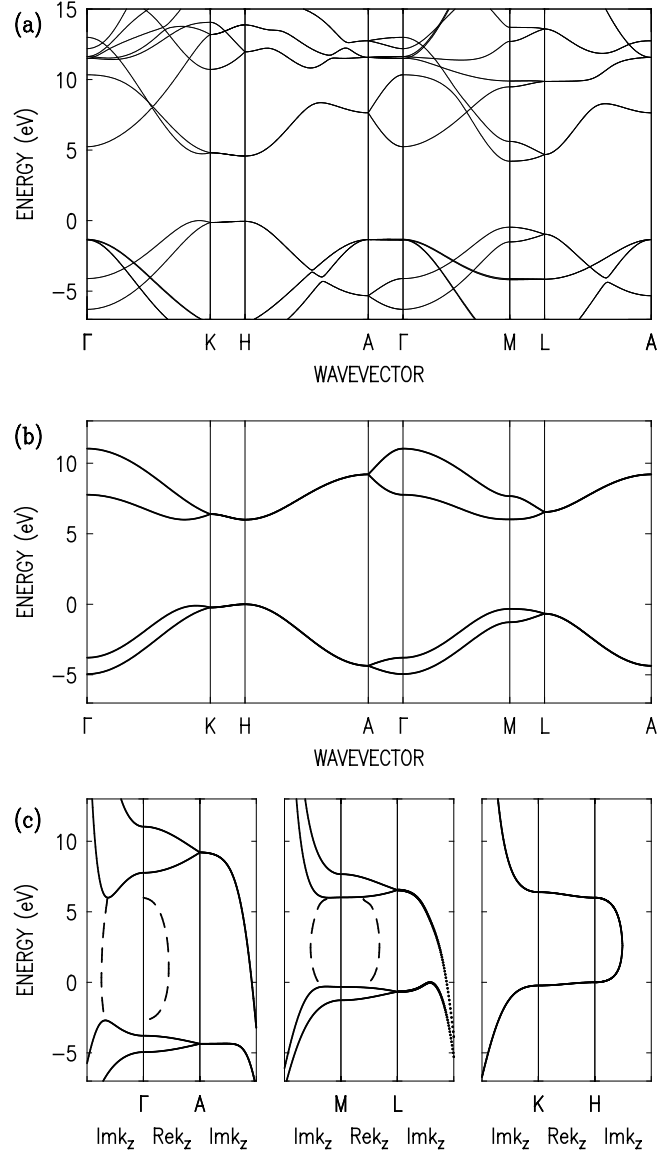


Figure 7.2: (a) Band structure of hexagonal boron nitride, computed with density-functional theory. (b) Band structure from a tight-binding model, including only p_z basis states. (c) Complex band structure from the tight-binding model, along the Γ A, ML, and KH directions. The right-hand and left-hand panels for each direction show the band structure with varying imaginary part of k_z . In these panels, solid lines denote bands for which $\text{Re}(k_z)$ is constant, equal to the value at the point where the right- or left-hand panel joins the center panel. Dashed lines indicate bands for which both $\text{Im}(k_z)$ and $\text{Re}(k_z)$ is varying, in accordance to the lines in the respective $\text{Im}(k_z)$ and $\text{Re}(k_z)$ panels. In the each panel where $\text{Im}(k_z)$ is varying, the range plotted is twice as large as in the corresponding panel showing $\text{Re}(k_z)$.

for a band with imaginary \mathbf{k} connecting states Ψ_i and Ψ_j .

To explicitly obtain the complex band structure for h-BN, we employ a tight-binding model with parameter values adjusted such that the bands approximately match those of the density-functional computation (except for the band gap, where the experimental value of 6.0 eV is matched).[21] Results are shown in Fig. 7.2(b), where we have used a model with only p_z -states on the B and N atoms as basis functions (on-site energies of 6.0 and -1.9 eV, respectively), and assuming both in-plane and out-of-plane nearest-neighbor B-N interactions (hopping energies of -1.6 and 0.6 eV, respectively) as well as a second-nearest-neighbor in-plane N-N interaction (-0.3 eV). Additionally, non-orthogonality between both in-plane and out-of-plane nearest-neighbor B-N p_z -orbitals is included (overlap matrix elements of 0.05 and 0.03, respectively). The method of solution for this problem with the non-orthogonal basis is described, for example, in Ref. 58. Our tight-binding results are similar to those of Robertson [124].

Comparing Figs. 7.2(a) and 7.2(b), we see that the states derived from the p_z -orbitals are quite clearly apparent in the density-functional results. Some mixing occurs with the other, sp^2 -derived states of the system, with the mixing being strongest in the conduction band. However, for our purposes of evaluating the tunneling of states with large in-plane momentum (near the K or M points), then we note in particular that along the KH and ML directions the tight-binding description of the system using only the p_z -orbitals works quite well since the sp^2 -derived states are separated from the VB and CB edges by about 5 eV. In terms of quantitative agreement between the tight-binding and density-functional results, the former overestimates the band widths for the p_z -states along KH (these bands are very flat in the density-functional results) and it underestimates the band widths for the Γ A direction. Along ML, the band widths for the tight-binding and density-functional results are reasonably close, within 15%, and those values are also in fairly good agreement with many-body computational results.[125]

From the tight-binding model we can obtain the complex band structure, shown in Fig. 7.2(c). Those plots are displayed with the same format as Ref. 122. For example, on the far right-hand side of the plot along the KH direction, in the panel with varying $\text{Im}(k_z)$, there is a loop connecting the VB maximum and CB minimum. This loop is shown by a solid line, indicating that the $\text{Re}(k_z)$ value for these states is constant, i.e. it has a value corresponding to the H-point, $\text{Re}(k_z) = \pi/c$, where c is the lattice constant of 6.66 \AA . For states with energies within the band gap having lateral wavevector corresponding to the K-point, then they will decay in the h-BN with decay constant of $\kappa \equiv \text{Im}(k_z)$ according to the values shown by this loop shown on the far right of Fig. 7.2(c). The wavefunctions of these states will, at the same time, have a spatial oscillation given by $\text{Re}(k_z) = \pi/c$. This result of a combined exponential decay plus oscillation is a basic feature of the h-BN eigenstates in the $[0001]$ direction through the material (states that have exponential decay without any oscillation are not eigenstates of the system).

Turning to the ML and Γ A directions shown in Fig. 7.2(c), the situation is more complicated. The dashed lines seen there in the $\text{Re}(k_z)$ and $\text{Im}(k_z)$ panels indicate eigenstates for which both $\text{Re}(k_z)$ and $\text{Im}(k_z)$ are varying as a function of energy.[122] Focusing on the results in the ML direction, we find a maximum value of $\kappa \equiv \text{Im}(k_z) = 5.2 \text{ nm}^{-1}$ for the (dashed) loop connecting the VB and CB states, at an energy in the middle of the band gap. For the KH direction, at midgap we find a κ value of 4.6 nm^{-1} , although as discussed above our tight-binding KH bands show too much dispersion; flatter bands are expected to considerably increase this estimated κ value. Averaging over angles, we estimate a midgap κ value of $\gtrsim 5.0 \text{ nm}^{-1}$. An improved treatment of the complex band structure will provide a better estimate of this value, as well as possibly producing a significant dependence of κ on the angle between the graphene and h-BN lattice.

Regarding the energy dependence of κ , we have found in Fig. 7.2(c) that we have loops connecting the VB and CB. In the absence of a loop, it is usual to model the energy dependence as being parabolic with the energy ΔE to a band edge, $\kappa = \sqrt{2m^*\Delta E}/\hbar$ with some effective mass m^* . [31, 110] Now, including the loop, we use this same formula for κ but with an interpolation formula for an *effective* barrier height ΔE ,

$$\Delta E = \frac{(E_C - E)(E - E_V)}{(E_C - E_V)} \quad (7.12)$$

where E_V is the energy of the VB maximum, E_C is the energy of the CB minimum, and E is the energy of a state within the band gap. For a midgap κ value of κ_0 , the effective mass is given by $m^* = 2\hbar^2\kappa_0^2/(E_C - E_V)$.

An experimental value for the tunneling decay constant is available from a prior work of Britnell et al. [126]; computing the slope of their measured tunneling resistance (on a logarithmic scale) as a function of number of BN layers, we find a decay constant of 6.0 nm^{-1} . The relationship of this value to the midgap κ_0 value depends on the offset between the boron nitride VB and the Dirac point of the graphene. Britnell et al. [112] have used an offset of 1.5 eV (i.e. one quarter of the way up the band gap), [127] and as discussed in Section 7.4, they have argued that this value accounts for an observed asymmetry in their device characteristics. As also discussed there, from comparison of theory to experiment for other devices we derive an offset value closer to the middle of the band gap.[2] In any case, in order to be definite as to our choice of decay constant to use in our simulations, we take the experimental value of 6.0 nm^{-1} and we assign that to the midgap κ_0 value. This experimental value is slightly greater than that derived from the tight-binding model discussed above, but still in reasonable agreement considering the uncertainties of the theory. The κ_0 value of 6.0 nm^{-1} corresponds to an effective mass of 0.9 times the free-electron mass.

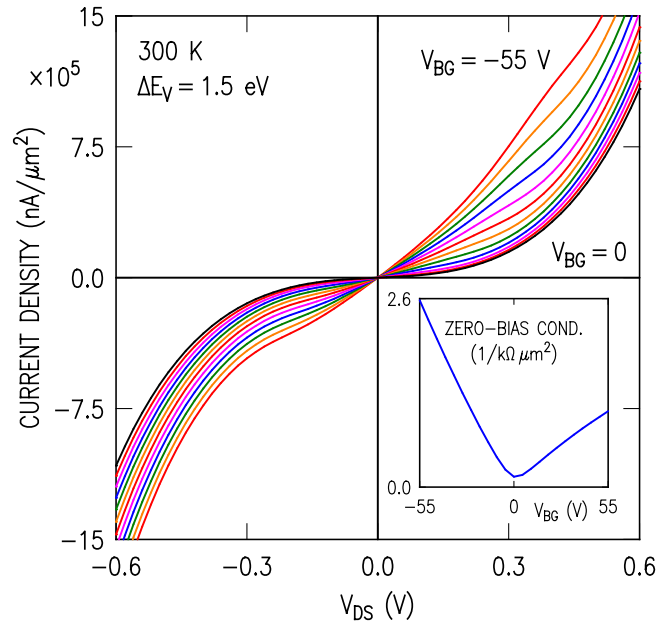


Figure 7.3: Theoretical simulation of a GIG device with a back gate, corresponding to Fig. 4 of Ref. 128. The simulated structure consists of the top layer of graphene, 4 layers of h-BN, the bottom layer of graphene, and 20 nm of h-BN on a silicon substrate (back gate) with a 300 nm SiO₂ dielectric film. Both graphene layers are assumed to be undoped. Curves are shown for $V_{BG} = -55$ to 0 V in 5 V increments. Zero-bias conductance versus gate voltage is shown in the inset. The valence band offset that best fits with the experimental data is found to be $\Delta E_V = 1.5$ eV.

7.4 Comparison to experiment

In this section, we display various simulated results for the GIG current–voltage characteristics, selected to provide comparison to experimental results published elsewhere.[31] The device structures that we consider include either a single gate on the bottom of the device, or both top and bottom gates sandwiching the main GIG structure. Voltages on the gates are denoted V_{BG} and V_{TG} for the bottom and top, respectively. We denote the two graphene electrodes as the source and drain, with the drain being the electrode closest to the top gate and the source closest to the bottom gate. Voltages on the electrodes are denoted V_S and V_D for the source and drain, respectively. We consider the current into the drain, I_D , as a function of $V_{DS} \equiv V_D - V_S$. Gate voltages are similarly referenced to the source voltage. In all subsequent simulations we use the two-sided tunneling barrier described by Eq. (7.12). We calculate carrier densities in the graphene electrodes using the temperature-dependent integrals given in Eq. (27) of Ref. 110, in contrast to the zero-temperature approximation employed in the computational results of our previous work.[2, 110, 111]

We first consider results obtained on devices that do not display NDR in their

characteristics, presumably due to a relatively small coherence length for the tunneling. In Fig. 7.3, we display computed characteristics for a device whose structure (tunneling barrier thickness and gate dielectric thickness) is identical to that employed by Ponomarenko et al., Fig. 4 of Ref. 128. This device did not display any NDR, and thus we simulate the characteristics with a coherence length of $L \rightarrow 0$ (that is, employing Eq. (7.1) and correcting the magnitude of the current according to the discussion following Eq. (A.2)). Our computed curve for zero gate voltage is essentially identical with that of Ponomarenko et al., and in Fig. 7.3 we display curves for various other gate voltages as well. Regarding the dependence of the zero-bias conductance on gate voltage, Ponomarenko et al. observed distinct asymmetry with respect to the polarity of the gate voltage, and from that they concluded that the valence band offset between the h-BN and graphene was approximately 1.5 eV. Our computation of this gate voltage dependence, shown in the inset of Fig. 7.3, agrees qualitatively with those of Ref. 128, though our simulation uses the modified form of the energy dependence of κ as given by Eq. (7.12) and the temperature-dependent carrier densities mentioned in the previous paragraph (whereas Ponomarenko et al. appear to use the zero-temperature form of the carrier densities).

In Fig. 7.4 we display computed characteristics for a device whose structure is identical to that employed by Roy et al., Fig. 5 of Ref. 2. Again, this device did not display any NDR and we simulate it in the limit of $L \rightarrow 0$. We see a sloping feature in the curves near $V_{DS} \approx 0.25$ V, which corresponds to the Fermi level in the top graphene electrode passing through the vanishing density-of-states at the Dirac point. There are generally two such features in a given current–voltage curve; one for each electrode as the Fermi level passes through the Dirac point of that electrode. The sloping feature described here is due to the same phenomena as the plateau feature described in Ref. 2, though it is less distinct due to the broadening effect of finite temperature. Our computed zero-bias conductance versus gate voltage curve is shown in the inset of Fig. 7.4. In this case, we find agreement between experiment and theory for a valence band offset of 3 eV (solid curve), i.e. with the graphene Dirac point closer to the middle of the h-BN band gap. If we use an offset of 1.5 eV as in Fig. 7.3, we obtain the curve shown by the dashed line in the inset of Fig. 7.4, which does not compare well to the experiment. This difference between the offsets obtained for the devices of Figs. 7.3 and 7.4 is not understood at present, although measurements for additional device structures will hopefully serve to clarify this situation.

Considering the lack of NDR observed in the devices associated with Figs. 7.3 and 7.4, we have so far allowed the coherence length to serve as a free parameter in the simulations and made no claims as to the source of wavefunction decoherence. For the latter device, however, we do have additional evidence which suggests that disorder in the graphene due to processing steps leads to a vanishing coherence length. Using Raman spectroscopy, it is possible to identify materials by measuring the amplitude of inelastically scattered light as a function of energy shift (typically reported in units of inverse wavelength). The position and relative amplitudes of peaks measured in these

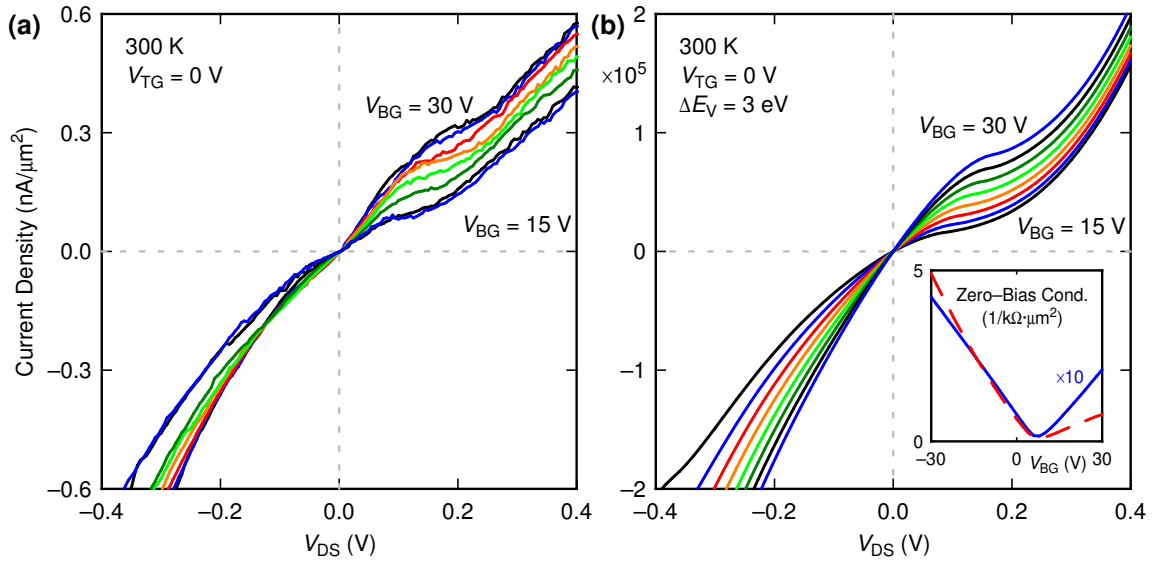


Figure 7.4: (a) Measured current–voltage characteristic from a GIG device fabricated with CVD graphene and h-BN. Structure consists of a top gate, 10 nm of a HfO_2 gate dielectric, the top layer of graphene, 4 layers of h-BN, and the bottom layer of graphene on a doped silicon substrate (back gate) with a 90 nm SiO_2 dielectric film. (b) Theoretical simulation of this GIG device, without momentum conservation, with top and bottom gates (denoted V_{TG} and V_{BG}). Both graphene layers are p -type doped with a carrier density of $p = 7.4 \times 10^{11} \text{ cm}^{-2}$ in each layer. Curves are shown for $V_{BG} = 15$ to 30 V in 1.5 V increments. Zero-bias conductance versus back gate voltage is shown in the inset for a valence band offset of 3 eV (solid) and 1.5 eV (dashed). The best agreement with experiment (shown in main panel) is obtained for a valence band offset at midgap, $\Delta E = 3 \text{ eV}$.

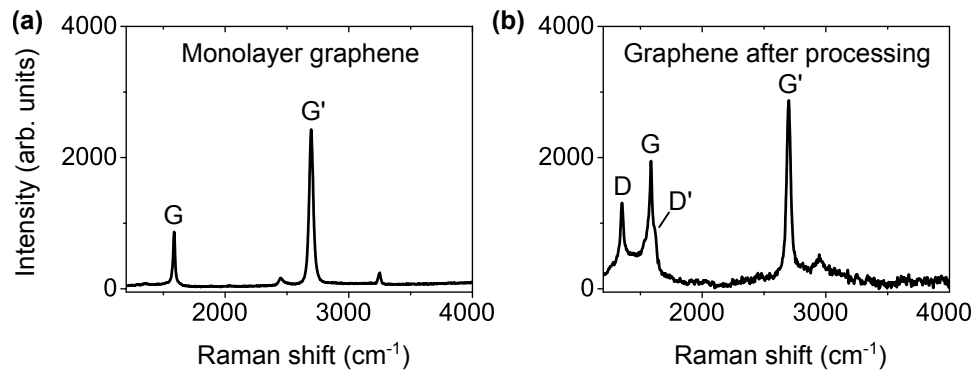


Figure 7.5: (a) Raman spectrum obtained from monolayer graphene after transfer to the SiO_2 substrate showing characteristic G and G' peaks of graphene. (b) Spectrum of graphene after transfer of h-BN to make device discussed in Fig. 7.4, showing enhanced D and D' peaks due to disorder introduced in processing.

spectra are characteristic of the vibrational modes present in the sample, and thus serve as a fingerprint for the constituent materials. For instance, the sp^2 network of carbon bonds in graphene and bulk graphite yields a doubly-degenerate zone-center E_{2g} mode (using the Mulliken symbol E_{2g} to represent the point group symmetry of this mode, as is convention in Raman spectroscopy), leading to a Raman peak at $\approx 1580 \text{ cm}^{-1}$, the so-called G -peak.[129–131] In the presence of disorder, intervalley elastic scattering from a defect site followed by inelastic scattering with a phonon leads to a peak at $\approx 1360 \text{ cm}^{-1}$, the D -peak of disordered graphene and graphite. This is a second-order effect involving two scattering events, but nonetheless provides clear evidence of the presence of defects (and boundaries) in a graphene lattice. An additional second-order peak emerges around 2700 cm^{-1} (depending on excitation wavelength) due to two-phonon scattering, often called the $2D$ -peak since the relevant phonons come from the zone-edge, as in the D -peak. However, this transition does not involve defect scattering and therefore is always present in graphitic-carbon materials, and thus we refer to this peak as the G' -peak here to emphasize its association with defect-free scattering in graphene.

Raman spectra from the graphene used to fabricate the CVD-based device from Ref. 2 are shown in Fig. 7.5, measured before and after several processes steps and transfer of the h-BN. After processing steps, including Ti deposition, removal, and h-BN transfer, the graphene Raman spectrum shows a clear D -peak that was not present before. In addition, there is a shoulder feature to the right of the G -peak in Fig. 7.5(b) which is similarly associated with disorder in the graphene; the D' -peak, resulting from a second-order *intravalley* scattering process.[131] This feature in particular, present after processing along with the D -peak, helps to distinguish the D -peak from what could otherwise be interpreted as the E_{2g} mode of h-BN, which is typically peaked near $\approx 1370 \text{ cm}^{-1}$. [132–134] The emergence of strong D and D' signatures in Fig. 7.5(b) suggest that processing introduced defects which degraded the graphene and thus reduced the lateral wavefunction coherence, ultimately causing a lack of resonance and NDR in the tunneling current.

Let us now turn to devices that do display NDR in their characteristics, indicative of larger coherence lengths. Figure 7.6 shows simulated results for the device structure of Britnell et al., Fig. 1 of Ref. 31. This device has essentially the same structure as the device in Ref. 128, yet exhibits clear NDR for a similar range of gate voltages. Our simulations of this device in Figs. 7.6(b)–7.6(d) use a lateral coherence length of 75 nm and a valence band offset of 1.5 eV (although the results were not sensitive to the precise value of the offset). Fig. 7.6(b) shows the result of our theory for zero misorientation angle between the graphene and the h-BN lattices. The resonant peak behavior is in good agreement with the experiment; they are also very close to the simulation results of Britnell et al., since, as argued in Section 7.2, our theory and their theory are essentially equivalent for the case of zero misorientation angle. Shown in Figs. 7.6(c) and 7.6(d) are results for other possible values of the misorientation. We see that a relatively small misorientation angle changes the tunneling current

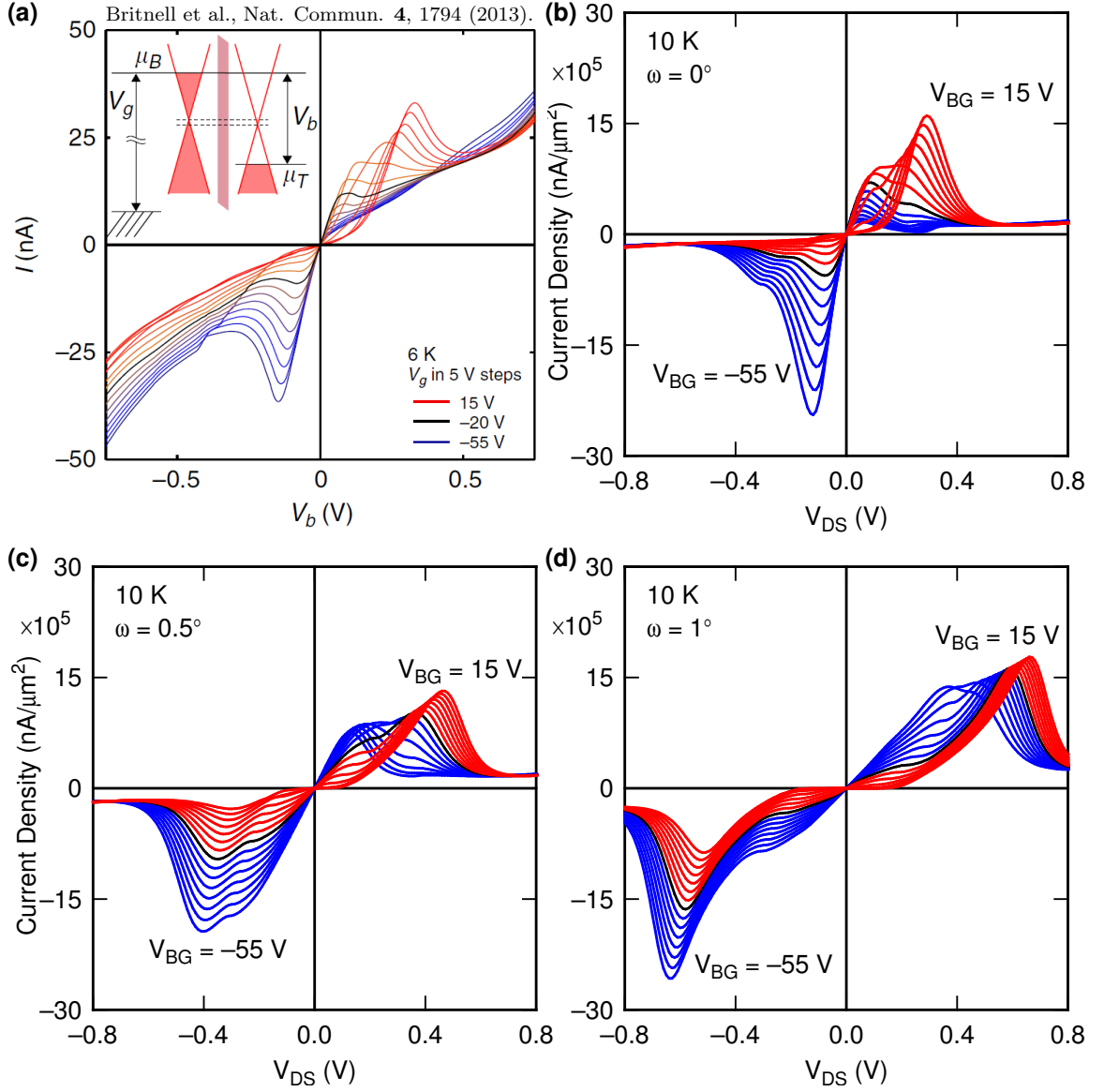


Figure 7.6: (a) Measured tunneling characteristics for gated GIG device, adapted from Ref. 31. (b)–(c) Simulations of resonant tunneling using a geometry corresponding to Fig. 1 of Ref. 31, reproduced in panel (a) for comparison. Tunneling characteristics are shown for (b) zero misorientation, (c) 0.5° of misorientation, and (d) 1.0° of misorientation between the graphene sheets. Curves are shown for $V_{BG} = -55$ to 15 V in 5 V increments. Computations are performed at low temperature to match with experiment. The device structure is identical to that of Fig. 7.3, with doping in the top and bottom layers of graphene set to $p = 1.0 \times 10^{12} \text{ cm}^{-2}$ and $n = 4.4 \times 10^{11} \text{ cm}^{-2}$, respectively.

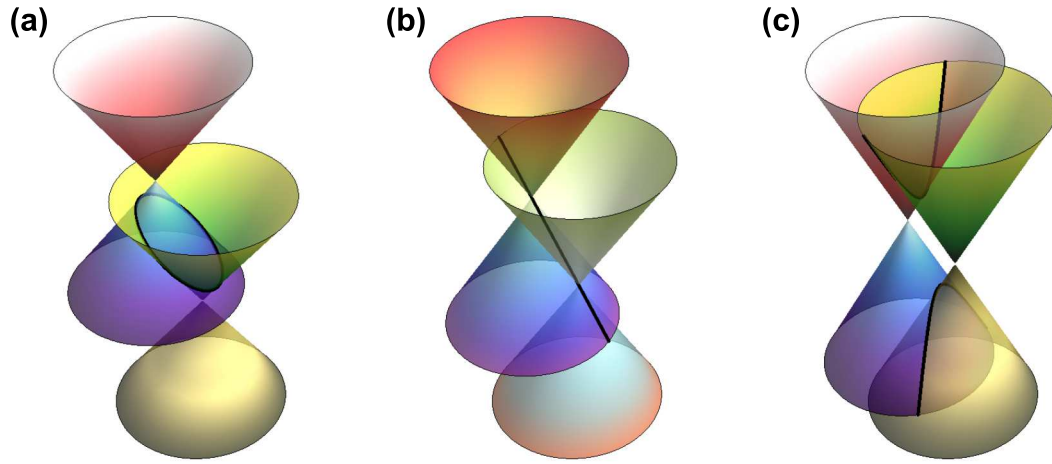


Figure 7.7: (a) Intersection of graphene bands from two electrodes with nonzero misorientation, at a bias voltage between the two resonant conditions, showing an elliptical set of states (bold) which conserve both energy and momentum simultaneously. (b) Intersecting states for a bias near resonance, extending through the conduction and valence bands of both electrodes, leading to a large number of allowed tunneling states. There will be a second, similar set of intersection states at close to opposite bias, resulting in a second resonant tunneling peak. (c) Intersecting states at a bias beyond the region of resonance, with disallowed tunneling for a band of states between the extrema of the hyperbolic intersections.

characteristics significantly, shifting the resonant peaks out to larger bias voltages, as well as flattening out the currents at low bias. This shift in voltage is caused by the addition of the misorientation vector \mathbf{Q} to the momentum conservation condition, which pushes the resonance condition out to higher voltages.[110] For certain doping situations (with nonzero misorientation), there is one positive and one negative peak in the tunneling characteristic due to the symmetry between the conduction and valence bands in graphene near the Dirac point. The conditions for energy and momentum conservation of tunneling states with nonzero misorientation are more complicated than for the oriented case, with situations such as those shown schematically in Fig. 7.7, leading to two resonant peaks at nearly opposite voltages. We see such a peak develop for both signs of V_{DS} in Fig. 7.6(d) (with a misorientation angle of 1.0°) over a wide range of gate voltages. Recently, this dual-peak phenomenon has indeed been observed and reported by Mishchenko et al. [32] in devices with finite misorientation.

The overall scale of our computed currents shown in Fig. 7.6 is significantly larger than what has been observed experimentally, despite the fact that the simulation parameters are partially derived from the measured value of $\kappa = 6.0 \text{ nm}^{-1}$, as discussed in Section 7.3. In addition, neither our theory, nor the theory of Britnell et al. can account for the apparent linear background current observed in the devices with NDR, as seen in Fig. 1 of Ref. 31. One way to produce a linear background current in the simulation is to average over all angles, as in Fig. 7 of Ref. 110, however a range of misorientation angles does not appear to be consistent with this experimental device. Further work is needed in order to resolve these discrepancies between the theoretical and the experimental current–voltage characteristics.

7.5 Summary

In summary, we have investigated a number of theoretical issues relating to GIG tunnel junctions. Conservation of lateral momentum in such devices leads to nonlinear current–voltage characteristics of the junction, with a resonant peak occurring when the Dirac points of the graphene electrodes are aligned.[110] Addition of gate electrode(s) can then produce transistor-type behavior of the devices.[111] Theories describing the characteristics of the devices have been previously presented in Refs. 110 and 31. Despite the seemingly different derivations used for the two theories, we have demonstrated here that they are actually equivalent. In both cases, a limitation of the lateral coherence length leads to broadening of the resonant peak. However, an important distinction between the two theories is in the manner in which misorientation of the graphene electrodes is treated; it is fully included within the theory of Ref. 110 in which the limitation of lateral momentum is assumed to arise through some limited area over which the tunneling occurs, whereas it has no significant effect in the theory of Ref. 31 since the misorientation is folded into the “scattering potential” of the problem. The theoretical work of Brey [135] fully includes misorientation

effects in the same manner as in Ref. 110.

Experimental results for GIG junctions have been reported,[2, 31, 112] some of which apparently display little or no momentum conservation, i.e. no resonant peak, and others of which do display a resonant peak. In the former case the results can be simulated with a simple formula involving only the density-of-states of the electrodes.[112] We have used that formula here for simulating recent experimental data[2] and we have also argued how the absolute magnitude of the current in this type of computation can be determined. For data in which a resonant peak is observed, we investigate the possible effect of electrode misorientation on the results. At least for the data reported thus far, we find that the best comparison with simulation occurs for zero misorientation angle, a conclusion which is apparently consistent with the theory of Ref. 31 since it explicitly neglects the role of misorientation. The reason for this lack of dependence on misorientation angle is not clear at present.

Separately, we have investigated the complex band structure of the h-BN tunneling barrier material. The values of the tunnel decay constant κ show dependence on the misorientation angle between the graphene and the h-BN. A quantitative result for this dependence is not available at present, but it is important to note that even a relatively small variation in κ can lead to a large variation in the transmission term $e^{-2\kappa d}$. Thus, it is possible that the tunneling will be strongly confined to a narrow angular range of lateral wavevectors in the h-BN. To achieve those particular wavevectors in the h-BN, phonon scattering (or phonon-assisted tunneling) of the graphene states may play an important role. The presence of a linear background current in the measured characteristics, much greater than what is obtained in the simulated current as discussed at the end of Section 7.4, possibly provides evidence of such phonon participation in the tunneling process.

Chapter 8

Tunneling between bilayers of graphene

In this chapter, a theory is developed for calculating vertical tunneling current between two sheets of bilayer graphene separated by a thin, insulating layer of hexagonal boron nitride, neglecting many-body effects. Results are presented using physical parameters that enable comparison of the theory with recently reported experimental results. The observed resonant tunneling and negative differential resistance in the current–voltage characteristics are explained in terms of the electrostatically-induced band gap, gate voltage modulation, density of states near the band edge, and resonances with the upper sub-band. These observations are compared to ones from similar heterostructures formed with monolayer graphene. The work described in this chapter appears in published form in Ref. 3.

8.1 Introduction

In contrast to the well-known linear dispersion of monolayer graphene (MLG), charge carriers near the six corners of the Brillouin zone in an isolated graphene *bilayer* are described by a quadratic energy dispersion.[136, 137] An even more intriguing distinction with MLG is that, under the influence of external fields, the band structure of bilayer graphene (BLG) near the charge neutrality point becomes quartic, changing from semi-metallic to semiconducting as a small band gap is induced.[138–140] This tunability of the band gap can be exploited by introducing gates, doping, and interactions with substrate materials in electronic devices based on BLG.[141–143] In this paper, we consider these effects and others in a 2D to 2D resonant tunneling device composed of two sheets of BLG separated by a thin, insulating layer of hexagonal boron nitride (h-BN). In a vertical configuration with an interlayer bias, tunneling between two-dimensional electron gases is constrained by simultaneous energy and momentum conservation, leading to resonances in the current–voltage (I – V) characteristic and thus regions of negative differential resistance (NDR).[33] Such devices

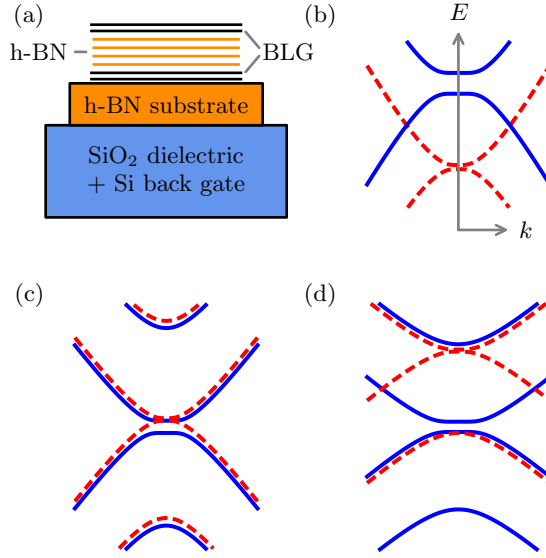


Figure 8.1: (a) Device structure, with double black lines indicating each graphene bilayer (BLG) and the group of orange lines representing 4 to 6 layers of h-BN. (b) Alignment of electronic bands at an off-resonant interlayer bias voltage; blue (solid) curves for one bilayer and red (dashed) for the other; (c) at the voltage which yields the primary tunneling resonance; (d) at a higher voltage which aligns the lower bands of one bilayer with the higher sub-bands of the other. The largest contribution to tunneling current occurs near the states where the two bands intersect. Bands represent energy as a function of in-plane crystal momentum near one of the six corners of the Brillouin zone.

were originally proposed for conventional 2D quantum wells,[26] but the theory was recently treated for MLG,[1, 31, 110, 111, 115, 116, 135, 144] and NDR was observed experimentally in high-quality devices shortly thereafter.[31–33] The theory discussed in the present work is particularly relevant to the recent observations of Fallahzad et al.[33]

8.2 Tunneling mechanism

For a given interlayer voltage and for bilayers that are in crystallographic alignment, the electronic bands of the top and bottom bilayer of graphene will overlap for particular sets of states with equal energy and crystal momentum (Fig. 8.1). Away from the resonance voltage, only the states near the intersecting ring(s) can contribute to the tunneling current (Fig. 8.1(b)). However, for one particular voltage, the electrostatic potential between the bands will be zero, allowing all states between the two Fermi levels to tunnel simultaneously (Fig. 8.1(c)). The shape and position of the resulting

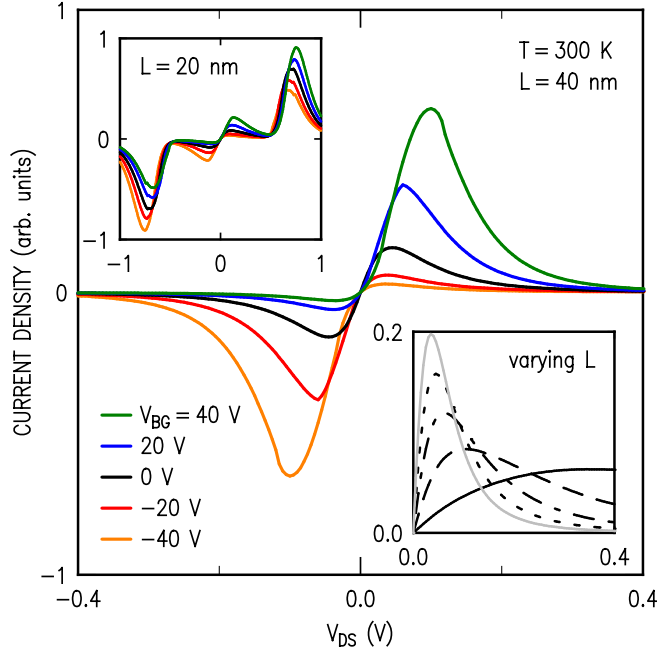


Figure 8.2: Calculated tunnel current density versus interlayer bias between undoped graphene bilayers for a range of gate voltages. Upper inset: a similar computation for a larger voltage range highlighting secondary resonances from the higher sub-bands. Lower inset: a closer view of the $V_{BG} = 0$ case, varying coherence length, a disorder parameter in the theory, from 50 nm (solid, light) to 10 nm (solid, dark).

resonant peak in the I - V characteristic depends on the quantity and sign of charge carriers in each bilayer, and therefore indirectly on external fields (gate voltages) and the electrostatic doping conditions.

For example, in the absence of strong doping or substrate interactions, resonance can be observed for both both positive and negative bias voltages as the back-gate voltage (V_{BG}) is swept from one sign to the other (Fig. 8.2). Recently, Fallahzad et al. have observed resonances with precisely this behavior in devices fabricated with exfoliated BLG/h-BN/BLG on a h-BN/SiO₂ substrate.[33] The width and amplitude of each resonant peak relative to the background (non-resonant) current are determined by the degree of coherence between tunneling wavefunctions, as is discussed in detail in Ref. 1.

In addition to the primary resonance, the higher sub-band of one bilayer can also come into alignment with the lower sub-band of the second bilayer causing a similar spike in the tunneling current. Secondary resonances as well as an increase in background current from the upper bands entering the tunneling energy window can be observed at larger voltages as shown in the upper inset of Fig. 8.2. Interactions with the upper sub-bands are distinct from monolayer devices, and may provide opportunities for multi-state logic devices.

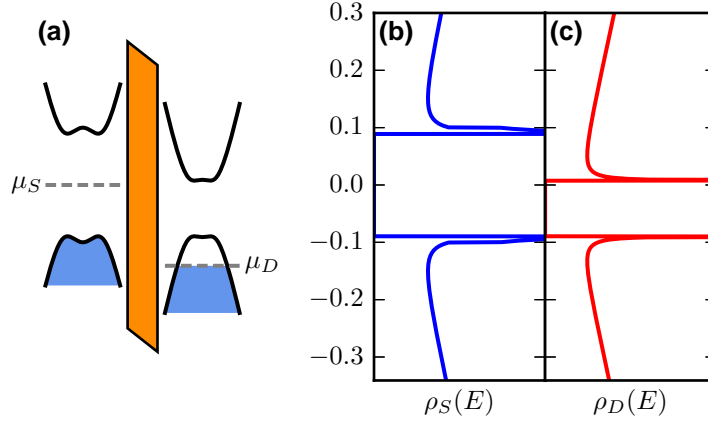


Figure 8.3: (a) Electronic bands in the source (left) and drain (right) electrodes with the tunneling barrier (band gap of boron nitride) in between at a small positive bias. Dashed lines indicate the Fermi levels in each bilayer, $\mu_i = -eV_i$; not to scale. Density of states corresponding to (b) the source electrode and (c) the drain electrode in the same bias condition as panel (a); energy axes in units of eV. The alignment of the divergences in the density of states near the valence band edge of each bilayer produces a large overlap of states and thus a spike in tunneling current.

At a smaller voltage scale, and especially at lower temperatures, it is possible to observe additional features due to the tunable band gap in BLG. The presence of a transverse electric field across a graphene bilayer induces a potential difference between the two individual layers of graphene. This broken layer symmetry causes a small band gap to open up around the charge neutrality point which increases with the magnitude of the potential difference across the bilayer. In the tunneling device modeled here, the interlayer and gate voltages modulate the separate potential difference across each individual bilayer in a coupled system.[143] As a result, the band gaps in both bilayers vary with voltage (typically at different rates), which affects the overall tunneling current. For non-zero band gap, the precise form of the energy dispersion is quartic near the gap, as in Figs. 8.1 and 8.3(a). Moreover, the location of the band gap is a ring of states concentric with the K -point. This arrangement of states causes divergences in the DOS at the conduction and valence band edges, which can yield additional spikes in the tunneling current for certain electrostatic arrangements. Whereas the primary feature in the tunneling current occurs when the electrostatic potentials in the source ϕ_S and drain ϕ_D electrodes are aligned, $\Delta\phi = \phi_S - \phi_D = 0$, other features due to overlap of the large DOS near the band edges can occur when one of the four conditions $\Delta\phi \pm E_{g,S}/2 \pm E_{g,D}/2 = 0$ is satisfied (where $E_{g,i}$ is the band gap in each bilayer), as in Figs. 8.3 and 8.4. These features in the I - V characteristic are distinct from those caused directly by momentum-conserving effects with complete band alignment (as in Fig. 8.1) and are less sensitive to the relaxation of momentum conservation (decoherence), but may

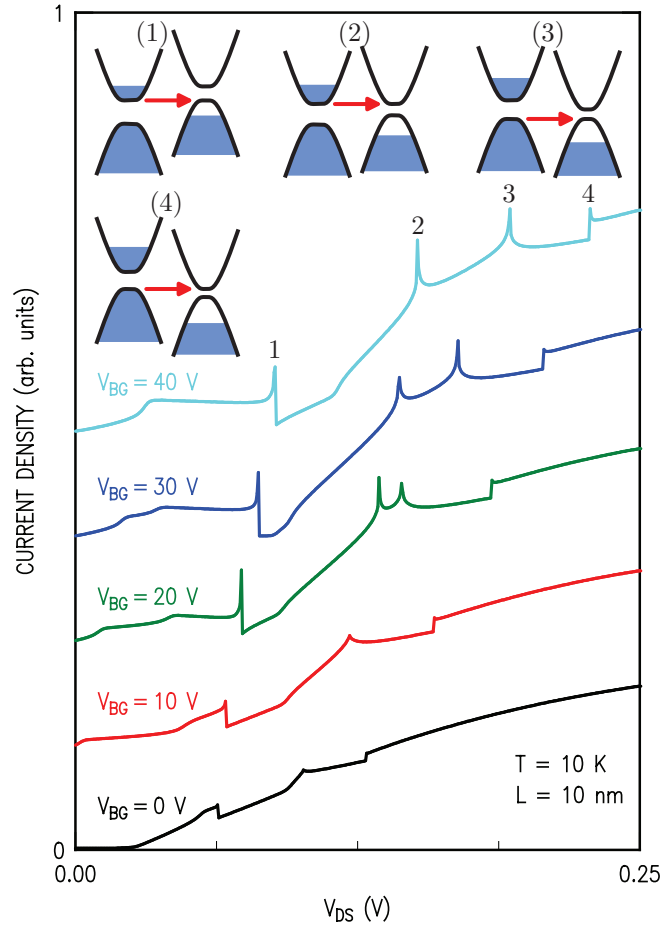


Figure 8.4: Low-voltage tunneling current for a device with a small amount of doping on the top (drain) bilayer at 10 K showing a number of small features due to the alignment of various band-edges, as explained in Fig. 8.3. I - V curves are shifted vertically for clarity. Numbered insets show the band alignment for each of the four labeled points along the $V_{BG} = 40$ V curve. Arrows indicate electron current that produces the sharp feature in each case.

be observed in tandem with the latter. In MLG there are no equivalent band edges, and thus these additional sharp features are absent in monolayer vertical tunneling devices.

8.3 Theoretical formalism

We use a tight-binding model for the dispersion of BLG with nearest-neighbor hopping energy $\gamma_0 \approx 3.1$ eV, interlayer hopping energy $\gamma_1 \approx 0.4$ eV, and interlayer potential asymmetry U .^[96] Higher order considerations such as the trigonal warping of the bands (azimuthal asymmetry) were found to have a negligible impact on the tunneling and thus were excluded. The occupation of levels and band gap in each electrode varies with the set of applied voltages, and thus the electrostatic potentials are required to calculate the tunneling current. These potentials are determined by first solving a matrix equation $q_i = C_{ij}V_j$, treating each monolayer of graphene separately, to obtain the transverse fields across each bilayer. We then use those fields to solve a second matrix equation treating each bilayer with the local DOS for each layer within the bilayers, as discussed in greater detail in Section 6.3.2. This method can accommodate both top and bottom gates, though we chose to focus on matching with devices with only one gate in the present work. Net charges are calculated using full Fermi integrals $q_i = e [(n_i - p_i) - N_i]$, $n_i = e \int dE \rho(E) f(E)$ to account for quantum capacitance and thermal occupation, with environmental doping density N_i . We calculate the tunneling current by summing over the transition rates between all states in the source and drain bilayers,

$$I = g_s g_v \frac{2\pi e}{\hbar} \sum_{\alpha, \beta} |M_{\alpha\beta}|^2 [f_S(E_\alpha) - f_D(E_\beta)] \delta(E_\alpha - E_\beta), \quad (8.1)$$

with spin and valley degeneracies g_s , g_v and state labels α and β in the source and drain bilayers.^[110] The overlap integrals between states in the source and drain are contained in the matrix element

$$M_{\alpha\beta} = \frac{\hbar^2}{2m} \int dS \left(\Psi_\alpha^* \frac{d\Psi_\beta}{dz} - \Psi_\beta \frac{d\Psi_\alpha^*}{dz} \right), \quad (8.2)$$

which is evaluated in a similar way as for MLG in Refs. 110 and 1. We calculate the surface integral in Eq. (8.2) over a region defined by the length scale of wavefunction coherence in the device, a parameter we call the characteristic coherence length, L . This is a disorder parameter which defines the degree of momentum conservation and thus controls the width and amplitude of resonant features in the I - V characteristic. The momentum (wavevector) conservation, chiral (angular) terms, and crystallographic misorientation are encapsulated in the matrix elements, while energy conservation is contained in the δ -function that appears in Eq. (8.1).^[1, 110]

In contrast to the theory for MLG devices, for BLG this δ -function must be evaluated using the quartic dispersion relation in order to capture band-gap and higher sub-band effects. Converting the sums over states in Eq. (8.1) to integrals over k , we can evaluate the δ -function by changing variables from E to k ,

$$\delta[E(\mathbf{k}_S) - E(\mathbf{k}_D) + \Delta\phi] \rightarrow \sum_i \frac{\delta(k - k_i)}{|f'(k_i)|} \quad (8.3)$$

for all combinations of bands between each bilayer, where f is equal to the original argument of the δ -function, k_i are the zeros of this argument, and f' is the derivative with respect to k . This procedure allows us to remove one k -integration and proceed to calculating the current. A small amount of broadening is introduced to handle the singularities that arise near the band edges (an imaginary term $i\epsilon$ is added to the $|f'|$ denominator, with epsilon typically equal to $10^{-2}\hbar v_F$).

8.4 Comparison to experiment

Comparing our theory with the experimental results of Fallahazad et al.[33], we find for the undoped device at room temperature (Fig. 8.2) very good agreement both in terms of the peak shapes and the gate-voltage dependence. For the low-temperature results of Fig. 8.4, small peaks associated with DOS features become prominent, superimposed on a broad momentum-conserving background current. We believe the situation found in experiment at low temperature is the same, showing a similar sharp peak superimposed on a smooth background current.[33] The interpretation offered in Ref. 33 associates the sharp peak itself with a momentum-conserving resonant effect, but no origin for the broad background is provided. Alternatively, in our interpretation, both features can be well understood. The data for the undoped device at room temperature (Fig. 8.2) can be similarly understood within the same framework. Sharp DOS features are not seen for the latter, either in theory or experiment, since the higher temperature leads to a reduction in the amplitude of the sharp peaks (at elevated temperature the tunnel current includes contributions from nearby states that are thermally occupied, leading to a reduction in strength of the sharp peaks). This distinction between DOS versus momentum-conserving effects, as provided by our theory, provides an expanded interpretation of the experimental results.[33]

8.5 Conclusions

While resonant tunneling in MLG heterostructures is novel and intriguing, the additional sub-bands in BLG as well as its unusual behavior in the presence of transverse fields provides many additional channels for interesting tunneling phenomena. Although the results presented here were calculated with zero angular misorientation

(perfect crystallographic alignment) between the two bilayers of graphene, the theory readily computes current for non-zero misorientation, as discussed and observed in prior work for MLG.[1, 32, 110] Concerning possible misorientation within the graphene bilayers themselves, this is known experimentally not to occur for the devices of Fallahazad et al.[33] An additional source of misorientation in the device would be that between the graphene bilayers and the h-BN layers of the tunnel barrier. We have not investigated this effect in detail, although referring to prior work for twisted BLG,[145, 146] it appears that such an effect would give rise to a reduced transmission current through the entire heterostructure. Indeed, for the case of tunneling between MLG layers separated by h-BN, computed tunnel currents agree in detail with experiment, except that the theory is a factor of 10^3 to 10^4 too large.[1] We find a similar discrepancy in absolute magnitude of the current for the present situation of BLG/h-BN devices, and we consider it likely that the reduced conductance of the BLG/h-BN interface is the source of this discrepancy.

For BLG devices, we find that DOS effects are largely unaffected by small amounts of angular misorientation between the bilayers, whereas momentum-conserving resonant peaks are shifted due to the change in conditions required for band intersection, as in monolayer devices. We note that the electronic properties of the BLG can be expected to be influenced by the neighboring h-BN, in analogy with the MLG case.[147] Such effects are typically on the 1 to 10 meV scale; they will be important for a very detailed comparison between experiment and theory, but in terms of the overall distinction that we make here between DOS and momentum-conserving effects these effects can be neglected. Similarly, we neglect many-body modifications to the BLG band structure (including many-body effects between the two graphene bilayers, since they are separated in the experiments[33] by 4 to 6 monolayers of h-BN). The effects of external in-plane magnetic fields have been explored for similar monolayer and monolayer/bilayer devices,[32, 135, 148] but are not considered here for brevity. Finally, inelastic effects may play a role in some devices, particularly at room temperature, however, we have focused here on elastic interactions, which play a large role in the relaxation of momentum conservation and subsequently the strength of resonant behavior compared to background current.

Chapter 9

Progress toward 2D tunneling devices

In addition to characterizing layered 2D heterostructures with LEEM and performing simulations of tunneling transport in such structures, we sought to build up a capability to quickly assemble 2D heterostructures from exfoliated 2D materials in parallel. The advantages of such a capability are twofold:

1. Exfoliated 2D crystals are typically of very high quality; many outstanding results from early investigations of 2D materials involve exfoliated materials, which often provide high crystallinity and purity without much effort beyond obtaining reliable bulk source material.[149, 150]
2. Major strides in experimental techniques for integrating exfoliated crystals into layered heterostructures have enabled rapid fabrication of such structures with arbitrary complexity.[23, 74, 151]

Devices can be made on an individual basis by performing electron-beam lithography in various stages of heterostructure fabrication to pattern critical components such as electrical contacts, gates, and insulating layers. From the perspective of industrial production technologies, electron-beam lithography is a slow, serial method for patterning of devices. Moreover, exfoliated crystals, which are typically small in lateral dimensions and highly variable in terms of yield, are therefore not scalable for production. Nevertheless, for the purposes of scientific research, exfoliated crystals are quite ideal.

Despite the relative ease with which 2D devices can be fabricated using exfoliated materials compared to bottom-up (growth) methods, which are presently lagging behind exfoliation methods in terms of development, the task of making a device from start to finish is still rather complicated. The steps involve exfoliation and identification of useful crystals (by itself, a time-consuming task), a clean and reliable method of picking up and transferring the layers, one-by-one, to build up the desired heterostructure with as few undesirable impurities between the layers as possible,[152] and finally several carefully-designed steps to define electrical contacts with suitable work functions, low contact resistances, and minimal influence on the physics of the

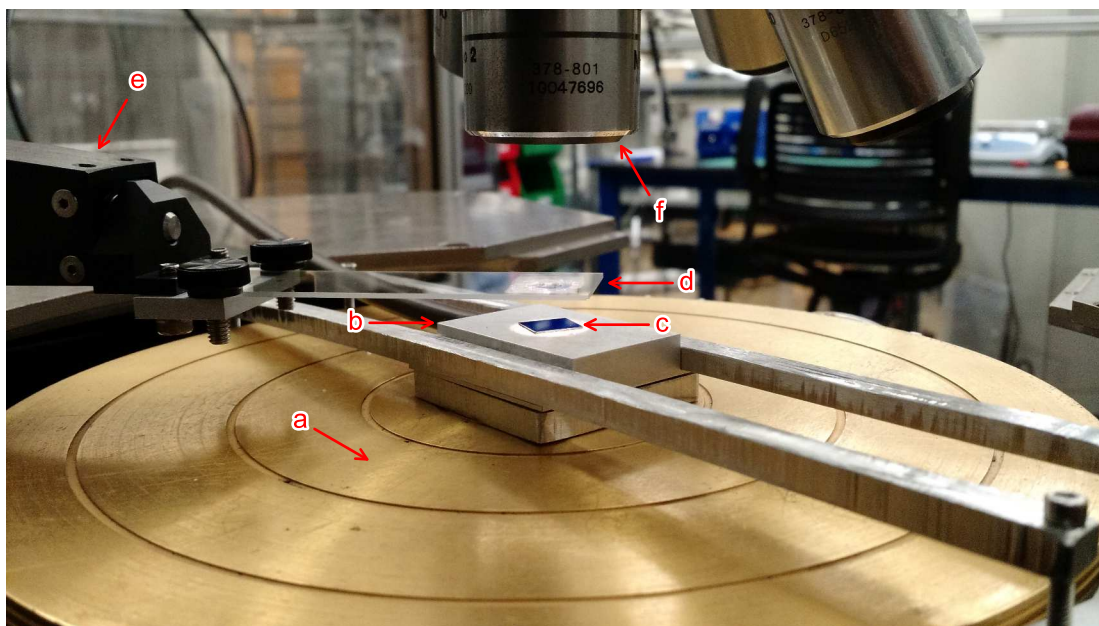


Figure 9.1: Photograph of Wentworth PML8000 probe station and micromanipulator modified for transfer of 2D layers, with (a) Temptronic TPO3020B temperature controller and heated stage, (b) custom vacuum chuck, (c) substrate with exfoliated crystals, (d) transfer slide with polymer stack (underneath) used to pick-up and put-down 2D crystals, (e) micromanipulator arm, and (f) optical microscope for aligning layers and monitoring assembly.

device itself. Tunneling devices require even more care in design and fabrication given that tunneling is exponentially sensitive to distance; uniformity of barrier thickness is essential, meaning intercalated materials and defects are even more critical than in conventional devices. Finally, crystal orientation between the layers is often highly relevant to the tunneling, as discussed in Chapter 7. Although diffraction techniques such as LEED may provide some insight into crystal orientation, integration of diffraction into the process flow of fabricating a device is non-trivial.

These difficulties must be overcome, however, if the goal is to measure transport in real 2D devices. To this end, I will outline the state of progress toward this goal at Carnegie Mellon University, beginning with my personal contribution to creating a new user facility in Section 9.1.

9.1 A new facility for 2D crystal exfoliation and transfer

As part of a collaborative center at Carnegie Mellon University aimed at studying 2D materials, I designed and outfitted a new facility for the express purpose of exfoliating and transferring 2D crystals for device fabrication. With the intention of enabling the cleanest interfaces possible, all equipment and materials in the facility are enclosed in a custom 130 ft² clean room area with two large HEPA filters maintaining a modest positive pressure with respect to outside air to purge the facility area of the majority of airborne particulates. Inside the clean area are nitrogen-purged and vacuum storage systems for long-term storage of bulk material sources (with varying degrees of air sensitivity) and samples, an exfoliation area, optical microscope, atomic force microscope (AFM), and transfer station (Fig. 9.1).

Exfoliated crystals are prepared by repeated mechanical cleavage (separating the layers) of a small flake of bulk material using Scotch tape or polydimethylsiloxane (PDMS) to achieve a high density of thin (not necessarily 2D) material on the tape (or PDMS). The tape is then adhered to a separately-prepared clean silicon “chip” (see item (c) in Fig. 9.1) with a 300 nm SiO₂ oxide layer. Depending on the material, heat is sometimes used to promote contact between the crystals on the tape and the SiO₂/Si surface. The tape is removed from the surface, and if the procedure was successful then there will be a number of crystals that remain on the surface of the chip, having cleaved once again from the underside of thicker crystals which remain stuck to the tape. The fact that this procedure works at all is a bit miraculous, but indeed, if performed correctly, this method can yield 2D crystals from many types of layered materials.

Identification of exfoliated crystals proceeds by optical inspection, with the thinnest crystals (monolayer, bilayer, up to a few layers) being visible, and in fact, distinguishable, due to an optical interference effect with the 300 nm oxide layer.[153] A single exfoliation attempt with high-quality graphite onto a 1 cm² chip typically yields on the order of 2 useful monolayers of graphene, each with lateral dimensions ranging from 10 μm to 100 μm. Exfoliation of bulk h-BN provides similar overall yield, but fewer monolayers, and TMD materials are notoriously more difficult to coax into monolayer form.

Having identified potentially-useful 2D crystals optically, AFM is performed on the crystals to establish the flatness and cleanliness (absence of hydrocarbons, tape residue, or other contaminants), and possibly the thickness, although other methods are typically more reliable for the latter. Crystals with clean surfaces are then assembled into a heterostructure using a dry-transfer method that relies on building the layered structure from the top, down. The top layer is picked up first, using a special polymer stack on the underside of a glass slide mounted in a micromanipulator (Fig. 9.1).[23] Subsequent layers are then picked up using the van der Waals interaction with the layer above so that the interface between the two layers does not come

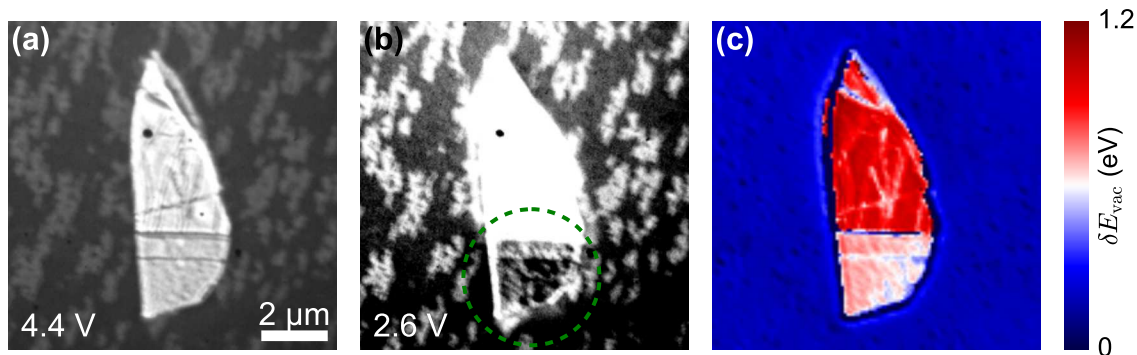


Figure 9.2: (a) Low-energy electron micrograph of mechanically exfoliated WSe_2 on epitaxial graphene on SiC, imaged at 4.4 V sample bias. Central bright region is many-layer WSe_2 , whereas surrounding variegated regions are 3ML and 4ML graphene. (b) Another micrograph of the same area at 2.6 V, with high contrast within the WSe_2 due to partial electron transparency in the lower (encircled) part of the crystal at this energy, revealing the pattern of graphene below the WSe_2 layers. (c) Relative work function map of the surface (electrostatic potential variation, δE_{vac}) highlighting the large difference between WSe_2 and graphene surfaces, calculated using a modification of the method outlined in Section 2.2.

into contact with any polymer or other contaminant. The layers are picked up in this way sequentially, starting with the top layer and ending with the bottom layer, at which point the entire heterostructure (suspended on the transfer slide) is deposited onto a desired substrate by heating (and melting) the bottom polymer layer, later removed with chloroform. Although the exposed surfaces of the heterostructure come into contact with polymers and other chemicals, the interior interfaces are kept atomically clean by the interlayer van der Waals interactions, and thus it is possible to make extremely high-quality devices with this method.

9.2 Initial studies of exfoliated materials and challenges

Presently, the methods described in Section 9.1 are successfully being carried out by me and other users of the facility to fabricate heterostructures. My own work in this area has led to preliminary studies of exfoliated materials in LEEM, as shown in Fig. 9.2. Going forward, LEEM will certainly prove to be a valuable tool for probing heterostructures of exfoliated materials due to the relative ease with which samples can be prepared for study in LEEM. The expectation is that LEEM will provide critical information regarding layer thicknesses (Section 3.5), interlayer crystal orientations (Section 3.3), defect density (Section 5.1), and work function variations

(Section 4.3), among other quantities. As an extension to measuring point-to-point variations in work function, there may be cases where *spatially-resolved* work function mapping (see Fig. 9.2(c), for example) can be illuminating, especially related to transport phenomena such as contact resistances and spatial inhomogeneity.

That being said, there are challenges which must be overcome for using LEEM to study structures that will also be measured with electrical transport. One of the basic requirements of LEEM samples is that they are able to carry away excess charge during imaging, so as to prevent charging (which has the effect of deflecting the beam and thus detrimentally affecting the image). The simplest way around this restriction for small crystals that may be semi-insulating is to place them on an appropriate, conducting substrate. For example, the sample shown in Fig. 9.2 makes use of epitaxial graphene as a conducting substrate for imaging WSe_2 , which may be insulating or semiconducting based on the position of the Fermi level (as discussed in Section 4.4). For measuring transport, however, a conducting substrate is usually undesirable since it makes contacting the device region with isolated leads a difficult task. In addition, devices that require a top gate (for transport modulation) or encapsulation (for materials and properties that are sensitive to the environment) will present additional challenges if they are to also be studied with LEEM, since LEEM is most sensitive to the top-most atomic surface, and the electrons do not generally penetrate more than a handful of atomic layers in total. These outstanding questions will be addressed by me and other students in order to make correlated measurements between LEEM and electrical transport in the near future.

9.3 Layered heterostructures of 2D materials for device transport

Progress toward making *devices* from layered heterostructures is also ongoing. Members of the Hunt group (users of the transfer facility) and I are currently working to develop the nanofabrication processes needed to pattern and define device boundaries, deposit contacts and gates, and wire bond the finished devices into chip carriers designed for performing transport measurements. These projects are currently in various stages of achievement, with the effort being led by Ben Hunt and his student, Devashish Gopalan, in particular. In parallel, efforts are underway to enable low-temperature transport with a liquid-He-cooled physical property measurement system (PPMS), which will be greatly augmented by the addition of a dilution refrigerator (an independent system which will allow cooling below 300 mK and will include a superconducting magnet for field-dependent transport measurements) to the Hunt lab in the Fall of 2016.

In addition to these activities, I have personally been involved in a project to fabricate monolayer graphene diodes led by Jeffrey Weldon and his student, Mohamed Darwish. Toward this goal, I, with the help of students Jean-Yves Desaulles and

Andrew Ye, have assembled a number of monolayer and bilayer graphene structures supported by h-BN in order to achieve high mobility in lateral transport through the graphene layers. Darwish has used the provided structures for subsequent device nanofabrication steps (patterning and defining contacts) along with multiple stages of characterization.

With these initial steps accomplished, current and future users of the exfoliation and transfer facility will carry this work forward, with many more results from 2D heterostructures and devices to follow.

Chapter 10

Conclusions

In the course of this thesis, I have introduced two-dimensional (2D) materials and their heterostructures as a new paradigm for the fields of physics and nanoscience. I argued that layered heterostructures in particular, that is, individually-stacked monolayers of different 2D crystals with deliberate arrangement, expand the available parameter space for new physics and interesting phenomena greatly, and within this space I have chosen to focus on interlayer transport in a few specific structures. I outlined the method of low-energy electron microscopy (LEEM), its utility for studying 2D materials, and its unique spectroscopic capabilities, which have yet to achieve anywhere near the notoriety (let alone ubiquity) of optical, x-ray, or scanning probe methods, despite its complementary relevance.

In Chapters 3, 4, and 5, I presented several examples of these capabilities. I showed that electron reflectivity spectra from the surface of few-layer WSe₂ on epitaxial graphene allow direct discrimination of the number of WSe₂ layers at each point in a collected series of images. A similar method was previously applied to few-layer graphene and h-BN by other workers, however, the situation for WSe₂ is far more complex due to a high level of state-mixing in the WSe₂ band structure and non-trivial inelastic considerations. By carefully sorting out these details, I have developed a method for unambiguously identifying monlayer, bilayer, and trilayer WSe₂, and hopefully provided insight for applying similar analyses to other transition metal dichalcogenide (TMD) materials.

Considering the interface between two dissimilar 2D materials, I used the very-low energy part of reflectivity spectra to measure relative work function differences between WSe₂-epitaxial graphene and MoSe₂-epitaxial graphene. In the former case, a large difference in work function between the WSe₂ and graphene was associated with Schottky barrier tunneling in conducting-AFM measurements of transport between the layers, whereas a negligible difference in work function resulted in ohmic contact between the TMD and graphene. The quantitative results for work function differences in the two cases were used to model a charge transfer process that provided an explanation for the change in transport behavior.

From a methodology standpoint, there are two significant points regarding the results of this work. Firstly, it is worthwhile to reflect on the fact that LEEM is a tool that directly probes unoccupied, unbound states that exist *above* the vacuum level. On the other hand, the conclusions drawn from the analyses in Chapter 4 are related to electrical transport phenomena, which are manifestly relevant to states near the Fermi level, far below what is directly accessible by LEEM electrons. Therefore, I will emphasize here that LEEM not only probes a complementary part of the solid state energy spectrum with respect to other methods, but that measurements obtained from this unusual high-energy domain can be related to everyday phenomena such as electrical conduction.

As a second point of this examination, based on the collection of LEEM methods presented in this thesis, it is remarkable from the perspective of other, more involved experimental methods, which require contacts, patterning, or other forms of sample preparation, that the measurements gleaned from such methods are even possible from what essentially amounts to imaging of surfaces. As a final application of the LEEM methods developed in the earlier chapters, large work function differences between MoSe₂ and epitaxial graphene were measured and provided as evidence (in tandem with diffraction) of enormous defect density in the MoSe₂ films.

In Chapters 6, 7 and 8, efforts from a parallel thrust aimed at modeling interlayer tunneling between 2D materials were described and employed to provide predictions of novel phenomena. Beginning with the general theory established by Bardeen, and the adaptation of that theory to two dimensions by Feenstra et al. [110], I presented models for computing tunneling currents between graphene sheets with arbitrary gate modulation, coherence length, crystallographic misorientation, and an advanced treatment of the tunneling barrier. The primary prediction of this work is resonant tunneling behavior that depends strongly on the aforementioned characteristics of the junction. The model was extended to bilayer graphene tunneling junctions, and additional phenomena resulting from the unique band structure of bilayer graphene were illustrated. These predictions were compared to experimental results measured in monolayer and bilayer graphene based tunneling devices, and the agreement between the computed and measured tunneling characteristics was shown to be quite remarkable.

Finally, in Chapter 9 progress toward my own experimental realizations of layered 2D heterostructures and interlayer tunneling devices were discussed in the context of my involvement in contributing to a collaborative research center at Carnegie Mellon University. With an eye toward prospective outcomes emerging from these ongoing efforts, I have great confidence that many new and interesting results pertaining to layered 2D heterostructures are imminent.

Appendix A

2D–2D tunneling in the zero-coherence-length limit

We briefly comment on one additional aspect of the tunneling formalism introduced in Chapter 7, namely, the use of the density-of-states formula of Eq. (7.1) for computing tunneling current.[112] This formula is commonly used in tunneling computations, although obtaining an absolute magnitude of the current is problematic with this approach since it is not obvious what the appropriate pre-factors in front of the integral should be. Of course, with the full theory of Eq. (7.2), we can obtain a current with well-defined magnitude. Also, in the limit of $L \rightarrow 0$ of that theory, it is easily shown that we recover Eq. (7.1). However, when we compute currents in that limit, i.e. for smaller and smaller L values, then the currents that we obtain (actually they are current densities, since the computation is for a specific L^2 area) become unphysically small. The question we must address is, what is the fundamental source of this decrease in current density for $L \rightarrow 0$, and can we somehow produce a current density whose magnitude is physically meaningful even in this limit.

The origin of the unphysical $L \rightarrow 0$ limit of the full theory of Eq. (7.2), when evaluated together with Eq. (7.4) or (7.6) and Eq. (7.7) or (7.10), arises from our assumption of limiting the area over which the surface integral in Eq. (7.2) is performed. For very small L values, we then encounter a situation in which the tunneling is restricted to a small area of one electrode over to the same small area of the opposite electrode. This restriction is invalid since we are ignoring the tunneling to neighboring areas in the opposing electrodes. That is, we must consider spreading (dispersion) of these states as they extend across the barrier. To properly deal with this situation, we construct states on each electrode that are restricted to an area L , hence with wavefunctions proportional to $[\Theta(x + L/2) - \Theta(x - L/2)][\Theta(y + L/2) - \Theta(y - L/2)] e^{i\mathbf{k}\cdot\mathbf{r}}$ where $\Theta(x)$ is a Heaviside step function. We Fourier transform these wavefunctions in order to deduce their dispersion in the barrier, with each Fourier component extending into the barrier with an exponential decay constant

$$\kappa' = \sqrt{\kappa^2 + \eta^2}, \tag{A.1}$$

(assuming equal effective masses in the lateral and perpendicular directions) where $\eta \equiv |\boldsymbol{\eta}|$ denotes the lateral wavevector variable in the Fourier transform. On each electrode the total wavefunction is written as a summation of such states, localized on adjoining areas. We then work through the Bardeen formalism.

For a given state restricted to an area $A = L^2$ of the left-hand electrode, we can evaluate contributions to the matrix element Eq. (7.3) from the overlap of that state with states from all areas of the right-hand electrode. To illustrate our result, we compare it to the surface integral in Eq. (7.7), for the case of zero misorientation and where we include a $\kappa e^{-\kappa d}$ term in that integrand (i.e. from the prefactor of Eq. (7.4)). Whereas Eq. (7.8) was obtained by using an *ad hoc* restriction of this surface integral over the area A , we now have a more rigorous treatment using our constructed wavefunctions. The term analogous to Eq. (7.7) then becomes

$$\begin{aligned} \frac{1}{A} \int dS \kappa e^{-\kappa d} e^{i\boldsymbol{\Delta}\mathbf{k}\cdot\mathbf{r}} &\rightarrow \frac{A}{(2\pi)^2} \sum_{m,n} \int_{-\infty}^{\infty} d\eta_x \int_{-\infty}^{\infty} d\eta_y \kappa' e^{-\kappa' d} \\ &\times \text{sinc}\left(\frac{(\eta_x - k_{R,x})L}{2}\right) \text{sinc}\left(\frac{(\eta_y - k_{R,y})L}{2}\right) \\ &\times \text{sinc}\left(\frac{(\eta_x - k_{L,x})L}{2}\right) \text{sinc}\left(\frac{(\eta_y - k_{L,y})L}{2}\right) \\ &\times e^{i[(\eta_x - k_{R,x})mL + (\eta_y - k_{R,y})nL]} \end{aligned} \quad (\text{A.2})$$

where m and n label areas of the right-hand electrode, both extending over $0, \pm 1, \pm 2, \dots$

The $m = n = 0$ term of the summation on the right-hand side of Eq. (A.2) dominates for large L , and in that case the expression on the left-hand side of the equation (evaluated as in Eq. (7.8)) is recovered. The additional terms in that sum are negligible for $L > 10$ nm, but they make important contributions for smaller L values. Performing the complete summation for small L values becomes computationally demanding. However, we find for the parameters of our simulations described in Section 7.4 (1.34 nm-wide tunnel barrier with tunneling decay constant 6 nm^{-1}), the results of the full summation for $L \rightarrow 0$ matches well to the result of including only the $m = n = 0$ term but with the fixed value of $L = 1.4$ nm. Therefore, to incorporate an absolute scale of current densities on computations employing Eq. (7.1), we can simply adjust the magnitude of the results so that they match that of a computation employing Eq. (7.4) together with Eq. (7.10) using $L = 1.4$ nm.

We note that the voltage-dependence of the computation using Eqs. (7.4) and (7.10) with $L = 1.4$ nm is very close to that obtained with Eq. (7.1), so in principle we could simply use the former to report the results. Nevertheless it is desirable to use the latter for computations in which no trace of momentum conservation is evident in the experimental data, while at the same time including an estimate of the absolute magnitude for those current densities. We achieve that goal by matching the magnitudes of the two computational results. Of course, this same procedure would

be necessary (and would yield similar results) if employing the theory of Ref. 31, i.e. Eq. (7.6) together with Eq. (7.9) or (7.10), for very large q_c values.

Appendix B

Details of resonant tunneling model for graphene and its bilayers

The following sections provide additional details regarding the analytic portion of the momentum-conserving 2D–2D tunneling calculation, including wavevector matching (for computing current) and densities-of-states (for solving electrostatics).

B.1 Monolayer graphene

For comparison to the more complicated cases, I will reproduce the equations that govern resonant tunneling for the monolayer graphene case with elastic scattering. Using the Bardeen formalism, we have for the tunneling current

$$I_{\text{elas}} = g_V g_S \frac{2\pi e}{\hbar} \sum_{\alpha\beta} |M_{\alpha\beta}|^2 [f_L(E_\alpha) - f_R(E_\beta)] \delta(E_\alpha - E_\beta). \quad (\text{B.1})$$

which involves a sum over all states α, β in each graphene electrode. The matrix element $M_{\alpha\beta}$ is evaluated using graphene basis functions in Bloch form to obtain

$$M_{\mathbf{k}_R \mathbf{k}_L} = \frac{\hbar^2}{2m} \frac{\kappa e^{-\kappa d}}{D} g_\omega(\theta_R, \theta_L) \frac{1}{A} \int dS e^{i\mathbf{Q}\cdot\mathbf{r}} e^{i(\mathbf{k}_R - \mathbf{k}_L)\cdot\mathbf{r}}, \quad (\text{B.2})$$

which allows us to write the current as a sum over wavevectors,

$$I_{\text{elas}} = g_V g_S \frac{2\pi e}{\hbar} \left(\frac{\hbar^2}{2m} \right)^2 \sum_{\mathbf{k}_R \mathbf{k}_L} \left(\frac{\kappa e^{-\kappa d}}{D} \right)^2 |\Lambda(\Delta\mathbf{k})|^2 [f_L(E_L) - f_R(E_R)] \delta(E_L - E_R), \quad (\text{B.3})$$

with $\Lambda(\Delta\mathbf{k}) = \frac{g_\omega}{A} \int dS e^{i\mathbf{Q}\cdot\mathbf{r}} e^{i\Delta\mathbf{k}\cdot\mathbf{r}}$ where $\Delta\mathbf{k} = \mathbf{k}_R - \mathbf{k}_L$ and the surface integral is taken over an area defined by the phase coherence length, L . To evaluate the delta function which enforces energy conservation, we must convert the sums over all states to integrals, and rewrite $\delta(E_L - E_R)$ in terms of wavevectors. Using the

linear approximation to the monolayer graphene dispersion $E(k) \approx \hbar v_F k$, we write the energy in each electrode as $E_i = E(k_i) + \phi_i$, where ϕ_i is the electrostatic potential at the Dirac point, and hence for the energy range above both Dirac points (REGION I).

$$E_L - E_R = E(k_L) - E(k_R) + \phi_L - \phi_R = \hbar v_F (k_L - k_R) + eV', \quad (\text{B.4})$$

where $eV' = \phi_L - \phi_R$ is the electrostatic potential difference between the graphene electrodes. We replace the delta function of $E_L - E_R$ with a version in terms of k ,

$$\delta(f(k_R, k_L)) \rightarrow \frac{\delta(k_R - k_0)}{|f'(k_0)|}, \quad (\text{B.5})$$

where the zero of $f(k_R, k_L)$ is found using Eq. (B.4) to be

$$\text{REGION I:} \quad k_0 = k_L + eV'/\hbar v_F = k_L + k', \quad (\text{B.6})$$

with $k' = eV'/\hbar v_F$. From this, it follows that $|f'(k_0)| = \hbar v_F$. This new delta function removes the integral over the magnitude of k_R , leaving two angular integrals and the integral over k_L . For the energy range below both Dirac points (REGION III), the energies are negative with respect to the charge neutrality point $E(k) \approx -\hbar v_F k$ and thus

$$E_L - E_R = -\hbar v_F (k_L - k_R) + eV', \quad (\text{B.7})$$

which yields

$$\text{REGION III:} \quad k_0 = k_L - k'. \quad (\text{B.8})$$

Similarly, in the energy range between the two Dirac points (REGION II), one energy is positive while the other is negative, and generally

$$\text{REGION II:} \quad k_0 = |k'| - k_L. \quad (\text{B.9})$$

In order to properly determine the electrostatics, one must also compute the number of carriers in each electrode which requires the density of states. For a dispersion relation of $E(k) \approx \hbar v_F k$ in two dimensions with spin and valley degeneracy factors of 2, the occupation factor for each level is

$$n(k) = g_V g_S \frac{1}{(2\pi)^2} \pi k^2 = \frac{1}{\pi} \left(\frac{E}{\hbar v_F} \right)^2, \quad (\text{B.10})$$

and thus the density of states is

$$\rho(E) = \frac{dn}{dE} = \frac{2}{\pi} \frac{|E|}{(\hbar v_F)^2}. \quad (\text{B.11})$$

From this, we calculate the electron and hole density in each electrode using

$$n_i = \int_{\phi_i}^{\infty} dE \frac{\rho(E - \phi_i)}{e^{(E - \mu_i)/kT} + 1} = -\frac{2}{\pi} \left(\frac{kT}{\hbar v_F} \right)^2 \text{Li}_2 \left(-e^{(\mu_i - \phi_i)/kT} \right) \quad (\text{B.12a})$$

$$p_i = \int_{-\infty}^{\phi_i} dE \frac{\rho(E - \phi_i)}{e^{(\mu_i - E)/kT} + 1} = -\frac{2}{\pi} \left(\frac{kT}{\hbar v_F} \right)^2 \text{Li}_2 \left(-e^{(\phi_i - \mu_i)/kT} \right), \quad (\text{B.12b})$$

with the second-order polylogarithm, $\text{Li}_2(z)$. In the limit that $T \rightarrow 0$, the Fermi-Dirac function approaches a step-function, and the total number of carriers reduces to

$$\lim_{T \rightarrow 0} n_i = \int_{\phi_i}^{\infty} dE \rho(E - \phi_i) \Theta(E - \mu_i) = \frac{1}{\pi} \left(\frac{\mu_i - \phi_i}{\hbar v_F} \right)^2. \quad (\text{B.13})$$

B.2 Bilayer graphene: parabolic dispersion

The simplest model for bilayer graphene assumes a parabolic dispersion $E(k) \approx \alpha k^2$, with the coefficient of proportionality $\alpha = (\hbar v_F)^2 / t_{\perp}$ (with interlayer hopping energy t_{\perp}) extracted from the tight-binding method. Borrowing Eq. (B.3) from the monolayer case, we proceed to evaluating the delta function $\delta(E_L - E_R)$ for each of the relevant energy regions. In REGION I, above both Dirac points (conduction- to conduction-band tunneling) we have

$$E_L - E_R = \alpha(k_L^2 - k_R^2) + eV', \quad (\text{B.14})$$

which tends to zero at

$$\text{REGION I:} \quad k_0 = \sqrt{k_L^2 + eV'/\alpha} \quad (\text{B.15})$$

with the derivative $|f'(k_0)| = 2\alpha k_0$ evaluated at that point. In REGION III (valence- to valence-band tunneling) both energies are negative and therefore

$$E_L - E_R = -\alpha(k_L^2 - k_R^2) + eV', \quad (\text{B.16})$$

which gives us $f(k_0) = 0$ for

$$\text{REGION III:} \quad k_0 = \sqrt{k_L^2 - eV'/\alpha}. \quad (\text{B.17})$$

In REGION II (unlike-band tunneling), we must examine separate cases for each sign of eV' . Doing this, we obtain one equation which holds for both zeros (here $k'^2 = |eV'|/\alpha$),

$$\text{REGION II:} \quad k_0 = \sqrt{|eV'|/\alpha - k_L^2} = \sqrt{k'^2 - k_L^2}. \quad (\text{B.18})$$

For the electrostatics calculation, we can simply replace the k^2 in Eq. (B.10) with the rearranged dispersion relation $k^2 = |E|/\alpha$ to obtain

$$n(k) = g_V g_S \frac{1}{(2\pi)^2} \pi k^2 = \frac{|E|}{\pi \alpha}. \quad (\text{B.19})$$

Taking the derivative with respect to energy, we calculate the density of states

$$\rho(E) = \frac{dn}{dE} = \frac{1}{\pi \alpha}, \quad (\text{B.20})$$

which is constant (a well-known result for parabolic dispersion in two dimensions). The charge densities for each graphene sheet are then easily obtained for finite temperature,

$$n_i = \frac{1}{\pi\alpha} \int_{\phi_i}^{\infty} dE \frac{1}{e^{(E-\mu_i)/kT} + 1} = \frac{kT}{\pi\alpha} \ln(1 + e^{(\mu_i-\phi_i)/kT}) \quad (\text{B.21a})$$

$$p_i = \frac{1}{\pi\alpha} \int_{-\infty}^{\phi_i} dE \frac{1}{e^{(\mu_i-E)/kT} + 1} = \frac{kT}{\pi\alpha} \ln(1 + e^{(\phi_i-\mu_i)/kT}), \quad (\text{B.21b})$$

as well as in the low-temperature limit,

$$\lim_{T \rightarrow 0} n_i = \frac{1}{\pi\alpha} \int_{\phi_i}^{\infty} dE \Theta(E - \mu_i) = \frac{|\mu_i - \phi_i|}{\pi\alpha}. \quad (\text{B.22})$$

Curiously, when we calculate the net charge using the temperature-dependent forms shown in Eqs. (B.21a) and (B.21b), we find that the result is independent of temperature and equal to Eq. (B.22),

$$n_i - p_i = \frac{kT}{\pi\alpha} [\ln(1 + e^{(\mu_i-\phi_i)/kT}) - \ln(1 + e^{(\phi_i-\mu_i)/kT})] = \frac{|\mu_i - \phi_i|}{\pi\alpha}. \quad (\text{B.23})$$

B.3 Bilayer graphene: hyperbolic dispersion

Although the parabolic approximation to the bilayer graphene dispersion is appropriate for very small energies, the true bilayer dispersion quickly becomes non-parabolic as one extends out to energies that are relevant for off-resonance currents (high-voltage behavior). These effects can be captured by writing the dispersion in a hyperbolic form which is parabolic for $\hbar v_F k \ll t_{\perp}$ and linear in the opposite limit $\hbar v_F k \gg t_{\perp}$,

$$E \approx \frac{t_{\perp}}{2} \left[\sqrt{1 + (k/k_c)^2} \pm 1 \right], \quad (\text{B.24})$$

with the transitional value $k_c = t_{\perp}/2\hbar v_F$ between the two regimes, and where the upper (lower) sign corresponds to the higher (lower) energy sub-band. For convenience, we define $h(k) \equiv \sqrt{1 + (k/k_c)^2}$. Considering only the lower conduction bands of both electrodes, we write the argument of the delta function in Eq. (B.3) as

$$E_L - E_R = \frac{t_{\perp}}{2} [h(k_L) - h(k_R)] + eV', \quad (\text{B.25})$$

and we find that the zero occurs when

$$\text{REGION I:} \quad k_0 = k_c \sqrt{[h(k_L) + 2eV'/t_{\perp}]^2 - 1}. \quad (\text{B.26})$$

The derivative of Eq. (B.25) gives us $|f'(k_0)| = 2\alpha k_0/h(k_0)$. In REGION III (considering only the upper valence bands), we have negative energies and

$$E_L - E_R = -\frac{t_\perp}{2}[h(k_L) - h(k_R)] + eV'. \quad (\text{B.27})$$

The zero of this equation is

$$\text{REGION III:} \quad k_0 = k_c \sqrt{[h(k_L) - 2eV'/t_\perp]^2 - 1}. \quad (\text{B.28})$$

In the unlike-band tunneling region, we evaluate the two cases of positive and negative eV' to obtain

$$\text{REGION II:} \quad k_0 = k_c \sqrt{[h(k_L) - 2|eV'|/t_\perp - 2]^2 - 1}. \quad (\text{B.29})$$

Before we begin calculating the carrier densities required for electrostatics, we must first invert the dispersion shown in Eq. (B.24) (for the lower sign),

$$k^2 = \left(\frac{2k_0}{t_\perp}\right)^2 |E| (|E| + t_\perp) = \frac{|E|}{(\hbar v_F)^2} (|E| + t_\perp). \quad (\text{B.30})$$

We use this equation to determine the occupation factor for each k ,

$$n(k) = g_V g_S \frac{1}{(2\pi)^2} \pi k^2 = \frac{|E|}{\pi(\hbar v_F)^2} (|E| + t_\perp), \quad (\text{B.31})$$

and take the derivative to get the density of states

$$\rho(E) = \frac{dn}{dE} = \frac{2|E| + t_\perp}{\pi(\hbar v_F)^2} = \frac{1}{\pi\alpha} + \frac{2|E|}{\pi(\hbar v_F)^2}, \quad (\text{B.32})$$

which is in fact a sum of the monolayer and parabolic densities of states. As such, the carrier densities will be sums of the monolayer and parabolic cases as well;

$$n_i = \frac{kT}{\pi\alpha} \ln(1 + e^{(\mu_i - \phi_i)/kT}) - \frac{2}{\pi} \left(\frac{kT}{\hbar v_F}\right)^2 \text{Li}_2(-e^{(\mu_i - \phi_i)/kT}) \quad (\text{B.33a})$$

$$p_i = \frac{kT}{\pi\alpha} \ln(1 + e^{(\phi_i - \mu_i)/kT}) - \frac{2}{\pi} \left(\frac{kT}{\hbar v_F}\right)^2 \text{Li}_2(-e^{(\phi_i - \mu_i)/kT}), \quad (\text{B.33b})$$

and in the low-temperature limit,

$$\lim_{T \rightarrow 0} n_i = \frac{|\mu_i - \phi_i|}{\pi\alpha} + \frac{1}{\pi} \left(\frac{\mu_i - \phi_i}{\hbar v_F}\right)^2. \quad (\text{B.34})$$

Appendix C

Resonant tunneling between transition metal dichalcogenides

The following sections extend the band model for graphene–graphene interlayer tunneling to enable calculation of tunneling current between semiconducting transition metal dichalcogenides. The described model uses an approximate form for the semiconducting bands around the K and K' points of the Brillouin zone, and neglects the details of the TMD wavefunctions, which in general will be more complicated than those of graphene.

C.1 Tight-binding model and dispersion

Following the discussion of a simple tight-binding model for monolayers of transition metal dichalcogenides (TMDs) by Liu et al. [95], we approximate the low-energy behavior of electrons by expanding the tight-binding Hamiltonian around the K -point. Keeping only the lowest order term, we write the reduced $\mathbf{k} \cdot \mathbf{p}$ two-band Hamiltonian as

$$H_0(\mathbf{k}) \approx \begin{pmatrix} \Delta/2 & \hbar v(\tau k_x - ik_y) \\ \hbar v(\tau k_x + ik_y) & -\Delta/2 \end{pmatrix} = \begin{pmatrix} \Delta/2 & \tau \hbar v k e^{-i\tau\phi} \\ \tau \hbar v k e^{i\tau\phi} & -\Delta/2 \end{pmatrix}, \quad (\text{C.1})$$

where $k = |\mathbf{k}|$, $\phi = \arctan(k_x/k_y)$, $\tau = \pm 1$ is a valley-index, Δ is the band gap of the TMD, and $\hbar v = at$ in the notation of Liu et al.. The eigenvalues for this simple model are hyperbolic,

$$E(k) = \pm \frac{1}{2} \sqrt{(2\hbar v k)^2 + \Delta^2}. \quad (\text{C.2})$$

It is possible at this stage to make a simple, parabolic “effective mass” approximation using this result by expanding to lowest order in k ,

$$E(k) = \pm \frac{1}{2} \left[\Delta + \frac{(2\hbar v k)^2}{2\Delta} + \mathcal{O}(k^4) \right] \approx \pm \left[\frac{\Delta}{2} + \frac{\hbar^2 k^2}{2m^*} \right], \quad (\text{C.3})$$

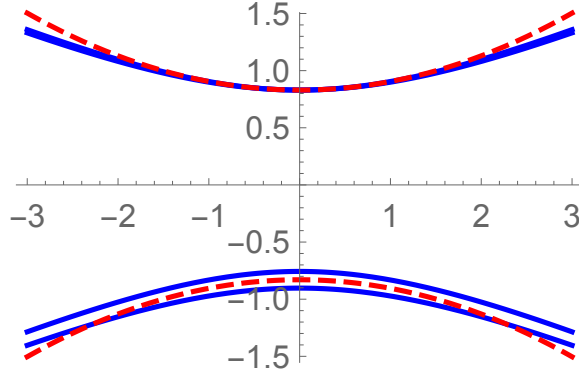


Figure C.1: Energy versus wavevector $E_s(k)$ around the K -point using a first-order two-band effective Hamiltonian with spin-orbit coupling (solid, blue), and a parabolic effective mass approximation (dashed, red). Energy axis in units of eV and k -axis in nm^{-1} .

with $m^* \equiv \Delta/2v^2$, but the hyperbolic form is at least as compact and a bit more accurate. We can go a bit further by including spin-orbit coupling (which is relevant in many 2D TMDs) according to the prescription by [Liu et al.](#),

$$H_{s-o} \approx H_0(\mathbf{k}) + \begin{pmatrix} 0 & 0 \\ 0 & \tau s \lambda \end{pmatrix}, \quad (\text{C.4})$$

for spin-orbit perturbation parameter λ (see Table IV of Ref. [95](#)) and spin-index $s = \pm 1$. The eigenvalues including spin-orbit coupling now take the form,

$$E_{s,\tau}(k) = \frac{1}{2} \left[\tau s \lambda \pm \sqrt{(2\hbar v k)^2 + (\Delta - \tau s \lambda)^2} \right]. \quad (\text{C.5})$$

The valley-index τ appears explicitly in the dispersion, indicating that the valley degeneracy has been lifted by spin-orbit splitting. However, we cannot distinguish between the spin-states in our device (or rather, between the states involved in spin-orbit splitting), so we can ignore the valley-index and retain a valley degeneracy factor of $g_v = 2$,

$$E_s(k) = \frac{1}{2} \left[s \lambda \pm \sqrt{(2\hbar v k)^2 + (\Delta - s \lambda)^2} \right]. \quad (\text{C.6})$$

This dispersion relation is compact enough for direct use in our tunneling calculation, while also properly capturing the non-parabolicity of the bands at low energies as well as the primary effect of spin-orbit coupling, which is asymmetric for electrons versus holes. This model will likely be sufficient for computation for both like-band and unlike-band tunneling modes. In particular, the band-splitting from spin-orbit coupling will properly capture the effect on the density of states near the band edge, which governs the turn-on characteristic of a device based on unlike-band tunneling, a tunneling field-effect transistor (TFET).

C.2 Energy-conservation between tunneling states in transition metal dichalcogenides

The modification in the energy-conservation term between monolayer graphene devices and TMD devices is straightforward. The delta function $\delta(E_L - E_R)$ must be rewritten in terms of the wavevector in each electrode and summed over the available bands,

$$\delta(E_L - E_R) \rightarrow \sum_i \frac{\delta(k - k_i)}{|f'(k_i)|}, \quad (\text{C.7})$$

where the sum index i runs over $s = \pm 1$ for both the conduction and valence bands (four terms in total). Here, f refers to the original argument of the delta function and k_i are the zeros of that function,

$$f \equiv E_L - E_R = E_s^\pm(k_L) - E_{s'}^{\pm'}(k_R) + \phi_L - \phi_R. \quad (\text{C.8})$$

Solving this expression for zero will require the inversion of Eq. (C.6),

$$k_s(E) = \frac{1}{2\hbar v} \sqrt{(2E - s\lambda)^2 - (\Delta - s\lambda)^2}, \quad E \geq \frac{\Delta}{2} \text{ or } E \leq -\frac{\Delta}{2} + s\lambda. \quad (\text{C.9})$$

Using Eq. (C.9) to evaluate the solution of $f = 0$ yields

$$k_i = k_s^\pm[E_{s'}^{\pm'}(k_R) - eV'], \quad (\text{C.10})$$

with $eV' = \phi_L - \phi_R$ and where the band gaps Δ_L , Δ_R and spin-orbit parameters λ_L , λ_R are defined separately for each material. The zeros k_i define the relationship between the magnitude of wavevectors imposed by energy conservation, and will differ for each of the three energy regions in the tunneling calculation. The limits of each region in TMDs will extend from the band edges instead of from the Dirac point, as in monolayer graphene. This is similar to the case of bilayer graphene, where the band gap creates bands of energy in which no tunneling can occur.

C.3 Density of states and occupation of levels

There are several ways to write the density of states; here, I will use

$$\rho_s = \frac{g_v}{2\pi} k_s \left| \frac{dk_s}{dE} \right|, \quad (\text{C.11})$$

summing over spin states and the conduction and valence bands to get the total density of states. Using Eq. (C.9) we write

$$\frac{dk_s}{dE} = \frac{2E - s\lambda}{\hbar v \sqrt{(2E - s\lambda)^2 - (\Delta - s\lambda)^2}}. \quad (\text{C.12})$$

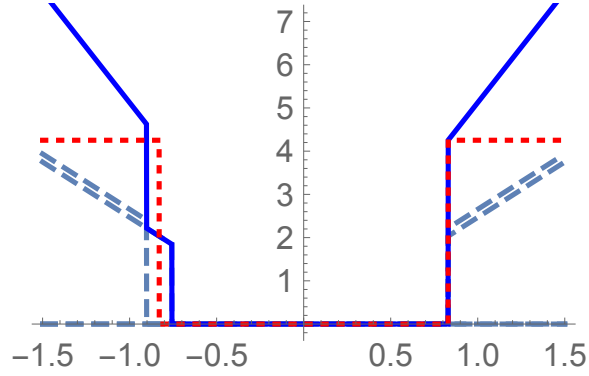


Figure C.2: Total density of states versus energy in units of eV (solid, blue). Dashed blue lines indicate separate spin contributions. Red dotted lines show the equivalent density of states from the parabolic effective mass approximation in Section 1.

which gives

$$k_s \left| \frac{dk_s}{dE} \right| = \frac{|2E - s\lambda|}{2\pi(\hbar v)^2}. \quad (\text{C.13})$$

In the conduction band, $E > 0$ (also $E > \Delta/2 \gg \lambda$) and the density of electron states (summing over spin) takes the form

$$\rho_e(E) = \frac{2}{\pi} \frac{E}{(\hbar v)^2} \Theta(E - \Delta/2). \quad (\text{C.14})$$

Due to the splitting of hole bands, there are two terms for the hole density of states,

$$\rho_h(E) = \frac{1}{2\pi(\hbar v)^2} \{ |2E - \lambda| \Theta(-\Delta/2 + \lambda - E) + |2E + \lambda| \Theta(-\Delta/2 - \lambda - E) \}. \quad (\text{C.15})$$

The total density of states is the sum of the electron and hole parts $\rho = \rho_e + \rho_h$. There is a notable step in the hole density of states due to spin-orbit splitting. In Fig. C.2, we see that this effect is quite distinct from the equivalent density of states one gets in the effective mass approximation, as shown by the red, dashed line which exhibits a simple step-function behavior. This feature may be important for the TFET device since such operation always involves tunneling from one conduction band to the valence band in the other layer.

For the electrostatics of TMD devices we will need carrier densities for each TMD layer. The electron density is obtained by integrating Eq. (C.14) with the Fermi

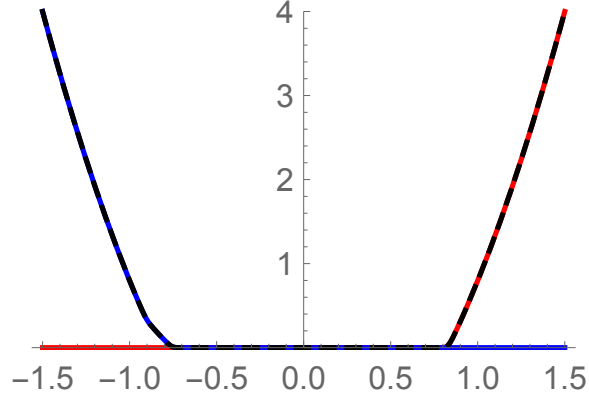


Figure C.3: Total carrier density (black, dashed line) $n + p$ (nm^{-2}) as a function of Fermi level (eV). Separate electron (red, solid) and hole (blue, solid) densities are shown as well.

occupation function,

$$\begin{aligned}
 n &= \frac{2}{\pi(\hbar v)^2} \int_{\Delta/2}^{\infty} dE \frac{E}{1 + e^{(E-\mu)/kT}} \\
 &= \frac{\Delta}{\pi(\hbar v)^2} kT \ln(1 + e^{(\mu-\Delta/2)/kT}) - \frac{2}{\pi} \left(\frac{kT}{\hbar v} \right)^2 \text{Li}_2(-e^{(\mu-\Delta/2)/kT}). \quad (\text{C.16})
 \end{aligned}$$

The hole density is obtained similarly, albeit with a few more terms,

$$\begin{aligned}
 p &= \frac{1}{2\pi(\hbar v)^2} \left\{ \int_{-\infty}^{-\Delta/2+\lambda} dE \frac{|2E - \lambda|}{1 + e^{(\mu-E)/kT}} + \int_{-\infty}^{-\Delta/2-\lambda} dE \frac{|2E + \lambda|}{1 + e^{(\mu-E)/kT}} \right\} \\
 &= \frac{(\Delta - \lambda)}{2\pi(\hbar v)^2} kT \ln(1 + e^{(-\Delta/2+\lambda-\mu)/kT}) - \frac{1}{\pi} \left(\frac{kT}{\hbar v} \right)^2 \text{Li}_2(-e^{(-\Delta/2+\lambda-\mu)/kT}) \\
 &\quad + \frac{(\Delta + \lambda)}{2\pi(\hbar v)^2} kT \ln(1 + e^{(-\Delta/2+\lambda+\mu)/kT}) - \frac{1}{\pi} \left(\frac{kT}{\hbar v} \right)^2 \text{Li}_2(-e^{(-\Delta/2+\lambda+\mu)/kT}). \quad (\text{C.17})
 \end{aligned}$$

The total carrier density $n + p$ is shown as a function of Fermi level in Fig. C.3, with a kink caused by the jumps in hole density for negative Fermi energies. Total charge is defined as $q = -en + ep$.

Bibliography

- [1] Sergio C. de la Barrera, Qin Gao, and Randall M. Feenstra. Theory of graphene–insulator–graphene tunnel junctions. *J. Vac. Sci. Technol.*, 32(4):04E101, April 2014. doi:[10.1116/1.4871760](https://doi.org/10.1116/1.4871760).
- [2] T. Roy, L. Liu, S. de la Barrera, B. Chakrabarti, Z. R. Hesabi, C. A. Joiner, R. M. Feenstra, G. Gu, and E. M. Vogel. Tunneling characteristics in chemical vapor deposited graphene–hexagonal boron nitride–graphene junctions. *Appl. Phys. Lett.*, 104(12):123506, March 2014. doi:[10.1063/1.4870073](https://doi.org/10.1063/1.4870073).
- [3] Sergio C. de la Barrera and Randall M. Feenstra. Theory of resonant tunneling in bilayer-graphene/hexagonal-boron-nitride heterostructures. *Appl. Phys. Lett.*, 106(9):093115, March 2015. doi:[10.1063/1.4914324](https://doi.org/10.1063/1.4914324).
- [4] Devashish P. Gopalan, Patrick C. Mende, Sergio C. de la Barrera, Shonali Dhingra, Jun Li, Kehao Zhang, Nicholas A. Simonson, Joshua A. Robinson, Ning Lu, Qingxiao Wang, Moon J. Kim, Brian D’Urso, and Randall M. Feenstra. Formation of hexagonal boron nitride on graphene-covered copper surfaces. *J. Mater. Res.*, 31:945–958, April 2016. doi:[10.1557/jmr.2016.82](https://doi.org/10.1557/jmr.2016.82).
- [5] Yu-Chuan Lin, Jun Li, Sergio C. de la Barrera, Sarah M. Eichfeld, Yifan Nie, Rafik Addou, Patrick C. Mende, Robert M. Wallace, Kyeongjae Cho, Randall M. Feenstra, and Joshua A. Robinson. Tuning electronic transport in epitaxial graphene-based van der Waals heterostructures. *Nanoscale*, 8:8947–8954, April 2016. doi:[10.1039/C6NR01902A](https://doi.org/10.1039/C6NR01902A).
- [6] Sergio C. de la Barrera, Yu-Chuan Lin, Sarah M. Eichfeld, Joshua A. Robinson, Qin Gao, Michael Widom, and Randall M. Feenstra. Thickness characterization of atomically thin WSe₂ on epitaxial graphene by low-energy electron reflectivity oscillations. *J. Vac. Sci. Technol. B*, 34(4):04J106, July 2016. doi:[10.1116/1.4954642](https://doi.org/10.1116/1.4954642).
- [7] K. S. Novoselov, A. K. Geim, S. V. Morozov, D. Jiang, Y. Zhang, S. V. Dubonos, I. V. Grigorieva, and A. A. Firsov. Electric field effect in atomically thin carbon films. *Science*, 306(5696):666–669, October 2004. doi:[10.1126/science.1102896](https://doi.org/10.1126/science.1102896).

- [8] R. Peierls. Quelques propriétés typiques des corps solides. *Ann. Inst. Henri Poincaré*, 5(3):177–222, 1935.
- [9] L. D. Landau. Zur theorie der phasenumwandlungen II. *Phys. Z. Sowjetunion*, 11:26–35, 1937.
- [10] N. D. Mermin. Crystalline order in two dimensions. *Phys. Rev.*, 176:250–254, December 1968. doi:[10.1103/PhysRev.176.250](https://doi.org/10.1103/PhysRev.176.250).
- [11] Claire Berger, Zhimin Song, Tianbo Li, Xuebin Li, Asmerom Y. Ogbazghi, Rui Feng, Zhenting Dai, Alexei N. Marchenkov, Edward H. Conrad, Phillip N. First, and Walt A. de Heer. Ultrathin epitaxial graphite: 2D electron gas properties and a route toward graphene-based nanoelectronics. *J. Phys. Chem. B*, 108(52):19912–19916, December 2004. doi:[10.1021/jp040650f](https://doi.org/10.1021/jp040650f).
- [12] K. S. Novoselov, D. Jiang, F. Schedin, T. J. Booth, V. V. Khotkevich, S. V. Morozov, and A. K. Geim. Two-dimensional atomic crystals. *Proc. Natl. Acad. Sci. U. S. A.*, 102(30):10451–10453, July 2005. doi:[10.1073/pnas.0502848102](https://doi.org/10.1073/pnas.0502848102).
- [13] D. Pacilé, J. C. Meyer, Ç. Ö. Girit, and A. Zettl. The two-dimensional phase of boron nitride: Few-atomic-layer sheets and suspended membranes. *Appl. Phys. Lett.*, 92(13):133107, 2008. doi:[10.1063/1.2903702](https://doi.org/10.1063/1.2903702).
- [14] Kin Fai Mak, Changgu Lee, James Hone, Jie Shan, and Tony F. Heinz. Atomically thin MoS₂: A new direct-gap semiconductor. *Phys. Rev. Lett.*, 105:136805, September 2010. doi:[10.1103/PhysRevLett.105.136805](https://doi.org/10.1103/PhysRevLett.105.136805).
- [15] C. R. Dean, A. F. Young, I. Meric, C. Lee, L. Wang, S. Sorgenfrei, K. Watanabe, T. Taniguchi, P. Kim, K. L. Shepard, and J. Hone. Boron nitride substrates for high-quality graphene electronics. *Nature Nanotech.*, 5(10):722–726, October 2010. doi:[10.1038/nnano.2010.172](https://doi.org/10.1038/nnano.2010.172).
- [16] Qing Hua Wang, Kouros Kalantar-Zadeh, Andras Kis, Jonathan N. Coleman, and Michael S. Strano. Electronics and optoelectronics of two-dimensional transition metal dichalcogenides. *Nature Nanotech.*, 7(11):699–712, November 2012. doi:[10.1038/nnano.2012.193](https://doi.org/10.1038/nnano.2012.193).
- [17] R. P. Feynman. There’s plenty of room at the bottom. *Engineering and Science*, 23:22–36, February 1960. Lecture given to the American Physical Society at the California Institute of Technology on 29 December 1959.
- [18] P. R. Wallace. The band theory of graphite. *Phys. Rev.*, 71:622–634, May 1947. doi:[10.1103/PhysRev.71.622](https://doi.org/10.1103/PhysRev.71.622).
- [19] A. H. Castro Neto, F. Guinea, N. M. R. Peres, K. S. Novoselov, and A. K. Geim. The electronic properties of graphene. *Rev. Mod. Phys.*, 81:109–162, January 2009. doi:[10.1103/RevModPhys.81.109](https://doi.org/10.1103/RevModPhys.81.109).

- [20] Gordon W. Semenoff. Condensed-matter simulation of a three-dimensional anomaly. *Phys. Rev. Lett.*, 53:2449–2452, December 1984. doi:[10.1103/PhysRevLett.53.2449](https://doi.org/10.1103/PhysRevLett.53.2449).
- [21] Kenji Watanabe, Takashi Taniguchi, and Hisao Kanda. Direct-bandgap properties and evidence for ultraviolet lasing of hexagonal boron nitride single crystal. *Nature Mater.*, 3(6):404–409, 2004. doi:[10.1038/nmat1134](https://doi.org/10.1038/nmat1134).
- [22] Jiamin Xue, Javier Sanchez-Yamagishi, Danny Bulmash, Philippe Jacquod, Aparna Deshpande, K. Watanabe, T. Taniguchi, Pablo Jarillo-Herrero, and Brian J. LeRoy. Scanning tunnelling microscopy and spectroscopy of ultra-flat graphene on hexagonal boron nitride. *Nature Mater.*, 10(4):282–285, April 2011. doi:[10.1038/nmat2968](https://doi.org/10.1038/nmat2968).
- [23] L. Wang, I. Meric, P. Y. Huang, Q. Gao, Y. Gao, H. Tran, T. Taniguchi, K. Watanabe, L. M. Campos, D. A. Muller, J. Guo, P. Kim, J. Hone, K. L. Shepard, and C. R. Dean. One-dimensional electrical contact to a two-dimensional material. *Science*, 342(6158):614–617, November 2013. doi:[10.1126/science.1244358](https://doi.org/10.1126/science.1244358).
- [24] A. Seabaugh and R. Lake. Tunnel diodes. In George L. Trigg, editor, *Encyclop. Appl. Phys.*, volume 22, pages 335–359. Wiley-VCH, New York, 1998.
- [25] Leo Esaki. New phenomenon in narrow germanium p - n junctions. *Phys. Rev.*, 109:603–604, January 1958. doi:[10.1103/PhysRev.109.603](https://doi.org/10.1103/PhysRev.109.603).
- [26] J. A. Simmons, M. A. Blount, J. S. Moon, S. K. Lyo, W. E. Baca, J. R. Wendt, J. L. Reno, and M. J. Hafich. Planar quantum transistor based on 2D–2D tunneling in double quantum well heterostructures. *J. Appl. Phys.*, 84(10):5626–5634, 1998. doi:[dx.doi.org/10.1063/1.368610](https://doi.org/dx.doi.org/10.1063/1.368610).
- [27] J. P. Eisenstein, L. N. Pfeiffer, and K. W. West. Field-induced resonant tunneling between parallel two-dimensional electron systems. *Appl. Phys. Lett.*, 58(14):1497–1499, 1991. doi:[10.1063/1.105157](https://doi.org/10.1063/1.105157).
- [28] J. P. Eisenstein, T. J. Gramila, L. N. Pfeiffer, and K. W. West. Probing a two-dimensional Fermi surface by tunneling. *Phys. Rev. B*, 44:6511–6514, September 1991. doi:[10.1103/PhysRevB.44.6511](https://doi.org/10.1103/PhysRevB.44.6511).
- [29] Sanjay K. Banerjee, Leonard F. Register, Emanuel Tutuc, Dharmendar Reddy, and Allan H. MacDonald. Bilayer pseudospin field-effect transistor (BiSFET): A proposed new logic device. *IEEE Elec. Dev. Lett.*, 30(2):158–160, February 2009. doi:[10.1109/LED.2008.2009362](https://doi.org/10.1109/LED.2008.2009362).

- [30] D. Basu, L. F. Register, Dharmendar Reddy, A. H. MacDonald, and S. K. Banerjee. Tight-binding study of electron-hole pair condensation in graphene bilayers: Gate control and system-parameter dependence. *Phys. Rev. B*, 82:075409, August 2010. doi:[10.1103/PhysRevB.82.075409](https://doi.org/10.1103/PhysRevB.82.075409).
- [31] L. Britnell, R. V. Gorbachev, A. K. Geim, L. A. Ponomarenko, A. Mishchenko, M. T. Greenaway, T. M. Fromhold, K. S. Novoselov, and L. Eaves. Resonant tunnelling and negative differential conductance in graphene transistors. *Nat. Commun.*, 4:1794, 2013. doi:[10.1038/ncomms2817](https://doi.org/10.1038/ncomms2817).
- [32] A. Mishchenko, J. S. Tu, Y. Cao, R. V. Gorbachev, J. R. Wallbank, M. T. Greenaway, V. E. Morozov, S. V. Morozov, M. J. Zhu, S. L. Wong, F. Withers, C. R. Woods, Y.-J. Kim, K. Watanabe, T. Taniguchi, E. E. Vdovin, O. Makarovskiy, T. M. Fromhold, V. I. Fal'ko, A. K. Geim, L. Eaves, and K. S. Novoselov. Twist-controlled resonant tunnelling in graphene/boron nitride/graphene heterostructures. *Nature Nanotech.*, 9(10):808–813, 2014. doi:[10.1038/nnano.2014.187](https://doi.org/10.1038/nnano.2014.187).
- [33] Babak Fallahazad, Kayoung Lee, Sangwoo Kang, Jiamin Xue, Stefano Larentis, Christopher Corbet, Kyoungwan Kim, Hema C. P. Movva, Takashi Taniguchi, Kenji Watanabe, Leonard F. Register, Sanjay K. Banerjee, and Emanuel Tutuc. Gate-tunable resonant tunneling in double bilayer graphene heterostructures. *Nano Lett.*, 15(1):428–433, 2015. doi:[10.1021/nl503756y](https://doi.org/10.1021/nl503756y).
- [34] Sangwoo Kang, Babak Fallahazad, Kayoung Lee, Hema Movva, Kyoungwan Kim, Chris M. Corbet, Takashi Taniguchi, Kenji Watanabe, Luigi Colombo, Leonard F. Register, Emanuel Tutuc, and Sanjay K. Banerjee. Bilayer graphene–hexagonal boron nitride heterostructure negative differential resistance interlayer tunnel FET. *IEEE Elec. Dev. Lett.*, 36(4):405–407, April 2015. doi:[10.1109/LED.2015.2398737](https://doi.org/10.1109/LED.2015.2398737).
- [35] E. Bauer. Low energy electron microscopy. *Rep. Prog. Phys.*, 57(9):895, 1994. doi:[10.1088/0034-4885/57/9/002](https://doi.org/10.1088/0034-4885/57/9/002).
- [36] E. Bauer. Interaction of slow electrons with surfaces. *J. Vac. Sci. Technol.*, 7(1):3–12, 1970. doi:[10.1116/1.1315823](https://doi.org/10.1116/1.1315823).
- [37] G. Binnig, K. H. Frank, H. Fuchs, N. Garcia, B. Reihl, H. Rohrer, F. Salvan, and A. R. Williams. Tunneling spectroscopy and inverse photoemission: Image and field states. *Phys. Rev. Lett.*, 55:991–994, August 1985. doi:[10.1103/PhysRevLett.55.991](https://doi.org/10.1103/PhysRevLett.55.991).
- [38] A. Selloni, P. Carnevali, E. Tosatti, and C. D. Chen. Voltage-dependent scanning-tunneling microscopy of a crystal surface: Graphite. *Phys. Rev. B*, 31:2602–2605, February 1985. doi:[10.1103/PhysRevB.31.2602](https://doi.org/10.1103/PhysRevB.31.2602).

- [39] Joseph A. Stroscio, R. M. Feenstra, and A. P. Fein. Electronic structure of the Si(111) 2×1 surface by scanning-tunneling microscopy. *Phys. Rev. Lett.*, 57: 2579–2582, November 1986. doi:[10.1103/PhysRevLett.57.2579](https://doi.org/10.1103/PhysRevLett.57.2579).
- [40] W. Świąch, B. Rausenberger, W. Engel, A. M. Bradshaw, and E. Zeitler. In-situ studies of heterogeneous reactions using mirror electron microscopy. *Surf. Sci.*, 294(3):297–307, June 1993. doi:[10.1016/0039-6028\(93\)90116-2](https://doi.org/10.1016/0039-6028(93)90116-2).
- [41] Ludwig Reimer and Helmut Kohl. *Transmission Electron Microscopy*, volume 36 of *Springer Series in Optical Sciences*. Springer, Berlin, 4 edition, 1997. doi:[10.1007/978-0-387-40093-8](https://doi.org/10.1007/978-0-387-40093-8).
- [42] J. B. Hannon and R. M. Tromp. Low-energy electron microscopy for nanoscale characterization. In Richard A. Haight, Frances M. Ross, and James B. Hannon, editors, *Handbook of Instrumentation and Techniques for Semiconductor Nanostructure Characterization*, pages 127–181. World Scientific, Singapore, November 2012. doi:[10.1142/9789814322843_0004](https://doi.org/10.1142/9789814322843_0004).
- [43] H. Hibino, H. Kageshima, F. Maeda, M. Nagase, Y. Kobayashi, and H. Yamaguchi. Microscopic thickness determination of thin graphite films formed on SiC from quantized oscillation in reflectivity of low-energy electrons. *Phys. Rev. B*, 77:075413, February 2008. doi:[10.1103/PhysRevB.77.075413](https://doi.org/10.1103/PhysRevB.77.075413).
- [44] C. Virojanadara, M. Syväjarvi, R. Yakimova, L. I. Johansson, A. A. Zakharov, and T. Balasubramanian. Homogeneous large-area graphene layer growth on 6H-SiC(0001). *Phys. Rev. B*, 78:245403, December 2008. doi:[10.1103/PhysRevB.78.245403](https://doi.org/10.1103/PhysRevB.78.245403).
- [45] Peter Sutter, Jerzy T. Sadowski, and Eli Sutter. Graphene on Pt(111): Growth and substrate interaction. *Phys. Rev. B*, 80:245411, December 2009. doi:[10.1103/PhysRevB.80.245411](https://doi.org/10.1103/PhysRevB.80.245411).
- [46] C. Riedl, C. Coletti, T. Iwasaki, A. A. Zakharov, and U. Starke. Quasi-free-standing epitaxial graphene on SiC obtained by hydrogen intercalation. *Phys. Rev. Lett.*, 103:246804, December 2009. doi:[10.1103/PhysRevLett.103.246804](https://doi.org/10.1103/PhysRevLett.103.246804).
- [47] Andrea Locatelli, Kevin R. Knox, Dean Cvetko, Tevfik Onur Montes, Miguel Angel Niño, Shancai Wang, Mehmet B. Yilmaz, Philip Kim, Jr. Richard M. Osgood, and Alberto Morgante. Corrugation in exfoliated graphene: An electron microscopy and diffraction study. *ACS Nano*, 4(8):4879–4889, August 2010. doi:[10.1021/nn101116n](https://doi.org/10.1021/nn101116n).
- [48] R. M. Feenstra, N. Srivastava, Qin Gao, M. Widom, Bogdan Diaconescu, Taisuke Ohta, G. L. Kellogg, J. T. Robinson, and I. V. Vlassiuk. Low-energy electron reflectivity from graphene. *Phys. Rev. B*, 87:041406, January 2013. doi:[10.1103/PhysRevB.87.041406](https://doi.org/10.1103/PhysRevB.87.041406).

- [49] Carlo M. Orofeo, Satoru Suzuki, Hiroyuki Kageshima, and Hiroki Hibino. Growth and low-energy electron microscopy characterization of monolayer hexagonal boron nitride on epitaxial cobalt. *Nano Res.*, 6(5):335–347, 2013. ISSN 1998-0000. doi:[10.1007/s12274-013-0310-1](https://doi.org/10.1007/s12274-013-0310-1).
- [50] Yu-Chuan Lin, Chih-Yuan S. Chang, Ram Krishna Ghosh, Jie Li, Hui Zhu, Rafik Addou, Bogdan Diaconescu, Taisuke Ohta, Xin Peng, Ning Lu, Moon J. Kim, Jeremy T. Robinson, Robert M. Wallace, Theresa S. Mayer, Suman Datta, Lain-Jong Li, and Joshua A. Robinson. Atomically thin heterostructures based on single-layer tungsten diselenide and graphene. *Nano Lett.*, 14(12):6936–6941, December 2014. doi:[10.1021/nl503144a](https://doi.org/10.1021/nl503144a).
- [51] Po-Chun Yeh, Wencan Jin, Nader Zaki, Jens Kunstmann, Daniel Chenet, Ghidewon Arefe, Jerzy T. Sadowski, Jerry I. Dadap, Peter Sutter, James Hone, and Richard M. Osgood, Jr. Direct measurement of the tunable electronic structure of bilayer MoS₂ by interlayer twist. *Nano Lett.*, 16(2):953–959, January 2016. doi:[10.1021/acs.nanolett.5b03883](https://doi.org/10.1021/acs.nanolett.5b03883).
- [52] Yu-Chuan Lin, Ning Lu, Nestor Perea-Lopez, Jie Li, Zhong Lin, Xin Peng, Chia Hui Lee, Ce Sun, Lazaro Calderin, Paul N. Browning, Michael S. Bresnahan, Moon J. Kim, Theresa S. Mayer, Mauricio Terrones, and Joshua A. Robinson. Direct synthesis of van der Waals solids. *ACS Nano*, 8(4):3715–3723, April 2014. doi:[10.1021/nm5003858](https://doi.org/10.1021/nm5003858).
- [53] Sarah M. Eichfeld, Lorraine Hossain, Yu-Chuan Lin, Aleksander F. Piasecki, Benjamin Kupp, A. Glen Birdwell, Robert A. Burke, Ning Lu, Xin Peng, Jie Li, Angelica Azcatl, Stephen McDonnell, Robert M. Wallace, Moon J. Kim, Theresa S. Mayer, Joan M. Redwing, and Joshua A. Robinson. Highly scalable, atomically thin WSe₂ grown via metal-organic chemical vapor deposition. *ACS Nano*, 9(2):2080–2087, January 2015. doi:[10.1021/nm5073286](https://doi.org/10.1021/nm5073286).
- [54] G. Kresse and J. Hafner. *Ab initio* molecular dynamics for liquid metals. *Phys. Rev. B*, 47:558–561, January 1993. doi:[10.1103/PhysRevB.47.558](https://doi.org/10.1103/PhysRevB.47.558).
- [55] G. Kresse and J. Furthmüller. Efficient iterative schemes for *ab initio* total-energy calculations using a plane-wave basis set. *Phys. Rev. B*, 54:11169–11186, October 1996. doi:[10.1103/PhysRevB.54.11169](https://doi.org/10.1103/PhysRevB.54.11169).
- [56] G. Kresse and D. Joubert. From ultrasoft pseudopotentials to the projector augmented-wave method. *Phys. Rev. B*, 59:1758–1775, January 1999. doi:[10.1103/PhysRevB.59.1758](https://doi.org/10.1103/PhysRevB.59.1758).
- [57] John P. Perdew, Kieron Burke, and Matthias Ernzerhof. Generalized gradient

- approximation made simple. *Phys. Rev. Lett.*, 77:3865–3868, October 1996. doi:[10.1103/PhysRevLett.77.3865](https://doi.org/10.1103/PhysRevLett.77.3865).
- John P. Perdew, Kieron Burke, and Matthias Ernzerhof. Generalized gradient approximation made simple [Phys. Rev. Lett. 77, 3865 (1996)]. *Phys. Rev. Lett.*, 78:1396–1396, February 1997. doi:[10.1103/PhysRevLett.78.1396](https://doi.org/10.1103/PhysRevLett.78.1396).
- [58] R. M. Feenstra and M. Widom. Low-energy electron reflectivity from graphene: First-principles computations and approximate models. *Ultramicroscopy*, 130: 101–108, July 2013. ISSN 0304-3991. doi:[10.1016/j.ultramic.2013.02.011](https://doi.org/10.1016/j.ultramic.2013.02.011).
- [59] Qin Gao, Patrick C. Mende, Michael Widom, and Randall M. Feenstra. Inelastic effects in low-energy electron reflectivity of two-dimensional materials. *J. Vac. Sci. Technol. B*, 33(2):02B105, March 2015. doi:[10.1116/1.4903361](https://doi.org/10.1116/1.4903361).
- [60] E. E. Krasovskii, W. Schattke, V. N. Strocov, and R. Claessen. Unoccupied band structure of NbSe₂ by very low-energy electron diffraction: Experiment and theory. *Phys. Rev. B*, 66:235403, December 2002. doi:[10.1103/PhysRevB.66.235403](https://doi.org/10.1103/PhysRevB.66.235403).
- [61] E. E. Krasovskii and V. N. Strocov. Very-low-energy electron diffraction from TiS₂: experiment and *ab initio* theory. *J. Phys. Condens. Matter*, 21(31): 314009, 2009. doi:[10.1088/0953-8984/21/31/314009](https://doi.org/10.1088/0953-8984/21/31/314009).
- [62] J. Ingo Flege, Axel Meyer, Jens Falta, and Eugene E. Krasovskii. Self-limited oxide formation in Ni(111) oxidation. *Phys. Rev. B*, 84:115441, September 2011. doi:[10.1103/PhysRevB.84.115441](https://doi.org/10.1103/PhysRevB.84.115441).
- [63] Yu-Chuan Lin, Ram Krishna Ghosh, Rafik Addou, Ning Lu, Sarah M. Eichfeld, Hui Zhu, Ming-Yang Li, Xin Peng, Moon J. Kim, Lain-Jong Li, Robert M. Wallace, Suman Datta, and Joshua A. Robinson. Atomically thin resonant tunnel diodes built from synthetic van der Waals heterostructures. *Nat. Commun.*, 6: 7311, June 2015. doi:[10.1038/ncomms8311](https://doi.org/10.1038/ncomms8311).
- [64] H. Hibino, H. Kageshima, F. Maeda, M. Nagase, Y. Kobayashi, Y. Kobayashi, and H. Yamaguchi. Thickness determination of graphene layers formed on SiC using low-energy electron microscopy. *e-J. Surf. Sci. Nanotech.*, 6:107–110, 2008. doi:[10.1380/ejssnt.2008.107](https://doi.org/10.1380/ejssnt.2008.107).
- [65] N. Srivastava, Qin Gao, M. Widom, R. M. Feenstra, Shu Nie, K. F. McCarty, and I. V. Vlassiouk. Low-energy electron reflectivity of graphene on copper and other substrates. *Phys. Rev. B*, 87:245414, June 2013. doi:[10.1103/PhysRevB.87.245414](https://doi.org/10.1103/PhysRevB.87.245414).

- [66] M. Posternak, A. Baldereschi, A. J. Freeman, E. Wimmer, and M. Weinert. Prediction of electronic interlayer states in graphite and reinterpretation of alkali bands in graphite intercalation compounds. *Phys. Rev. Lett.*, 50:761–764, March 1983. doi:[10.1103/PhysRevLett.50.761](https://doi.org/10.1103/PhysRevLett.50.761).
- [67] V. M. Silkin, J. Zhao, F. Guinea, E. V. Chulkov, P. M. Echenique, and H. Petek. Image potential states in graphene. *Phys. Rev. B*, 80:121408, September 2009. doi:[10.1103/PhysRevB.80.121408](https://doi.org/10.1103/PhysRevB.80.121408).
- [68] P. Mende. *Growth and surface studies of two-dimensional materials*. PhD thesis, Carnegie Mellon University, 2015.
- [69] Tania Roy, Mahmut Tosun, Xi Cao, Hui Fang, Der-Hsien Lien, Peida Zhao, Yu-Ze Chen, Yu-Lun Chueh, Jing Guo, and Ali Javey. Dual-gated MoS₂/WSe₂ van der Waals tunnel diodes and transistors. *ACS Nano*, 9(2):2071–2079, January 2015. doi:[10.1021/nn507278b](https://doi.org/10.1021/nn507278b).
- [70] Rusen Yan, Sara Fathipour, Yimo Han, Bo Song, Shudong Xiao, Mingda Li, Nan Ma, Vladimir Protasenko, David A. Muller, Debdeep Jena, and Huili Grace Xing. Esaki diodes in van der Waals heterojunctions with broken-gap energy band alignment. *Nano Lett.*, 15(9):5791–5798, July 2015. doi:[10.1021/acs.nanolett.5b01792](https://doi.org/10.1021/acs.nanolett.5b01792).
- [71] Thanasis Georgiou, Rashid Jalil, Branson D. Belle, Liam Britnell, Roman V. Gorbachev, Sergey V. Morozov, Yong-Jin Kim, Ali Gholinia, Sarah J. Haigh, Oleg Makarovskiy, et al. Vertical field-effect transistor based on graphene-WS₂ heterostructures for flexible and transparent electronics. *Nature Nanotech.*, 8(2):100–103, February 2013. doi:[10.1038/nnano.2012.224](https://doi.org/10.1038/nnano.2012.224).
- [72] L. Britnell, R. M. Ribeiro, A. Eckmann, R. Jalil, B. D. Belle, A. Mishchenko, Y.-J. Kim, R. V. Gorbachev, T. Georgiou, S. V. Morozov, A. N. Grigorenko, A. K. Geim, C. Casiraghi, A. H. Castro Neto, and K. S. Novoselov. Strong light-matter interactions in heterostructures of atomically thin films. *Science*, 340(6138):1311–1314, June 2013. doi:[10.1126/science.1235547](https://doi.org/10.1126/science.1235547).
- [73] Woo Jong Yu, Yuan Liu, Hailong Zhou, Anxiang Yin, Zheng Li, Yu Huang, and Xiangfeng Duan. Highly efficient gate-tunable photocurrent generation in vertical heterostructures of layered materials. *Nature Nanotech.*, 8(12):952–958, December 2013. doi:[10.1038/nnano.2013.219](https://doi.org/10.1038/nnano.2013.219).
- [74] Chul-Ho Lee, Gwan-Hyoung Lee, Arend M. van der Zande, Wenchao Chen, Yilei Li, Minyong Han, Xu Cui, Ghidewon Arefe, Colin Nuckolls, Tony F. Heinz, Jing Guo, James Hone, and Philip Kim. Atomically thin p–n junctions with van der Waals heterointerfaces. *Nature Nanotech.*, 9(9):676–681, September 2014. doi:[10.1038/nnano.2014.150](https://doi.org/10.1038/nnano.2014.150).

- [75] Yumeng Shi, Wu Zhou, Ang-Yu Lu, Wenjing Fang, Yi-Hsien Lee, Allen Long Hsu, Soo Min Kim, Ki Kang Kim, Hui Ying Yang, Lain-Jong Li, Juan-Carlos Idrobo, and Jing Kong. van der Waals epitaxy of MoS₂ layers using graphene as growth templates. *Nano Lett.*, 12(6):2784–2791, June 2012. doi:[10.1021/nl204562j](https://doi.org/10.1021/nl204562j).
- [76] Zheng Liu, Li Song, Shizhen Zhao, Jiaqi Huang, Lulu Ma, Jiangnan Zhang, Jun Lou, and Pulickel M. Ajayan. Direct growth of graphene/hexagonal boron nitride stacked layers. *Nano Lett.*, 11(5):2032–2037, May 2011. doi:[10.1021/nl200464j](https://doi.org/10.1021/nl200464j).
- [77] Silvan Roth, Fumihiko Matsui, Thomas Greber, and Jürg Osterwalder. Chemical vapor deposition and characterization of aligned and incommensurate graphene/hexagonal boron nitride heterostack on Cu(111). *Nano Lett.*, 13(6):2668–2675, June 2013. doi:[10.1021/nl400815w](https://doi.org/10.1021/nl400815w).
- [78] Wei Yang, Guorui Chen, Zhiwen Shi, Cheng-Cheng Liu, Lianchang Zhang, Guibai Xie, Meng Cheng, Duoming Wang, Rong Yang, Dongxia Shi, Kenji Watanabe, Takashi Taniguchi, Yugui Yao, Yuanbo Zhang, and Guangyu Zhang. Epitaxial growth of single-domain graphene on hexagonal boron nitride. *Nature Mater.*, 12(9):792–797, September 2013. doi:[10.1038/nmat3695](https://doi.org/10.1038/nmat3695).
- [79] Xuesong Li, Weiwei Cai, Jinho An, Seyoung Kim, Junghyo Nah, Dongxing Yang, Richard Piner, Aruna Velamakanni, Inhwa Jung, Emanuel Tutuc, Sanjay K. Banerjee, Luigi Colombo, and Rodney S. Ruoff. Large-area synthesis of high-quality and uniform graphene films on copper foils. *Science*, 324(5932):1312–1314, June 2009. doi:[10.1126/science.1171245](https://doi.org/10.1126/science.1171245).
- [80] S. Marchini, S. Günther, and J. Winterlin. Scanning tunneling microscopy of graphene on Ru(0001). *Phys. Rev. B*, 76:075429, August 2007. doi:[10.1103/PhysRevB.76.075429](https://doi.org/10.1103/PhysRevB.76.075429).
- [81] Johann Coraux, Alpha T. N’Diaye, Carsten Busse, and Thomas Michely. Structural coherency of graphene on Ir(111). *Nano Lett.*, 8(2):565–570, February 2008. doi:[10.1021/nl0728874](https://doi.org/10.1021/nl0728874).
- [82] Peter W. Sutter, Jan-Ingo Flege, and Eli A. Sutter. Epitaxial graphene on ruthenium. *Nature Mater.*, 7(5):406–411, May 2008. doi:[10.1038/nmat2166](https://doi.org/10.1038/nmat2166).
- [83] Xuesong Li, Weiwei Cai, Luigi Colombo, and Rodney S. Ruoff. Evolution of graphene growth on Ni and Cu by carbon isotope labeling. *Nano Lett.*, 9(12):4268–4272, December 2009. doi:[10.1021/nl902515k](https://doi.org/10.1021/nl902515k).
- [84] Claire Berger, Zhimin Song, Xuebin Li, Xiaosong Wu, Nate Brown, Cécile Naud, Didier Mayou, Tianbo Li, Joanna Hass, Alexei N. Marchenkov, Edward H.

- Conrad, Phillip N. First, and Walt A. de Heer. Electronic confinement and coherence in patterned epitaxial graphene. *Science*, 312(5777):1191–1196, May 2006. doi:[10.1126/science.1125925](https://doi.org/10.1126/science.1125925).
- [85] Konstantin V. Emtsev, Aaron Bostwick, Karsten Horn, Johannes Jobst, Gary L. Kellogg, Lothar Ley, Jessica L. McChesney, Taisuke Ohta, Sergey A. Reshanov, Jonas Röhrli, Eli Rotenberg, Andreas K. Schmid, Daniel Waldmann, Heiko B. Weber, and Thomas Seyller. Towards wafer-size graphene layers by atmospheric pressure graphitization of silicon carbide. *Nature Mater.*, 8(3):203–207, March 2009. doi:[10.1038/nmat2382](https://doi.org/10.1038/nmat2382).
- [86] Suresh Vishwanath, Xinyu Liu, Sergei Rouvimov, Patrick C. Mende, Angelica Azcatl, Stephen McDonnell, Robert M. Wallace, Randall M. Feenstra, Jacek K. Furdyna, Debdeep Jena, and Huili Grace Xing. Comprehensive structural and optical characterization of MBE grown MoSe₂ on graphite, CaF₂ and graphene. *2D Mater.*, 2(2):024007, May 2015. doi:[10.1088/2053-1583/2/2/024007](https://doi.org/10.1088/2053-1583/2/2/024007).
- [87] Joshua A. Robinson, Matthew Hollander, Michael LaBella, III, Kathleen A. Trumbull, Randall Cavalero, and David W. Snyder. Epitaxial graphene transistors: Enhancing performance via hydrogen intercalation. *Nano Lett.*, 11(9):3875–3880, September 2011. doi:[10.1021/nl2019855](https://doi.org/10.1021/nl2019855).
- [88] Taisuke Ohta, Aaron Bostwick, J. L. McChesney, Thomas Seyller, Karsten Horn, and Eli Rotenberg. Interlayer interaction and electronic screening in multilayer graphene investigated with angle-resolved photoemission spectroscopy. *Phys. Rev. Lett.*, 98:206802, May 2007. doi:[10.1103/PhysRevLett.98.206802](https://doi.org/10.1103/PhysRevLett.98.206802).
- [89] Sergey Kopylov, Alexander Tzalenchuk, Sergey Kubatkin, and Vladimir I. Fal'ko. Charge transfer between epitaxial graphene and silicon carbide. *Appl. Phys. Lett.*, 97(11):112109, 2010. doi:[10.1063/1.3487782](https://doi.org/10.1063/1.3487782).
- [90] J. Ristein, S. Mammadov, and Th. Seyller. Origin of doping in quasi-free-standing graphene on silicon carbide. *Phys. Rev. Lett.*, 108:246104, June 2012. doi:[10.1103/PhysRevLett.108.246104](https://doi.org/10.1103/PhysRevLett.108.246104).
- [91] Samir Mammadov, Jürgen Ristein, Roland J. Koch, Markus Ostler, Christian Raidel, Martina Wanke, Remigijus Vasiliauskas, Rositza Yakimova, and Thomas Seyller. Polarization doping of graphene on silicon carbide. *2D Mater.*, 1(3):035003, 2014. doi:[10.1088/2053-1583/1/3/035003](https://doi.org/10.1088/2053-1583/1/3/035003).
- [92] D. M. Ceperley and B. J. Alder. Ground state of the electron gas by a stochastic method. *Phys. Rev. Lett.*, 45:566–569, August 1980. doi:[10.1103/PhysRevLett.45.566](https://doi.org/10.1103/PhysRevLett.45.566).

- [93] Matthew J. Hollander, Ashish Agrawal, Michael S. Bresnehan, Michael LaBella, Kathleen A. Trumbull, Randal Cavalero, David W. Snyder, Suman Datta, and Joshua A. Robinson. Heterogeneous integration of hexagonal boron nitride on bilayer quasi-free-standing epitaxial graphene and its impact on electrical transport properties. *Phys. Status Solidi A*, 210(6):1062–1070, June 2013. ISSN 1862-6319. doi:[10.1002/pssa.201228683](https://doi.org/10.1002/pssa.201228683).
- [94] Young-Jun Yu, Yue Zhao, Sunmin Ryu, Louis E. Brus, Kwang S. Kim, and Philip Kim. Tuning the graphene work function by electric field effect. *Nano Lett.*, 9(10):3430–3434, October 2009. doi:[10.1021/nl901572a](https://doi.org/10.1021/nl901572a).
- [95] Gui-Bin Liu, Wen-Yu Shan, Yugui Yao, Wang Yao, and Di Xiao. Three-band tight-binding model for monolayers of group-VIB transition metal dichalcogenides. *Phys. Rev. B*, 88:085433, August 2013. doi:[10.1103/PhysRevB.88.085433](https://doi.org/10.1103/PhysRevB.88.085433).
- [96] Edward McCann and Mikito Koshino. The electronic properties of bilayer graphene. *Rep. Prog. Phys.*, 76(5):056503, May 2013. doi:[10.1088/0034-4885/76/5/056503](https://doi.org/10.1088/0034-4885/76/5/056503).
- [97] Mingda (Oscar) Li, David Esseni, Gregory Snider, Debdeep Jena, and Huili Grace Xing. Single particle transport in two-dimensional heterojunction interlayer tunneling field effect transistor. *J. Appl. Phys.*, 115(7):074508, 2014. doi:[10.1063/1.4866076](https://doi.org/10.1063/1.4866076).
- [98] Yufeng Liang, Shouting Huang, Ryan Soklaski, and Li Yang. Quasiparticle band-edge energy and band offsets of monolayer of molybdenum and tungsten chalcogenides. *Appl. Phys. Lett.*, 103(4):042106, 2013. doi:[10.1063/1.4816517](https://doi.org/10.1063/1.4816517).
- [99] Keliang He, Nardeep Kumar, Liang Zhao, Zefang Wang, Kin Fai Mak, Hui Zhao, and Jie Shan. Tightly bound excitons in monolayer WSe₂. *Phys. Rev. Lett.*, 113:026803, July 2014. doi:[10.1103/PhysRevLett.113.026803](https://doi.org/10.1103/PhysRevLett.113.026803).
- [100] Chendong Zhang, Yuxuan Chen, Amber Johnson, Ming-Yang Li, Lain-Jong Li, Patrick C. Mende, Randall M. Feenstra, and Chih-Kang Shih. Probing critical point energies of transition metal dichalcogenides: Surprising indirect gap of single layer WSe₂. *Nano Lett.*, 15(10):6494–6500, October 2015. doi:[10.1021/acs.nanolett.5b01968](https://doi.org/10.1021/acs.nanolett.5b01968).
- [101] Seung Min Song, Jong Kyung Park, One Jae Sul, and Byung Jin Cho. Determination of work function of graphene under a metal electrode and its role in contact resistance. *Nano Lett.*, 12(8):3887–3892, August 2012. doi:[10.1021/nl300266p](https://doi.org/10.1021/nl300266p).

- [102] Jong-Hun Kim, Jin Heui Hwang, Joonki Suh, Sefaattin Tongay, Sangku Kwon, C. C. Hwang, Junqiao Wu, and Jeong Young Park. Work function engineering of single layer graphene by irradiation-induced defects. *Appl. Phys. Lett.*, 103(17):171604, 2013. doi:[10.1063/1.4826642](https://doi.org/10.1063/1.4826642).
- [103] Jun Kang, Sefaattin Tongay, Jian Zhou, Jingbo Li, and Junqiao Wu. Band offsets and heterostructures of two-dimensional semiconductors. *Appl. Phys. Lett.*, 102(1):012111, 2013. doi:[10.1063/1.4774090](https://doi.org/10.1063/1.4774090).
- [104] Hongjun Liu, Lu Jiao, Fang Yang, Yuan Cai, Xianxin Wu, Wingkin Ho, Chunlei Gao, Jinfeng Jia, Ning Wang, Heng Fan, Wang Yao, and Maohai Xie. Dense network of one-dimensional midgap metallic modes in monolayer MoSe₂ and their spatial undulations. *Phys. Rev. Lett.*, 113:066105, August 2014. doi:[10.1103/PhysRevLett.113.066105](https://doi.org/10.1103/PhysRevLett.113.066105).
- [105] Ossi Lehtinen, Hannu-Pekka Komsa, Artem Pulkin, Michael Brian Whitwick, Ming-Wei Chen, Tibor Lehnert, Michael J. Mohn, Oleg V. Yazyev, Andras Kis, Ute Kaiser, and Arkady V. Krasheninnikov. Atomic scale microstructure and properties of Se-deficient two-dimensional MoSe₂. *ACS Nano*, 9(3):3274–3283, 2015. doi:[10.1021/acsnano.5b00410](https://doi.org/10.1021/acsnano.5b00410).
- [106] Horacio Coy Diaz, Yujing Ma, Redhouane Chaghi, and Matthias Batzill. High density of (pseudo) periodic twin-grain boundaries in molecular beam epitaxy-grown van der waals heterostructure: MoTe₂/MoS₂. *Appl. Phys. Lett.*, 108(19):191606, 2016. doi:[10.1063/1.4949559](https://doi.org/10.1063/1.4949559).
- [107] Supriyo Datta. Nanoscale device modeling: the Green’s function method. *Superlattice. Microst.*, 28(4):253–278, October 2000. doi:[10.1006/spmi.2000.0920](https://doi.org/10.1006/spmi.2000.0920).
- [108] J. Bardeen. Tunnelling from a many-particle point of view. *Phys. Rev. Lett.*, 6:57–59, January 1961. doi:[10.1103/PhysRevLett.6.57](https://doi.org/10.1103/PhysRevLett.6.57).
- [109] J. Tersoff and D. R. Hamann. Theory of the scanning tunneling microscope. *Phys. Rev. B*, 31:805–813, January 1985. doi:[10.1103/PhysRevB.31.805](https://doi.org/10.1103/PhysRevB.31.805).
- [110] R. M. Feenstra, Debdeep Jena, and Gong Gu. Single-particle tunneling in doped graphene-insulator-graphene junctions. *J. Appl. Phys.*, 111(4):043711, February 2012. doi:[dx.doi.org/10.1063/1.3686639](https://doi.org/10.1063/1.3686639).
- [111] Pei Zhao, Randall M Feenstra, Gong Gu, and Debdeep Jena. SymFET: A proposed symmetric graphene tunneling field effect transistor. In *Device Research Conference (DRC), 2012 70th Annual*, pages 33–34. IEEE, June 2012. doi:[10.1109/DRC.2012.6257006](https://doi.org/10.1109/DRC.2012.6257006).

- [112] L. Britnell, R. V. Gorbachev, R. Jalil, B. D. Belle, F. Schedin, A. Mishchenko, T. Georgiou, M. I. Katsnelson, L. Eaves, S. V. Morozov, N. M. R. Peres, J. Leist, A. K. Geim, K. S. Novoselov, and L. A. Ponomarenko. Field-effect tunneling transistor based on vertical graphene heterostructures. *Science*, 335(6071):947–950, 2012. doi:[10.1126/science.1218461](https://doi.org/10.1126/science.1218461).
- [113] T. Roy, Z. R. Hesabi, C. A. Joiner, A. Fujimoto, and E. M. Vogel. Barrier engineering for double layer CVD graphene tunnel FETs. *Microelectron. Eng.*, 109:117–119, September 2013. doi:[10.1016/j.mee.2013.02.090](https://doi.org/10.1016/j.mee.2013.02.090).
- [114] S. Bala Kumar, Gyungseon Seol, and Jing Guo. Modeling of a vertical tunneling graphene heterojunction field-effect transistor. *Appl. Phys. Lett.*, 101(3):033503, July 2012. doi:[10.1063/1.4737394](https://doi.org/10.1063/1.4737394).
- [115] Berardi Sensale-Rodriguez. Graphene-insulator-graphene active plasmonic terahertz devices. *Appl. Phys. Lett.*, 103(12):123109, 2013. doi:[10.1063/1.4821221](https://doi.org/10.1063/1.4821221).
- [116] V. Ryzhii, A. Satou, T. Otsuji, M. Ryzhii, V. Mitin, and M. S. Shur. Dynamic effects in double graphene-layer structures with inter-layer resonant-tunnelling negative conductivity. *J. Phys. D*, 46(31):315107, 2013. doi:[10.1088/0022-3727/46/31/315107](https://doi.org/10.1088/0022-3727/46/31/315107).
- [117] C. B. Duke. *Tunneling in solids*. Academic, New York, 1969.
- [118] Alex D. Gottlieb and Lisa Wesoloski. Bardeen’s tunnelling theory as applied to scanning tunnelling microscopy: a technical guide to the traditional interpretation. *Nanotechnology*, 17(8):R57, 2006. doi:[10.1088/0957-4484/17/8/R01](https://doi.org/10.1088/0957-4484/17/8/R01).
- [119] Ferney A. Chaves, David Jiménez, Aron W. Cummings, and Stephan Roche. Model of the electrostatics and tunneling current of metal-graphene junctions and metal-insulator-graphene heterostructures. 2013.
- [120] C. V. Thompson. Grain growth in thin films. *Annu. Rev. Mater. Sci.*, 20(1):245–268, August 1990. doi:[10.1146/annurev.ms.20.080190.001333](https://doi.org/10.1146/annurev.ms.20.080190.001333).
- [121] P. E. Blöchl. Projector augmented-wave method. *Phys. Rev. B*, 50:17953–17979, December 1994. doi:[10.1103/PhysRevB.50.17953](https://doi.org/10.1103/PhysRevB.50.17953).
- [122] Yia-Chung Chang. Complex band structures of zinc-blende materials. *Phys. Rev. B*, 25:605–619, January 1982. doi:[10.1103/PhysRevB.25.605](https://doi.org/10.1103/PhysRevB.25.605).
- [123] Yia-Chung Chang and J. N. Schulman. Complex band structures of crystalline solids: An eigenvalue method. *Phys. Rev. B*, 25:3975–3986, March 1982. doi:[10.1103/PhysRevB.25.3975](https://doi.org/10.1103/PhysRevB.25.3975).

- [124] John Robertson. Electronic structure and core exciton of hexagonal boron nitride. *Phys. Rev. B*, 29:2131–2137, February 1984. doi:[10.1103/PhysRevB.29.2131](https://doi.org/10.1103/PhysRevB.29.2131).
- [125] X. Blase, Angel Rubio, Steven G. Louie, and Marvin L. Cohen. Quasiparticle band structure of bulk hexagonal boron nitride and related systems. *Phys. Rev. B*, 51:6868–6875, March 1995. doi:[10.1103/PhysRevB.51.6868](https://doi.org/10.1103/PhysRevB.51.6868).
- [126] Liam Britnell, Roman V. Gorbachev, Rashid Jalil, Branson D. Belle, Fred Schedin, Mikhail I. Katsnelson, Laurence Eaves, Sergey V. Morozov, Alexander S. Mayorov, Nuno M. R. Peres, Antonio H. Castro Neto, Jon Leist, Andre K. Geim, Leonid A. Ponomarenko, and Kostya S. Novoselov. Electron tunneling through ultrathin boron nitride crystalline barriers. *Nano Lett.*, 12(3):1707–1710, 2012. doi:[10.1021/nl3002205](https://doi.org/10.1021/nl3002205).
- [127] Neerav Kharche and Saroj K. Nayak. Quasiparticle band gap engineering of graphene and graphone on hexagonal boron nitride substrate. *Nano Lett.*, 11(12):5274–5278, 2011. doi:[10.1021/nl202725w](https://doi.org/10.1021/nl202725w).
- [128] L. A. Ponomarenko, B. D. Belle, R. Jalil, L. Britnell, R. V. Gorbachev, A. K. Geim, K. S. Novoselov, A. H. Castro Neto, L. Eaves, and M. I. Katsnelson. Field-effect control of tunneling barrier height by exploiting graphene’s low density of states. *J. Appl. Phys.*, 113(13):136502, 2013. doi:[10.1063/1.4795542](https://doi.org/10.1063/1.4795542).
- [129] F. Tuinstra and J. L. Koenig. Raman spectrum of graphite. *J. Chem. Phys.*, 53(3):1126–1130, August 1970. doi:[10.1063/1.1674108](https://doi.org/10.1063/1.1674108).
- [130] A. C. Ferrari, J. C. Meyer, V. Scardaci, C. Casiraghi, M. Lazzeri, F. Mauri, S. Piscanec, D. Jiang, K. S. Novoselov, S. Roth, and A. K. Geim. Raman spectrum of graphene and graphene layers. *Phys. Rev. Lett.*, 97:187401, October 2006. doi:[10.1103/PhysRevLett.97.187401](https://doi.org/10.1103/PhysRevLett.97.187401).
- [131] M. A. Pimenta, G. Dresselhaus, M. S. Dresselhaus, L. G. Cancado, A. Jorio, and R. Saito. Studying disorder in graphite-based systems by Raman spectroscopy. *Phys. Chem. Chem. Phys.*, 9:1276–1290, January 2007. doi:[10.1039/B613962K](https://doi.org/10.1039/B613962K).
- [132] R. Geick, C. H. Perry, and G. Rupprecht. Normal modes in hexagonal boron nitride. *Phys. Rev.*, 146:543–547, June 1966. doi:[10.1103/PhysRev.146.543](https://doi.org/10.1103/PhysRev.146.543).
- [133] R. Arenal, A. C. Ferrari, S. Reich, L. Wirtz, J.-Y. Mevellec, S. Lefrant, A. Rubio, and A. Loiseau. Raman spectroscopy of single-wall boron nitride nanotubes. *Nano Lett.*, 6(8):1812–1816, July 2006. doi:[10.1021/nl0602544](https://doi.org/10.1021/nl0602544).
- [134] Li Song, Lijie Ci, Hao Lu, Pavel B. Sorokin, Chuanhong Jin, Jie Ni, Alexander G. Kvashnin, Dmitry G. Kvashnin, Jun Lou, Boris I. Yakobson, and

- Pulickel M. Ajayan. Large scale growth and characterization of atomic hexagonal boron nitride layers. *Nano Lett.*, 10(8):3209–3215, July 2010. doi:[10.1021/nl1022139](https://doi.org/10.1021/nl1022139).
- [135] Luis Brey. Coherent tunneling and negative differential conductivity in a graphene/*h*-bn/graphene heterostructure. *Phys. Rev. Applied*, 2:014003, July 2014. doi:[10.1103/PhysRevApplied.2.014003](https://doi.org/10.1103/PhysRevApplied.2.014003).
- [136] Edward McCann and Vladimir I. Fal’ko. Landau-level degeneracy and quantum hall effect in a graphite bilayer. *Phys. Rev. Lett.*, 96:086805, March 2006. doi:[10.1103/PhysRevLett.96.086805](https://doi.org/10.1103/PhysRevLett.96.086805).
- [137] Edward McCann. Asymmetry gap in the electronic band structure of bilayer graphene. *Phys. Rev. B*, 74:161403, October 2006. doi:[10.1103/PhysRevB.74.161403](https://doi.org/10.1103/PhysRevB.74.161403).
- [138] Hongki Min, Bhagawan Sahu, Sanjay K. Banerjee, and A. H. MacDonald. *Ab initio* theory of gate induced gaps in graphene bilayers. *Phys. Rev. B*, 75:155115, April 2007. doi:[10.1103/PhysRevB.75.155115](https://doi.org/10.1103/PhysRevB.75.155115).
- [139] Eduardo V. Castro, K. S. Novoselov, S. V. Morozov, N. M. R. Peres, J. M. B. Lopes dos Santos, Johan Nilsson, F. Guinea, A. K. Geim, and A. H. Castro Neto. Biased bilayer graphene: Semiconductor with a gap tunable by the electric field effect. *Phys. Rev. Lett.*, 99:216802, November 2007. doi:[10.1103/PhysRevLett.99.216802](https://doi.org/10.1103/PhysRevLett.99.216802).
- [140] Jeroen B. Oostinga, Hubert B. Heersche, Xinglan Liu, Alberto F. Morpurgo, and Lieven M. K. Vandersypen. Gate-induced insulating state in bilayer graphene devices. *Nature Mater.*, 7(2):151–157, December 2007. doi:[10.1038/nmat2082](https://doi.org/10.1038/nmat2082).
- [141] Taisuke Ohta, Aaron Bostwick, Thomas Seyller, Karsten Horn, and Eli Rotenberg. Controlling the electronic structure of bilayer graphene. *Science*, 313(5789):951–954, August 2006. doi:[10.1126/science.1130681](https://doi.org/10.1126/science.1130681).
- [142] Yuanbo Zhang, Tsung-Ta Tang, Caglar Girit, Zhao Hao, Michael C Martin, Alex Zettl, Michael F Crommie, Y Ron Shen, and Feng Wang. Direct observation of a widely tunable bandgap in bilayer graphene. *Nature*, 459(7248):820–823, 2009. doi:[10.1038/nature08105](https://doi.org/10.1038/nature08105).
- [143] Kayoung Lee, Babak Fallahazad, Jiamin Xue, David C. Dillen, Kyoungwan Kim, Takashi Taniguchi, Kenji Watanabe, and Emanuel Tutuc. Chemical potential and quantum hall ferromagnetism in bilayer graphene. *Science*, 345(6192):58–61, July 2014. doi:[10.1126/science.1251003](https://doi.org/10.1126/science.1251003).

- [144] S. Bala Kumar, Gyungseon Seol, and Jing Guo. Modeling of a vertical tunneling graphene heterojunction field-effect transistor. *Appl. Phys. Lett.*, 101(3):033503, 2012. doi:[10.1063/1.4737394](https://doi.org/10.1063/1.4737394).
- [145] V. Perebeinos, J. Tersoff, and Ph. Avouris. Phonon-mediated interlayer conductance in twisted graphene bilayers. *Phys. Rev. Lett.*, 109:236604, December 2012. doi:[10.1103/PhysRevLett.109.236604](https://doi.org/10.1103/PhysRevLett.109.236604).
- [146] K. M. Masum Habib, Somaia S. Sylvia, Supeng Ge, Mahesh Neupane, and Roger K. Lake. The coherent interlayer resistance of a single, rotated interface between two stacks of AB graphite. *Appl. Phys. Lett.*, 103(24):243114, 2013. doi:[10.1063/1.4841415](https://doi.org/10.1063/1.4841415).
- [147] Zhi-Guo Chen, Zhiwen Shi, Wei Yang, Xiaobo Lu, You Lai, Hugen Yan, Feng Wang, Guangyu Zhang, and Zhiqiang Li. Observation of an intrinsic bandgap and landau level renormalization in graphene/boron-nitride heterostructures. *Nat. Commun.*, 5:4461, 2014. doi:[10.1038/ncomms5461](https://doi.org/10.1038/ncomms5461).
- [148] L. Pratley and U. Zülicke. Valley filter from magneto-tunneling between single and bi-layer graphene. *Appl. Phys. Lett.*, 104(8):082401, February 2014. doi:[10.1063/1.4866591](https://doi.org/10.1063/1.4866591).
- [149] A. K. Geim and I. V. Grigorieva. Van der Waals heterostructures. *Nature*, 499(7459):419–425, July 2013. doi:[10.1038/nature12385](https://doi.org/10.1038/nature12385).
- [150] Gianluca Fiori, Francesco Bonaccorso, Giuseppe Iannaccone, Tomas Palacios, Daniel Neumaier, Alan Seabaugh, Sanjay K. Banerjee, and Luigi Colombo. Electronics based on two-dimensional materials. *Nature Nanotech.*, 9(10):768–779, October 2014. doi:[10.1038/nnano.2014.207](https://doi.org/10.1038/nnano.2014.207).
- [151] Andres Castellanos-Gomez, Michele Buscema, Rianda Molenaar, Vibhor Singh, Laurens Janssen, Herre S. J. van der Zant, and Gary A. Steele. Deterministic transfer of two-dimensional materials by all-dry viscoelastic stamping. *2D Mater.*, 1(1):011002, April 2014. doi:[10.1088/2053-1583/1/1/011002](https://doi.org/10.1088/2053-1583/1/1/011002).
- [152] S. J. Haigh, A. Gholinia, R. Jalil, S. Romani, L. Britnell, D. C. Elias, K. S. Novoselov, L. A. Ponomarenko, A. K. Geim, and R. Gorbachev. Cross-sectional imaging of individual layers and buried interfaces of graphene-based heterostructures and superlattices. *Nature Mater.*, 11(9):764–767, September 2012. doi:[10.1038/nmat3386](https://doi.org/10.1038/nmat3386).
- [153] P. Blake, E. W. Hill, A. H. Castro Neto, K. S. Novoselov, D. Jiang, R. Yang, T. J. Booth, and A. K. Geim. Making graphene visible. *Appl. Phys. Lett.*, 91(6):063124, 2007. doi:[10.1063/1.2768624](https://doi.org/10.1063/1.2768624).